ABSTRACT

Name: Michael Terry Eads Department: Physics

Title: A Search for Charged Massive Stable Particles at DØ

Major: Physics Degree: Doctor of Philosophy

Approved by: Date:

Dissertation Director

NORTHERN ILLINOIS UNIVERSITY

ABSTRACT

A search for charged massive stable particles has been performed with the DØ detector at the Fermilab Tevatron. The signature is two particles reconstructed as muons, but with speed and invariant mass inconsistent with beam-produced muons. No excess of events is observed and limits are set on the production cross-section for pair-produced stable stau sleptons based on 390 $pb^{-1}$ of data. Limits vary from 0.06 pb to 0.62 pb, depending on the stau mass, and are the strictest Tevatron limits to date. Mass limits are also set for stable charginos. The limits are 140 $GeV/c^2$ for a higgsino-like chargino and 174 $GeV/c^2$ for a gaugino-like chargino. These are currently the best limits to date for stable charginos.

NORTHERN ILLINOIS UNIVERSITY

# A SEARCH FOR CHARGED MASSIVE STABLE PARTICLES AT DØ

A DISSERTATION SUBMITTED TO THE GRADUATE SCHOOL
IN PARTIAL FULFILLMENT OF THE REQUIREMENTS
FOR THE DEGREE
DOCTOR OF PHILOSOPHY

DEPARTMENT OF PHYSICS

BY
MICHAEL TERRY EADS


DEKALB, ILLINOIS
AUGUST 2005

Certification: In accordance with departmental and Graduate School policies, this dissertation is accepted in partial fulfillment of degree requirements.

_____

Dissertation Director

_____

Date

# ACKNOWLEDGEMENTS

I would like to thank all members of the physics department for their flexibility in allowing me to complete both a Master's degree and a Doctorate following an unconventional path. I would also like to thank all the members of the DØ collaboration, without whom this research would not have been possible.

In particular, I would like to thank David Hedin for his advice and suggestions over the past several years and his careful reading of this document. I would also like to thank Gerald Blazey for always having time for me, even with his busy schedule. My discussions and classes with Steve Martin were also an invaluable source of knowledge about particle physics, supersymmetry, and physics in general. I would like to thank Volker Buescher, Jean-Francois Grivaz, Dave Cutts, and all the members editorial board 20 who stuck with me in taking this analysis to approval. Finally, thanks to all my students over the years who have helped make sure I don't lose sight of the big picture.

I would like to acknowledge the financial support of the U.S. Department of Education and the National Science Foundation.

DEDICATION

For Tessa and Grant

## TABLE OF CONTENTS

## LIST OF TABLES

Table Page

## LIST OF FIGURES

Figure Page

Figure Page

Figure Page

# CHAPTER 1

# INTRODUCTION

This chapter gives a very brief description of the Standard Model of particle physics. The theory of Supersymmetry is described as a possible solution to some of the shortcomings of the Standard Model. Finally, the breaking of Supersymmetry is discussed.

## A. The Standard Model of Particle Physics

One of the great triumphs of twentieth-century particle physics was the Standard Model of particle physics. The Standard Model is a relativistic quantum field theory. Particles are represented by excitations of fields above the vacuum state. Standard Model particles can be divided into two categories. The first category consists of particles whose spin is an odd integer multiple of $\hbar/2$ and are known as *fermions*. The second category of particles has spin which is a multiple of $\hbar$ and are known as *bosons*. The fundamental fermions of the Standard Model are the matter particles that make up all familiar matter, such as protons, neutrons, and electrons. The fundamental Standard Model bosons are the force carriers. For example, two electrically charged particles will either be attracted to each other (if they have opposite charge) or repelled from each other (if they have identical charge). In the Standard Model, this force of attraction (or repulsion)

is explained by the two charged particles exchanging a *gauge boson* (a photon in this case).

The dynamical behavior of Standard Model particles is summarized in the Standard Model Lagrangian. The specific interactions of the Standard Model particles with the Standard Model forces are determined by transformation properties of the corresponding field in the Lagrangian. Each of the forces in the Standard Model (strong, electromagnetic, and weak) has an associated symmetry group. The complete group structure of the Standard Model is $SU(3)_C \times SU(2)_L \times U(1)_Y$. The $SU(3)_C$ group corresponds to strong interactions, the $SU(2)_L$ group corresponds to weak interactions, and the $U(1)_Y$ group is known as weak hypercharge. In the Standard Model, the $SU(2)_L \times U(1)_Y$ group are spontaneously broken to form the familiar $U(1)_{EM}$ group of electromagnetism. The behavior of each of the Standard Model particles with respect to each of the forces is determined by the particular group representation of the corresponding field. For example, particles which are in an $SU(3)$ singlet will not feel the strong force. All particles transform under the $U(1)_Y$ weak hypercharge group, so the charge of the particle is the relevant parameter. The properties of the fundamental Standard Model fermions are shown in Table 1.1 and bosons in Table 1.2.

It should be noted that the particles listed in Table 1.1 are the gauge eigenstates, while the particle listed in Table 1.2 are mass eigenstates. The gauge eigenstates are the particle states that have definite interactions with the gauge bosons in the Lagrangian. The gauge eigenstates are labeled by their interactions with the $W$-boson. Left-handed states interact with the $W$-boson, while right-handed states do not. However, in general these gauge eigenstates will mix

Table 1.1: The Fundamental Standard Model Fermions

| Particle | Generation | $SU(3)_C$ Representation | $SU(2)_L$ Representation | $U(1)_Y$ Charge |
|---|---|---|---|---|
| $\nu_e, \nu_\mu, \nu_\tau$ | 1, 2, 3 | **1** | **2** | +1/2 |
| $e_L, \mu_L, \tau_L$ | 1, 2, 3 | **1** | **2** | -1/2 |
| $e_R, \mu_R, \tau_R$ | 1, 2, 3 | **1** | **1** | -1 |
| $u_L, c_L, t_L$ | 1, 2, 3 | **3** | **2** | 1/6 |
| $d_L, s_L, b_L$ | 1, 2, 3 | **3** | **2** | 1/6 |
| $u_R, c_R, t_R$ | 1, 2, 3 | **3** | **1** | 2/3 |
| $d_R, s_R, b_R$ | 1, 2, 3 | **3** | **1** | -1/3 |

Table 1.2: The Fundamental Standard Model Bosons

| Particle | Force Mediated | Electric Charge | Mass (GeV/c$^2$) |
|---|---|---|---|
| Photon ($\gamma$) | electromagnetic | 0 | 0 |
| $Z$-boson | weak | 0 | 91.2 |
| $W^{\pm}$-bosons | weak | $\pm 1$ | 80.4 |
| Gluons ($g$) | strong | 0 | 0 |
| (Graviton)[a] ($G$) | gravity | 0 | 0 |

[a]The graviton has yet to be experimentally observed.

to form the states with definite mass, the mass eigenstates. The electron that we are familiar with is actually a mass eigenstate, which is a mixture of both $e_L$ and $e_R$. The $U(1)_Y$ gauge boson is known as the $B$-boson and the $SU(2)_L$ gauge bosons are the $W^+$, $W^-$, and $W^0$. After spontaneous symmetry breaking the $B$ and $W^0$ mix to form the physical photon ($\gamma$) and $Z$-boson states.

Although the Standard Model of particle physics has been a remarkably successful description of nature, it is not a complete description of the world we live in. For example, the Standard Model does not contain a description of the gravitational force. For this reason alone, the Standard Model cannot be a complete desription of nature. However, there are additional reasons to believe that the Standard Model is incomplete.

One of the missing pieces of the Standard Model is an explanation of the measured masses of the particles in the theory. Fermion mass terms are not allowed in the Lagrangian, so the Higgs mechanism has been suggested as the source of the mass of most of the particles in the Standard Model. The Higgs field is a scalar field that has a non-zero vacuum expectation value. Yukawa couplings between the Higgs field and the Standard Model fermions result in effective masses for the particles of the theory. Furthermore, since the minimum of the Higgs potential is not unique, nature will choose a particular minimum and the $SU(2)_L \times U(1)_Y$ electroweak symmetry of the Standard Model Lagrangian will be broken in the vacuum, resulting in the familiar $U(1)_{EM}$ electromagnetic symmetry and also resulting in the masses of the $W^{\pm}$ and $Z$ vector bosons.

One issue with the Higgs mechanism is known as the hierarchy problem. Since all massive particles couple to the Higgs boson, a virtual particle loop will result in corrections to the Higgs propagator and effective corrections to the Higgs boson

mass. The corrections are divergent, and so the usual procedure is to cut off the integral at some high mass scale (such as the GUT or Planck scale). So, if there is any new physics between the weak scale and the Planck scale, one would naively expect that the large corrections to the Higgs boson mass would drive the mass up near the Planck scale, while precision electroweak data suggest that the Higgs mass should be of order 100 GeV/$c^2$.

One possible solution to the hierarchy problem is a very careful choice of the parameters of the theory in order for the large mass corrections to cancel and result in a Higgs boson mass near the weak scale. While this is not ruled out, it is usually considered theoretically distasteful.

Another possible solution to the hierarchy problem utilizes symmetries of the theory in order to ensure cancellations in the Higgs boson mass corrections, making a mass near the weak scale natural. The correction from a scalar loop will be of the opposite sign as the correction resulting from a fermion loop. So, if the theory contains a scalar partner of similar mass for each fermion, there will be large cancellation in the correction factor, stabilizing the Higgs boson mass near its preferred value at the weak scale.

## B. Supersymmetry

Supersymmetry is a proposed symmetry between bosons and fermions. A supersymmetry transformation transforms a fermion into a boson and vice-versa. The particles of the theory should fall into supermultiplets. A *chiral* supermultiplet consists of a Weyl fermion and a complex scalar field. A *gauge* supermultiplet consists of a massless vector boson and a Weyl fermion. Finally, a massless spin-

2 particle will be in a supermultiplet with a massless spin-3/2 particle. Other than the spin, the quantum numbers of the particles in a supermultiplet will be identical.

No pair of Standard Model particles satisfy the requirement to be placed together in a supermultiplet. This is because none of the Standard Model particles that differ by 1/2 unit of spin share the same remaining quantum numbers. So, if Supersymmetry is realized in nature, the number of the particles in the theory will double. All of the Standard Model fermions will have scalar superpartners. The names for these scalar superpartners are denoted by prepending an "s-" to the name of the corresponding Standard Model particle. Also note that chiral supermultiplets contain Weyl fermions. So, in Supersymmetry, the partner of the left-handed electron (the left-handed *selectron*) is a distinct particle from the partner of the right-handed electron (the right-handed *selectron*). The partners of the Standard Model gauge bosons will fall into a gauge supermultiplet and hence be fermions. The names of the fermionic partners of the gauge bosons are denoted by appending an "-ino" to the corresponding name of the Standard Model particle. Finally, the partner of the spin 2 graviton is the spin 3/2 gravitino. The Standard Model particles and their supersymmetric partners are shown in Table 1.3.

Table 1.3: The Standard Model Particles and Their Superpartners

| SM Particle | SM symbol | Superpartner name | Superpartner symbol |
|---|---|---|---|
| **Leptons** | | **Sleptons** | |
| RH electron, muon, tau | $e_R$, $\mu_R$, $\tau_R$ | RH selectron, smuon, stau | $\tilde{e}_R$, $\tilde{\mu}_R$, $\tilde{\tau}_R$ |
| LH electron, muon, tau | $e_L$, $\mu_L$, $\tau_L$ | LH selectron, smuon, stau | $\tilde{e}_L$, $\tilde{\mu}_L$, $\tilde{\tau}_L$ |
| Electron, muon, tau neutrino | $\nu_e$, $\nu_\mu$, $\nu_\tau$ | Electron, muon, tau sneutrino | $\tilde{\nu}_e$, $\tilde{\nu}_\mu$, $\tilde{\nu}_\tau$ |
| **Quarks** | | **Squarks** | |
| RH up, charm, top quark | $u_R$, $c_R$, $t_R$ | RH up, charm, top squark | $\tilde{u}_R$, $\tilde{c}_R$, $\tilde{t}_R$ |
| LH up, charm, top quark | $u_L$, $c_L$, $t_L$ | LH up, charm, top squark | $\tilde{u}_L$, $\tilde{c}_L$, $\tilde{t}_L$ |
| RH down, strange, bottom quark | $d_R$, $s_R$, $b_R$ | RH down, strange, bottom squark | $\tilde{d}_R$, $\tilde{s}_R$, $\tilde{b}_R$ |
| LH down, strange, bottom quark | $d_L$, $s_L$, $b_L$ | LH down, strange, bottom squark | $\tilde{d}_L$, $\tilde{s}_L$, $\tilde{b}_L$ |
| **Gauge Bosons** | | **Gauginos** | |
| Charged Higgs | $H^\pm$ | Charged Higgsino | $\tilde{H}^\pm$ |
| W-bosons | $W^\pm$, $W^0$ | Winos | $\tilde{W}^\pm$, $\tilde{W}^0$ |
| Neutral Higgs | $h^0$, $H^0$, $A^0$ | Neutral Higgsinos | $\tilde{H}^0_u$, $\tilde{H}^0_d$ |
| B-boson | $B$ | Bino | $\tilde{B}$ |
| Gluon | $g$ | Gluino | $\tilde{g}$ |
| Graviton | $G$ | Gravitino | $\tilde{G}$ |

Note that in the Standard Model one complex Higgs doublet is sufficient. After electroweak symmetry breaking one physical Higgs boson remains. In supersymmetry, two complex Higgs doublets are necessary. After electroweak symmetry breaking, five physical Higgs particles are present - two charged ($H^{\pm}$), two scalar ($h_0$ and $H_0$), and one pseudoscalar ($A_0$).

Many of the superpartners share the same quantum numbers, and hence the gauge eigenstates listed in Table 1.3 will mix to form mass eigenstates. This is shown in Table 1.4. The charged gauginos mix to form four *chargino* mass eigenstates. The four neutral gauginos will mix to form the four *neutralino* mass eigenstates. Finally, mixing is also possible in the squark and slepton sector. This occurs because of non-zero off-diagonal elements in the mass matrices in the supersymmetric Lagrangian. Since the size of these off-diagonal elements is proportional to the Yukawa coupling, the mixing is only important for squarks and sleptons in the third generation. The mass eigenstates are labeled with subscripts according to mass, with the lightest mass eigenstate having a subscript of one.

Table 1.4: Superpartner Mixing States

| Gauge Eigenstates | Mass Eigenstates |
|---|---|
| $\tilde{W}^{\pm}$, $\tilde{H}^{\pm}$ | $\tilde{\chi}_1^{\pm}$, $\tilde{\chi}_2^{\pm}$ |
| $\tilde{W}^0$, $\tilde{B}$, $\tilde{H}_u^0$, $\tilde{H}_d^0$ | $\tilde{\chi}_1^0$, $\tilde{\chi}_2^0$, $\tilde{\chi}_3^0$, $\tilde{\chi}_4^0$ |
| $\tilde{\tau}_R$, $\tilde{\tau}_L$ | $\tilde{\tau}_1$, $\tilde{\tau}_2$ |
| $\tilde{t}_R$, $\tilde{t}_L$ | $\tilde{t}_1$, $\tilde{t}_2$ |
| $\tilde{b}_R$, $\tilde{b}_L$ | $\tilde{b}_1$, $\tilde{b}_2$ |

In order to avoid rapid proton decay, a new quantum number is usually assumed to be conserved for particles and their superpartners. This is known as

$R$-parity. All Standard Model particles have odd $R$-parity ($R = +1$), while all superparticles have even $R$-parity ($R = -1$). In any process, the product of $R$-parity for the particles in the initial state must equal the product for the final state particles. This means that superparticles are always produced in pairs (at least in collisions of Standard Model particles) and also that the lightest supersymmetric particle (LSP) will be stable (providing a candidate for dark matter). Although strict $R$-parity conservation is not a requirement, we will assume that $R$-parity is strictly conserved.

## C. Supersymmetry Breaking

If supersymmetry were an exact symmetry of nature, then the superpartners would have exactly the same masses as their Standard Model partners. Since superpartners share the same couplings as their Standard Model partners, at least some of the superpartners would have already been discovered.

So, it is usually assumed that supersymmetry is a broken symmetry and hence the superpartners are heavier than their Standard Model partners and thus have escaped detection. This breaking can be realized by including terms in the Lagrangian that preserve gauge invariance but have positive mass dimension. In order to preserve the cancellations necessary to solve the hierarchy problem, these mass terms should not be much more than of order 1 TeV. If all possible terms that preserve gauge invariance and have positive mass dimension are included in the Lagrangian, an additional 105 parameters are necessary. To reduce the number of parameters to a more manageable level, some mechanism for spontaneously breaking supersymmetry is usually assumed.

One possibility is that supersymmetry is broken by interactions that occur at gravitational strength, which implies a mass scale at the Planck scale. The most common of these models is known as *Supergravity* [1]. Another possibilty is that supersymmetry is broken by standard gauge interactions at a much lower scale. One example is known as *gauge-mediated supersymmetry breaking* or GMSB [2]. Still another possibility is known as *anomaly-mediated supersymmetry breaking* or AMSB [3]. All of these supersymmetry-breaking models are very predictive and have only a few free parameters, although there is nothing that would suggest that nature has realized a situation quite as simple as those assumed in these models.

## CHAPTER 2

## MASSIVE STABLE PARTICLES

The term *stable* is used somewhat ambiguously in particle physics. In some cases, it refers to particles that are absolutely stable and never decay. In other situations, it can refer to particles that have lifetimes comparable to or longer than the time interval of interest. We shall use the term *stable* to refer to particles that have a lifetime long enough to escape the detector before decaying. In practice, this means particles having a lifetime on the order of a microsecond or more. So, for example, even though a muon is not absolutely stable, it has a lifetime long enough to completely penetrate the detector, and so for our purposes the muon is stable.

# A. Models Predicting Massive Stable Particles

There are many models that can predict the existence of massive stable particles beyond the Standard Model. (For an experimental and theoretical review, see Ref. [4].) In general, a massive stable particle could be electrically neutral or have unit or fractional electrical charge. Cosmological arguments disfavor electrically charged massive particles that are absolutely stable, as these particles would have been produced in the big bang and hence should be observable today, but have not been observed. However, there are no such restrictions on particles that are

electrically charged and have lifetimes that are stable on collider detector time scales but small on cosmological time scales. Furthermore, these massive stable particles could interact via the strong force as well. We are interested in massive stable particles that are electrically charged, as their signature in the detector is well known and easily modeled.

There are a few general conditions that can lead to the stability of a particle. One is a conserved quantum number. For example, in Supersymmetry, $R$-parity is usually assumed to be conserved. This means that the lightest supersymmetric particle must be absolutely stable. Even if $R$-parity is not absolutely conserved, in order to avoid constraints from proton decay experiments it must be violated at only a small level. This could result in a lightest supersymmetric particle that is stable on detector time scales.

Another source of stability is a very weak coupling. If a particle has only one allowed decay mode and the coupling present in this mode is very small, then the particle can acquire a lifetime long enough to appear stable in the detector. For example, if the only allowed decay mode involves the decay to a graviton (or gravitino), then the decay will proceed with gravitational strength, which can result in a long lifetime. Another possibility is that a decay can only occur through a virtual particle that is very heavy and hence very far off mass shell (and highly suppressed).

A final source of stability can come from kinematic considerations. If there is very little available phase space for the decay to proceed, the lifetime of the particle can be large. This can occur if the only allowed decay mode of the particle in question is to another particle that is nearly degenerate in mass. The smaller the mass difference between the two particles, the longer the lifetime of

the heavier particle will be.

There are many models that contain the above features and hence can predict the existence of a massive stable particle. One possibility is a gauge-mediated supersymmetry breaking (GMSB) model. Since the supersymmetry breaking scale in GMSB models is fairly low, all GMSB models contain a gravitino/goldstino as the LSP.[1] The phenomenology of the model is then driven by the next-to-lightest supersymmetric particle (NLSP). The NLSP can be either the lightest neutralino or the lightest stau mass eigenstate, depending upon the parameters of the model. The coupling of the NLSP to the LSP gravitino/goldstino can be suppressed, resulting in a long lifetime. If the lightest stau is the NLSP it will have a decay length given by Equation 2.1 [5].

$$L \approx 10 \text{ km} \times \langle\beta\gamma\rangle[\frac{F_{DSB}^{1/2}}{10^7 \text{ GeV}}]^4[\frac{100 \text{ GeV}}{m_{\tilde{\tau}_1}}]^5 \tag{2.1}$$

where $\beta$ and $\gamma$ are the relativistic factors and $F_{DSB}^{1/2}$ is the non-zero vacuum expectation value of the $F$ component of a chiral superfield. The stau is expected to be stable if $F_{DSB}$ is on the order of $10^7$ GeV or larger.

It should also be noted that a similar situation can occur in Planck-scale mediated supersymmetry breaking models, such as Supergravity. The mass of the gravitino/goldstino can be taken as a free parameter in the theory. Hence, it is possible that the gravitino/gravitino could be the LSP. As in GMSB, if the lightest stau is the NLSP and decays to the gravitino/goldstino are suppressed, the lifetime of the stau can become large. It has been suggested that if Super-

[1]The gravitino absorbs the pseudo-Nambu-Goldstone fermion generated from the spontaneous breaking of supersymmetry. The couplings of the goldstino are more important than those of the gravitino in determining the interactions of the particle.

symmetry with a gravitino/goldstino LSP is realized in nature, the lifetime of the NLSP should be in the order of one year or more to avoid complications with structure formation and big-bang nucleosynthesis in the early universe [6].

There are also supersymmetric models that predict a stable lightest chargino. If the lightest neutralino is the LSP and the lightest chargino is the NLSP the only allowed decays of the lightest chargino involve a neutralino. If the mass difference between the chargino and neutralino is very small these decays will be highly suppressed by the available phase space. This can occur in supersymmetric models that do not assume mass unification at some high scale. The chargino will appear stable in the detector if the mass difference between the lightest chargino and the lightest neutralino is less than about 150 MeV/c$^2$ [7, 8]. Figure 2.1 shows the lifetime and branching fractions of the lightest chargino as a function of the chargino-neutralino mass difference, $\Delta m_{\tilde{\chi}_1}$. Anomaly-mediated supersymmetry breaking (AMSB) models predict a lightest neutralino and lightest chargino that are nearly mass degenerate. However, after including loop corrections to the particle masses, it has been shown that in AMSB the mass difference between the chargino and neutralino is not small enough over most of the parameter space to result in a stable chargino [9]. However, a mass difference small enough to result in a stable chargino can be achieved in more general models of supersymmetry breaking [10].

Since the behavior of electrically charged particles in the detector is well understood, this analysis searches only for massive stable particles that are electrically charged. Both a GMSB stable stau model and stable chargino models are explored. However, there are other models that can predict massive stable particles.

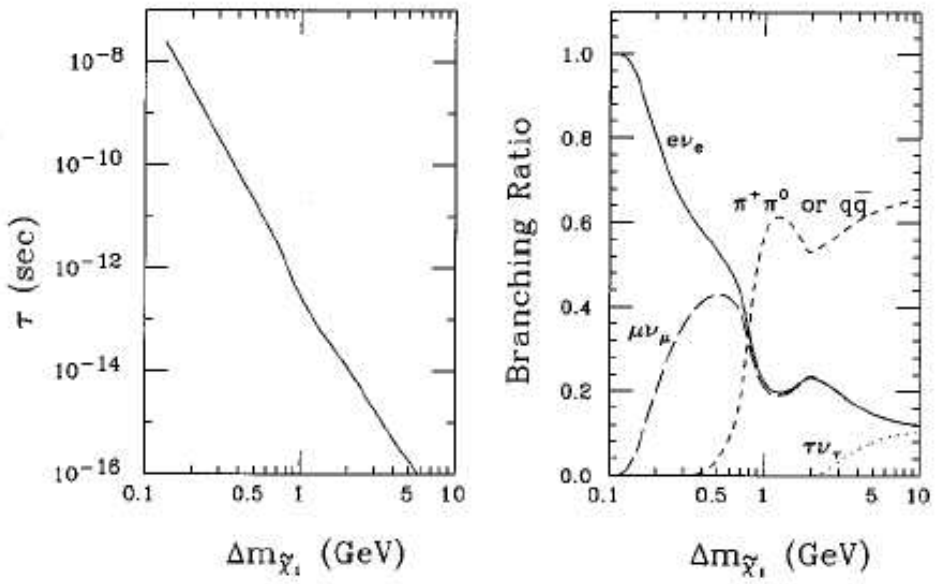


Figure 2.1: The chargino lifetime (left) and branching fractions to various final states (right) as a function of the chargino-neutralino mass difference. Figure taken from [7].

Another possible source of massive stable particles comes from a model known as split supersymmetry [11]. In this model, all scalars are very heavy ($\gtrsim 1$ TeV/c$^2$) and only the gauginos are expected to have masses near the weak scale. The gluino is the only colored particle at this low mass scale. The decays of the gluino can proceed only through the $t$-channel exchange of a virtual squark. Since the squarks are very heavy, this decay will be suppressed and the gluino can have a long lifetime. However, since the gluino is a strongly interacting particle, it will hadronize to form a particle known as an $R$-hadron. This $R$-hadron may be charged or neutral. Furthermore, as the $R$-hadron travels through the detector, it can exchange charge with the nuclei of the detector material. This can result in tracks that are alternately positively charged, negatively charged, or neutral. A very simlar situation can occur in supersymmetric models that predict a stable

lightest stop quark. Although stable stops or gluinos are strongly produced and hence have a large production cross section at the Tevatron, it is very difficult to model the hadronization of the $R$-hadrons and charge exchange effects in the detector. Therefore, this analysis does not make any attempt to set limits for stable stops or gluinos, although these could appear as slowly moving particles within the detector. However, no attempt has been made to calculate the efficiency for $R$-hadrons to be detected.

Another possible model that predicts a long-lived particle is Supersymmetry with the axino as the LSP [12]. The axino is the superpartner of the axion. The axion is a new particle that is predicted in certain solutions to the strong CP problem. If the axino is the LSP, then decays of the NLSP can proceed only through triangle diagrams, or three-body decays, resulting in a long lifetime for the NLSP. This analysis does not search for stable particles resulting from an axino LSP. However, the signal for such a scenario would be very similar to the models explored in this analysis.

## B. Charged Massive Stable Particle Detector Signature

A colorless, electrically charged particle will lose energy in the detector primarily through ionization. Since this ionization energy loss is small compared to the kinetic energy of a CMSP, the particle will traverse the entire detector. Hence, it will register in the outermost layers of the detector (the muon system) and its signature in the detector will be similar to a muon.

However, there will be several important differences between the detector

signature of a muon compared to a CMSP. At the energy of the Tevatron ($\sqrt{s}$ = 1.96 TeV), beam-produced muons (with a mass of 0.106 GeV/c$^2$) will be highly relativistic and will be traveling very near the speed of light. Muons that traverse the entire detector at DØ must have a momentum larger than approximately 3 GeV/c, ensuring that these particles will be relativistic. However, CMSPs (with an expected mass of at least 100 GeV/c$^2$) will not be relativistic and a substantial fraction of particles will be moving at speeds slower than the speed of light. Figure 2.2 shows the generator-level speed distributions for muons from Z boson decays, 100 GeV/c$^2$ staus, and 300 GeV/c$^2$ staus.

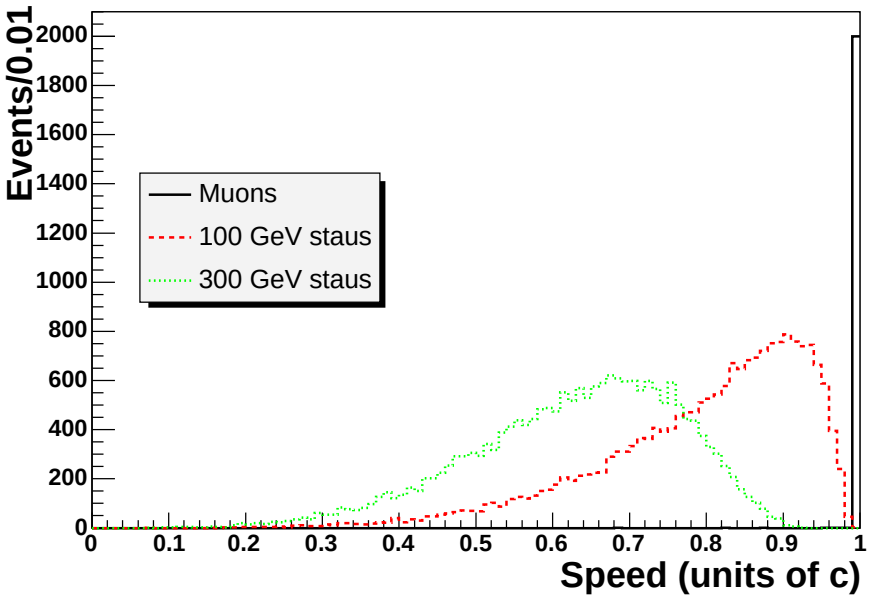


Figure 2.2: Speed distributions for muons from Z boson decays (solid black line), 100 GeV/c$^2$ staus (dashed red line), and 300 GeV/c$^2$ staus (dotted green line). Speeds are from generator level monte carlo simulation and no detector resolution effects are included.

Another distinct signature of CMSPs in the detector is the energy loss of the particle as it traverses the detector. Figure 2.3 shows the rate of energy loss

(dE/dx) for muons traveling through copper for a wide range of muon momenta. For muons whose energy loss is primarily through ionization (that is, muons which are nearly minimum-ionizing particles), the energy loss can be calculated by the Bethe-Bloch equation [13]. This equations predicts that the ionization energy loss of a particle is proportional to approximately $1/\beta^2$, where $\beta$ is the speed in units of the speed of light. So, if a CMSP has a speed of $\beta = 0.7$ it is expected to have an energy loss approximately twice as large as a minimum ionizing particle.

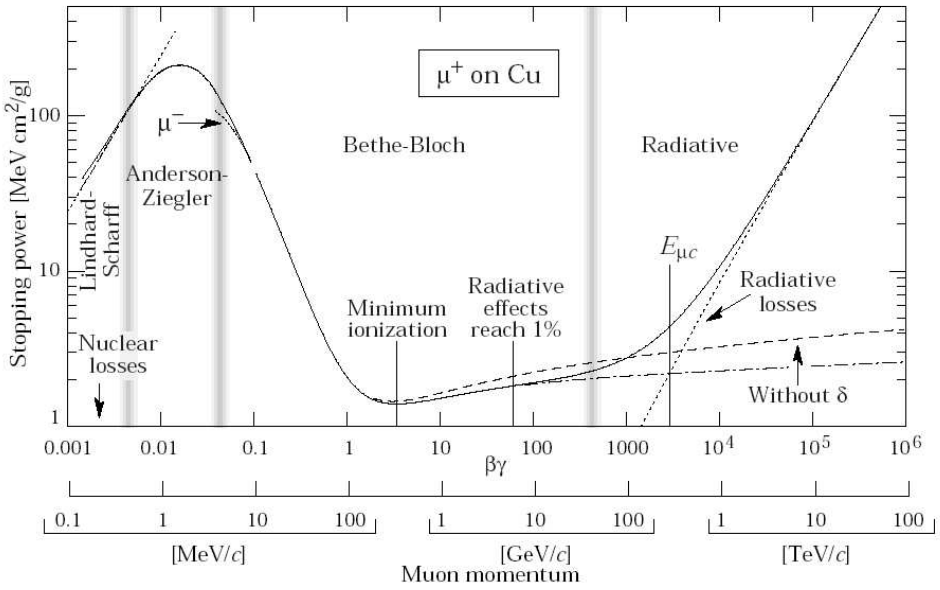


Figure 2.3: The energy loss of muons in material as a function of momentum. Figure taken from [13].

However, a non-negligible fraction of muons at DØ have momenta large enough that radiative energy loss effects become non-negligible. This can be seen in the gradual increase in energy loss for muons with momenta larger than the minimum ionizing point. So, the separation in energy loss between muons and CMSPs is not as good as one would expect if all the muons were minimum ionizing parti-

cles. Energy loss has not been used in this analysis, since it is possible to set a meaningful limit using only speed information, without introducing the additional systematics of energy loss.

## C. Previous CMSP Searches

Many searches for CMSPs have been performed, both at colliders and elsewhere. One way to search for CMSPs is to look for superheavy atomic isotopes. If CMSPs are present at a small level in the universe, or if they are produced in cosmic ray events, then it is possible that they can attach to a normal molecule to form a superheavy state. Searches for superheavy water molecules have been performed on sea water. Searches for superheavy isotopes have been performed on other materials. These experiments have all set limits on the flux of CMSPs as a function of the CMSP mass [14]. However, these experiments assume that the CMSP has a very long lifetime since it must be produced, bind to another molecule, and then be collected and detected by an experiment. The limits imposed by these experiments do not constrain CMSPs that have a lifetime long enough to excape the detector ($\gtrsim 10^{-6}$ s), but decay quickly thereafter.

A search for stable long-lived particles was carried out during Run I of the CDF detector at the Fermilab Tevatron [15]. This analysis was primarily a search for strongly interacting massive stable particles, but limits were also set for a stable slepton scenario. 95% confidence level cross section limits were set that varied from 1.3 pb (for a slepton mass of 80 GeV/c$^2$) to 0.75 pb (for a slepton mass of 120 GeV/c$^2$).

Searches for stable sleptons have also been performed at LEP. These searches

have resulted in 95% confidence level slepton mass limits that vary from 77 GeV/c$^2$ to 102 GeV/c$^2$, depending on the experiment [16]. A preliminary combination of the results from all four experiments has been performed by the LEP SUSY working group [17]. This combination has ruled out (at the 95% confidence level) right-handed sleptons with masses between 45 and 99.4 GeV/c$^2$ and left-handed sleptons with masses between 45 and 99.6 GeV/c$^2$. Figure 2.4 shows the excluded region in slepton mass versus cross section plane.

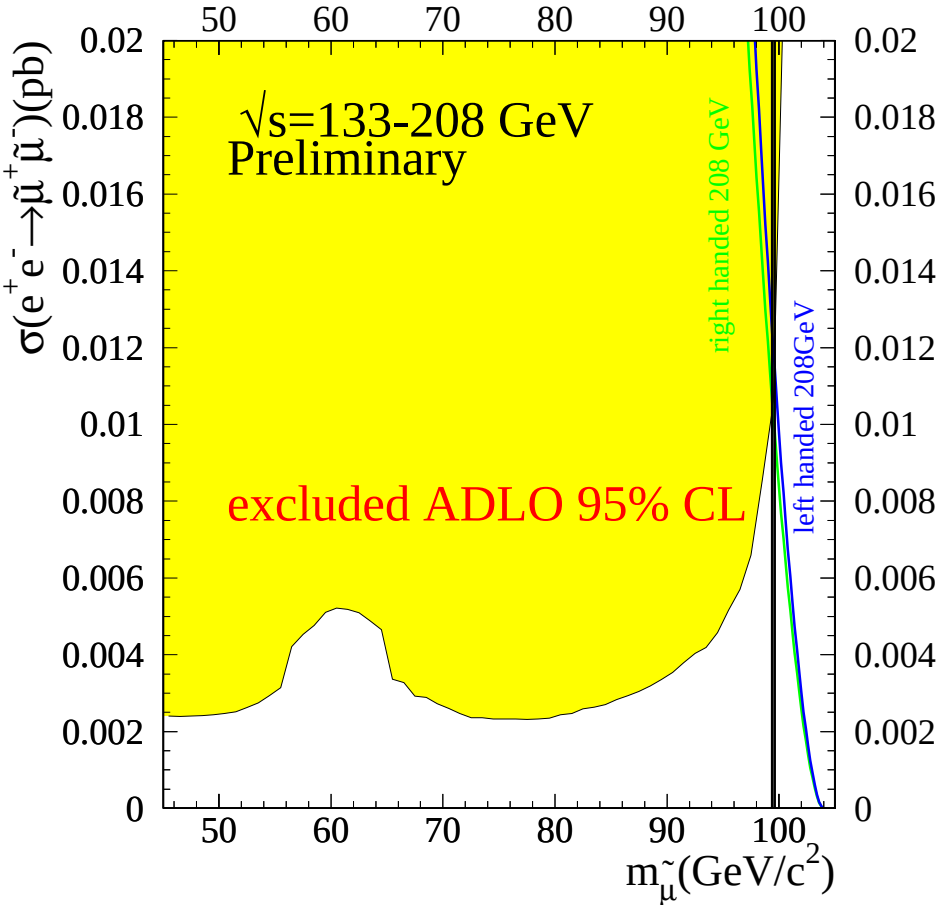


Figure 2.4: Combined LEP excluded region in the cross section versus mass plane for stable sleptons. Figure is from Ref. [17].

Searches for stable charginos have also been performed at LEP. These searches have placed 95% confidence level mass limits on stable chargino that vary from 87.5 GeV/$c^2$ to 102.0 GeV/$c^2$, depending on the experiment [18]. A preliminary combination of all LEP stable chargino results by the LEP SUSY working group has excluded stable charginos in the mass range of 45 GeV/$c^2$ to 102.5 GeV/$c^2$, at the 95% confidence level. Figure 2.5 shows the excluded region in the chargino cross section versus mass plane.

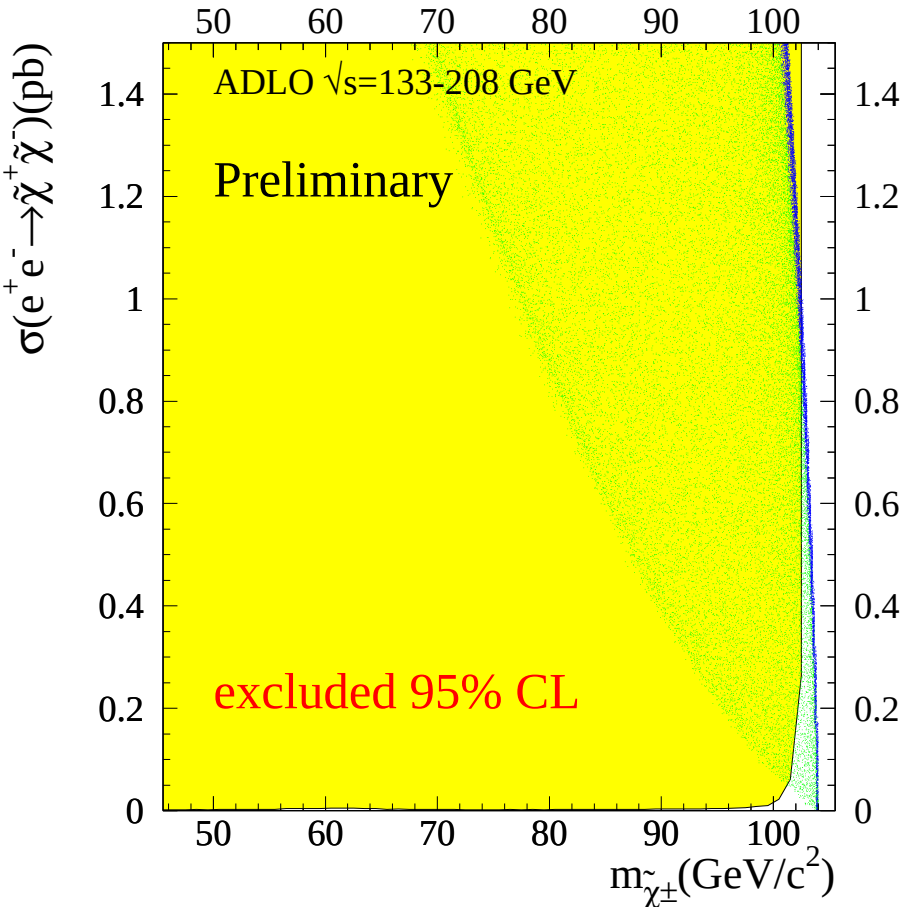


Figure 2.5: Combined LEP excluded region in the cross section versus mass plane for stable charginos. Figure is from Ref. [17].

# CHAPTER 3

# EXPERIMENTAL APPARATUS

A search for CMSPs has been carried out using the DØ detector at the Fermilab Tevatron collider. The Tevatron is currently the world's highest energy particle accelerator, colliding protons on antiprotons at a center of momentum energy $\sqrt{s} = 1.96$ TeV. The DØ detector is one of two multi-purpose collider detectors located at Fermilab. Since Fermilab is the source of the world's highest energy collisions, it is a natural location to search for physics beyond the standard model.

## A. The Fermilab Accelerator Complex

Fermilab is a hadron collider, colliding a beam of protons with a beam of antiprotons. Both beams have an energy of 980 GeV, resulting in a 1.96 TeV collision energy in the center of momentum frame. This is and will be the highest energy collider in the world until the Large Hadron Collider becomes operational at CERN.

Fermilab uses a series of several accelerators to bring the beams up to their final energies. The sequence of accelerators is shown schematically in Figure 3.1. The protons begin at the Cockcroft-Walton accelerator. This is a DC accelerator that forms negative ions from hydrogen gas and accelerates the resulting ions to an energy of 750 keV.

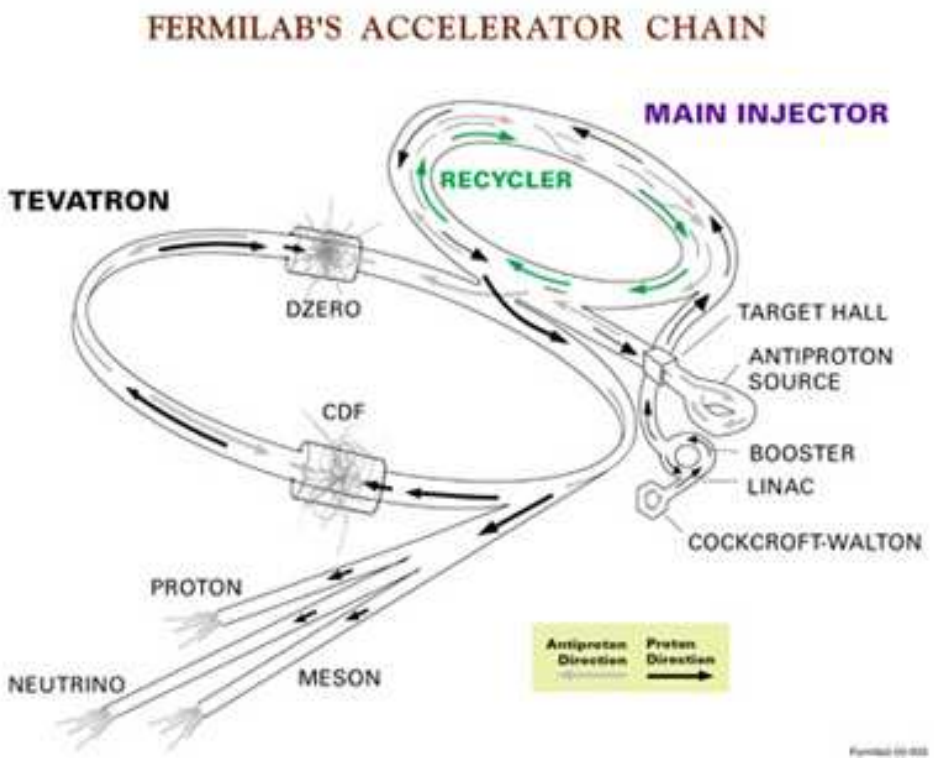


Figure 3.1: A schematic diagram of the sequence of accelerators at Fermilab. Image is courtesy of Fermi National Accelerator Laboratory.

The 750 keV protons are then injected into a linear accelerator. This accelerator is approximately 500 feet in length and uses a series of radio-frequency cavities to accelerate the negative hydrogen ion beam to an energy of 400 MeV. The electrons are removed from the hydrogen ions at the end of the linear accelerator using carbon foil.

After the linear accelerator, the 400 MeV protons enter the booster. This is a synchrotron accelerator that raises the energy to 8 GeV. After the booster, the protons enter the Main Injector. The Main Injector is a synchrotron with a circumference of two miles. It accelerates the proton beam to an energy of 150 GeV for injection into the next stage of acceleration. Furthermore, some of the protons in the Main Injector are used to create antiprotons.

To create antiprotons, 120 GeV protons from the Main Injector are extracted and are collided with a nickel target. A great number of secondary particles are created in this collision, including some antiprotons. The antiprotons are collected using a lithium lens and magnets that capture antiprotons with an energy of 8 GeV. The 8 GeV antiprotons are then transferred to the accumulator/debuncher. This device cools the captured antiprotons and arranges them into bunches with the same time structure as the proton beam in the main injector. After a large number of antiprotons have been collected, a process that ususally takes tens of hours, the antiprotons are injected into the Main Injector and accelerated to 150 GeV.[1]

[1]The Fermilab accelerator division is currently also using the Recycler, a permanent magnet storage ring installed in the Main Injector tunnel, to store antiprotons. After storing a number of antiprotons in the accumulator/debuncher, they are transferred to the recycler. Additional antiprotons are then created and stored in the accumulator/debuncher. This allows larger numbers of antiprotons to be created and stored since the rate of storing antiprotons is inversely proportional to the number of antiprotons already present in the accumulator/debuncher.

The final stage of the accelerator complex for protons and antiprotons is the Tevatron. The Tevatron is a synchrotron with a four-mile circumference that uses superconducting magnets and radio-frequency cavities to accelerate the proton and antiproton beams to an energy of 980 GeV. The proton and antiproton beams travel in the same beam pipe and can be made to collide at six points in the ring. Experiments (CDF and DØ) are located at two of these interaction regions. The Tevatron utilizes 36 bunches of protons and 36 bunches of antiprotons. The time spacing between bunches is 396 ns.

## B. The DØ Detector

The DØ detector is one of two general purpose collider detectors located at the Fermilab Tevatron. DØ employs a cylindrical coordinate system where the $z$-axis is located along the beam direction, with the positive direction along the proton direction. The angle $\phi$ is the azimuthal angle around the $z$-axis, measured from the horizontal direction pointing out of the Tevatron ring. The polar angle, $\theta$, is measured from the positive $z$-axis.

In practice, it is much more useful to use the *pseudorapidity* ($\eta$) than the polar angle. The pseudorapidity is defined as in equation 3.1.

$$\eta = -\ln\left(\tan\frac{\theta}{2}\right) \tag{3.1}$$

The pseudorapidity is identical to rapidity[2] in the limit that the particle is massless.

[2]The rapidity, $y$, is defined as $y = \frac{1}{2}\log\frac{E+p_L}{E-p_L}$, where $E$ is the energy of the particle and $p_L$ is the component of the momentum along the direction of the beam.

Furthermore, since protons (and antiprotons) are composite objects, it is impossible to know the exact momentum of the constituent quarks in the direction along the beam. Furthermore, some remnants of the proton (or antiproton) will escape down the beam pipe and be undetected. Therefore, it is useful to use the components of the quantities of interest that are transverse to the beam direction. For example, the transverse momentum ($p_T$) is defined as in equation 3.2, where $p$ is the three-momentum.

$$p_T = p \sin\theta \tag{3.2}$$

The DØ detector consists of a number of subdetectors arranged in several layers. A picture of the detector, showing the various subsystems, can be seen in Figure 3.2. The DØ detector underwent a succesful experimental run, refered to as Run I, from 1992 to 1995. The Run I detector is described in detail in Ref. [19]. One of the many successes of the Run I physics program was the simultaneous discovery of the top quark with CDF [20].

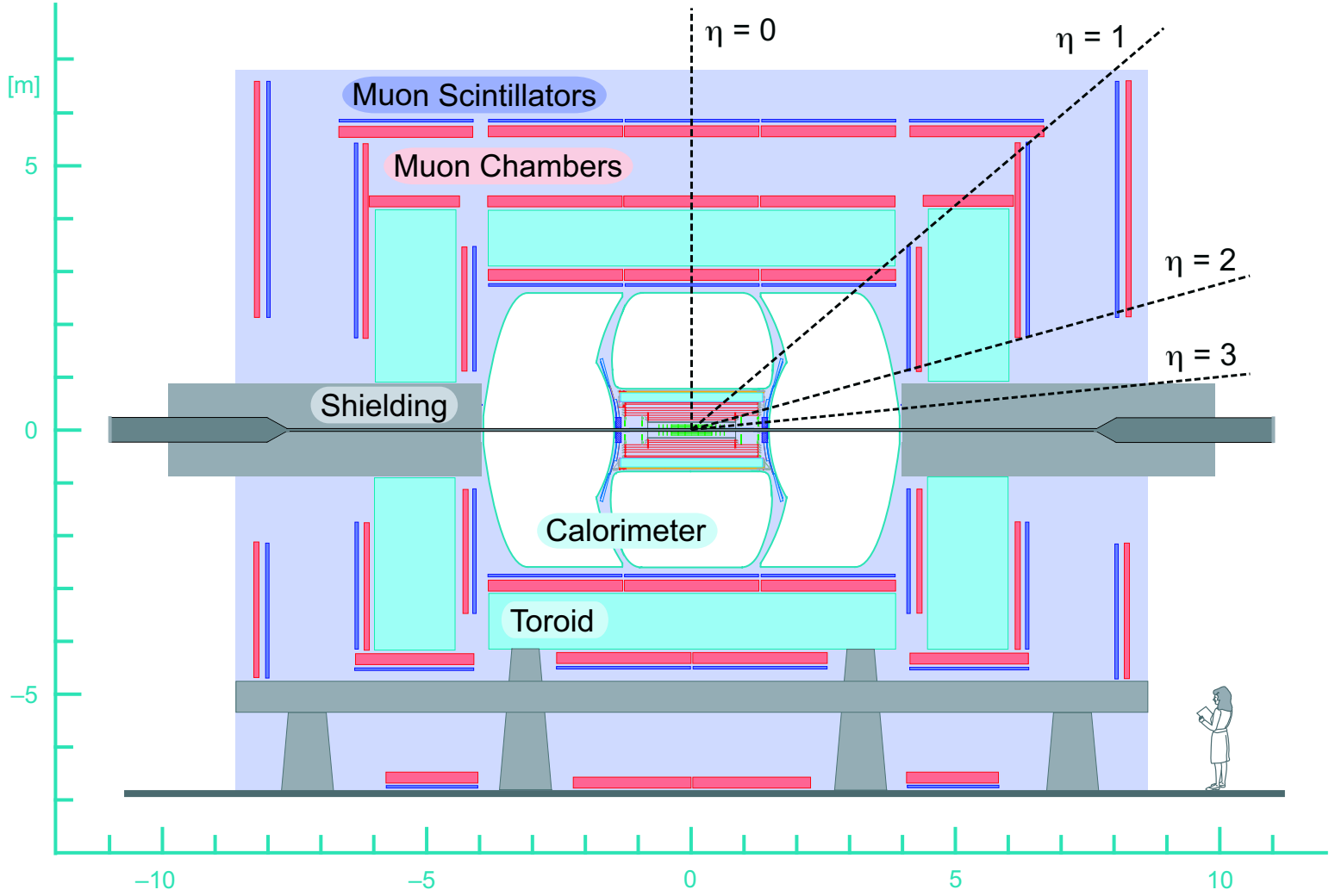


Figure 3.2: The DØ Detector

After the end of Run I, the DØ detector underwent a substantial upgrade to prepare for an increase in luminosity and a decreased bunch spacing (from 3.56 $\mu$s to 396 ns). The DØ Run II detector includes improvements to the central tracking system, the muon system, and the readout and trigger electronics. The upgraded DØ detector is described in detail in Ref. [21].

The DØ detector central tracking system is composed of a silicon vertex detector and a scintillating fiber tracker. The central tracking systems are inside a 2 T solenoidal magnet which allows for a determination of momenta prior to entering the calorimeter. The calorimeter is a liquid argon-uranium sampling calorimeter with excellent segmentation. The muon system consists of three layers of scintillation counters and drift tubes. The first layer is inside a 1.8 T iron toroid, while the next two layers are outside the iron toroid.

The central tracking system consists of both a silicon vertex detector and a central fiber tracker, as shown in Figure 3.3. Both of these systems are inside a solenoid with a field of 2 T. The combination of these two systems allows for the precise location of the exact interaction point of a collision as well as the tracks of all particles emanating from the collision point. When combined with a magnetic field, the system becomes a magnetic spectrometer, allowing the measurement of the momentum of charged particles in the region of the detector closest to the beam pipe.

The silicon vertex detector, pictured in Figure 3.4, is a combination of two different types of detectors. Barrel detectors are used to measure the r-$\phi$ coordinate while disk detectors measure both the r-z and r-$\phi$ coordinate. The barrel detectors are located near the center of the detector, while the disks (F-disks and H-disks) are located further away from the center of the detector, along the

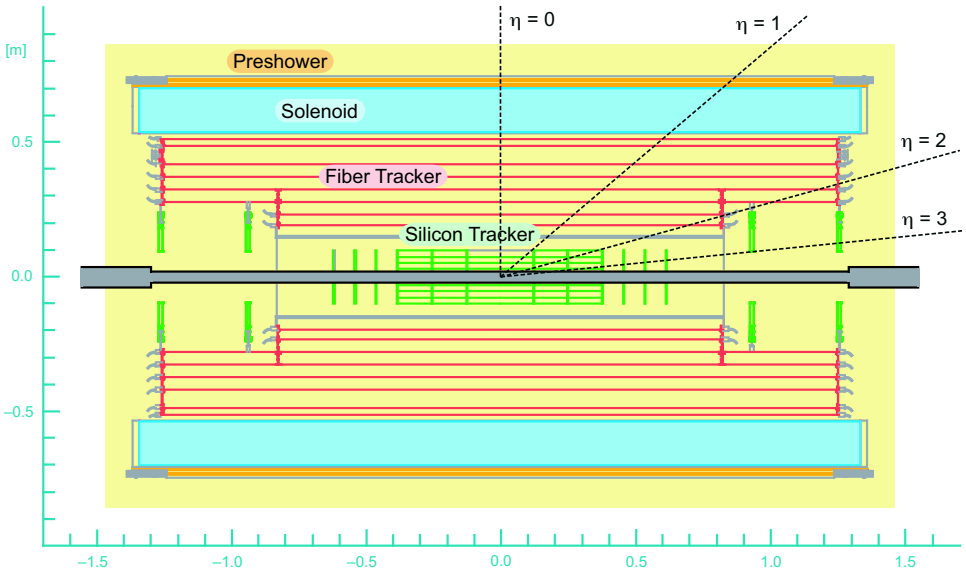


Figure 3.3: The DØ Central Tracking System

beamline. The silicon vertex detector is constructed of interleaved layers of silicon to provide coverage out to a pseudorapidity of three. The 50 $\mu$m pitch of the silicon strips provide a spatial resolution of 10 $\mu$m.

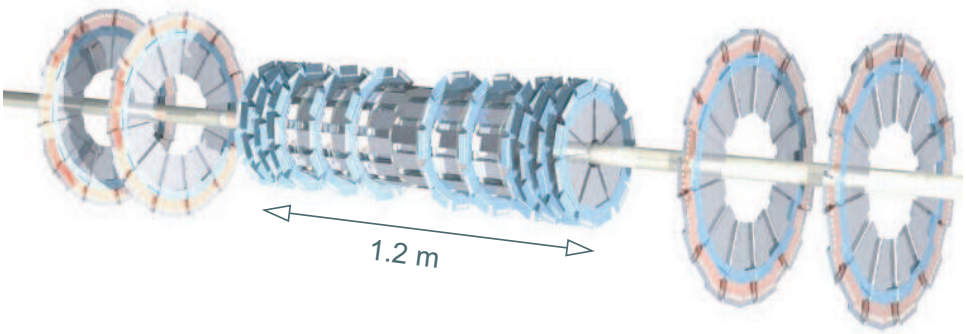


Figure 3.4: The DØ Silicon Detector

The scintillating fiber tracker is located just outside the silicon detector. It consists of about 74,000 scintillating fibers mounted on eight concentric cylinders

at radii of 19.5, 23.4, 28.1, 32.8, 37.5, 42.1, 48.8, and 51.5 cm. Furthermore, every other layer contains two additional layers of fibers mounted at a stereo angle to compensate for the gaps in between the fibers on layers containing only one layer. The CFT provides charged particle tracking out to a pseudorapidity of 1.7. The presence of the solenoid also allows for a measurement of the momentum of the charged particle prior to the calorimeter. Charged particle tracks from the central tracking system are also used to locate muons in the outer layers of the detector. The resolution of the central fiber tracker has been measured to be about 100 $\mu$m with a detection efficiency of greater than 99%.

The DØ calorimeter is a liquid argon-uranium sampling calorimeter. Due to its excellent performance during Run I, the calorimeter was not changed for Run II. However, the front-end electronics were upgraded to handle the shorter bunch crossing times. The calorimeter is pictured in Figure 3.5. The calorimeter is divided into three main sections. The central calorimeter provides coverage to roughly a pseudorapidity of one. There is also an end calorimeter on each side of the central calorimeter. The end calorimeters provide coverage to about $|\eta| < 4$. Within each section of the calorimeter there are several distinct layers. The layer closest to the beamline is the electromagnetic calorimeter. After the electromagnetic calorimeter, there is first a fine hadronic section, and finally a coarse hadronic section at the outermost layer of the calorimeter.

The muon system is essential for detecting CMSPs. In particular, the scintillation detectors provide a way to accurately measure the time-of-flight of a CMSP from the interaction point to the point of detection. Since the location of all detectors is known, it then becomes straightforward to calculate the speed of the CMSP. Muons that appear in the muon system are highly relativistic and

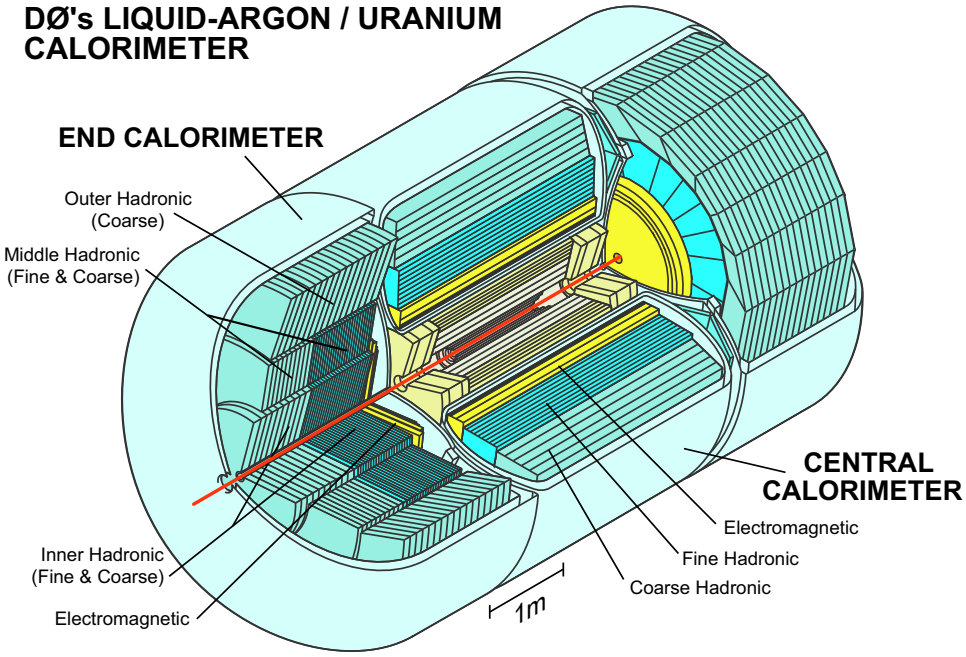


Figure 3.5: The DØ Calorimeter

have a speed very close to the speed of light. In contrast, massive particles will have a speed much less than the speed of light. Therefore, an accurate measure of time-of-flight will provide good rejection of background muons.

The Run II muon system is described in detail in Ref. [22]. The muon system is divided into two main areas. The central muon system provides coverage for $|\eta| < 1$ [23]. The forward muon system provides coverage for approximately $1 < |\eta| < 2$ [24]. Both the central and the forward muon system provide three layers of detectors, referred to as A, B, and C layers. The detectors in each layer consist of both drift tubes and scintillators. The innermost layer, the A-layer, is inside an iron toroid with a magnetic field of approximately 1.8 T, while the two outermost layers, the B- and C-layers, are outside the toroid.

In the central muon system, the layer of scintillators inside the toroid is known

as the A-$\phi$ layer. These counters have a $\phi$ segmentation of approximately 4.5 degrees. The outer layers of scintillators are much larger, with an average size of 50 cm by 150 cm. The central system also uses proportional drift tubes to track particles.

The forward system uses three layers of pixel scintillators combined with three layers of mini-drift tubes. The pixel counters have a $\phi$ segmentation of 4.5 degrees and an $\eta$ segmentation of 0.1. Each layer of the forward muon system consists of eight octants. This gives a total of 4608 pixel counters. Tracking in the forward system is accomplished with mini-drift tubes. The mini-drift tubes are constructed with eight cells with a cross-section of 1 cm by 1 cm. The layer nearest the interaction point has four such decks, while the two outer layers of mini-drift tubes contain three such decks.

The scintillators are the most important part of the muon system for the discovery of CMSPs. An accurate time-of-flight measurement is crucial for the identification of slow-moving particles that travel through the muon system. The expected time resolution of the scintillators will allow slow-moving CMSPs to be identified and relativistic background muons to be rejected, resulting in a very clean channel for discovery.

The time between successive bunches of particles in the Tevatron is 396 ns. This results in a collision rate of approximately 2.5 MHz. This event rate is much larger than the rate at which data can be recorded. Furthermore, only a small fraction of these events will contain an inelastic collision, which is the primary physics interest of the experiment. It is the role of the trigger system to reduce the event rate to a manageable level while ensuring that events with an interesting physics signature are retained.

The DØ experiment uses a three-tier trigger system. The three trigger tiers are referred to as Level 1, Level 2, and Level 3 (L1, L2, and L3). The L1 system is a hardware-based system. Each detector subsystem uses electronics to analyze the detector signals and decide if there are any physics objects in the event. For example, in the muon system there are several L1 trigger conditions that have been implemented. One commonly used L1 muon trigger condition requires scintillator hits in two separate layers and proportional tube wire hits in at least one layer. All these hits are required to be in the same octant of the detector.

L1 trigger decisions are based on the information from a single subdetector only.[3] After an L1 accept has been issued, the detector information is passed on to the L2 trigger system. The L1 trigger system reduces the event rate to approximately 2 kHz.

The L2 system can combine information from multiple subdetectors to form more complicated trigger decisions. The L2 system utilizes single-board computers and can perform simple algorithms on the detector data to make a trigger decision. If an L2 accept is issued, the event data is forwarded to the L3 system. The L2 system reduces the event rate to approximately 1 kHz.

The L3 system consists of a farm of computers that utilize the complete information from all subdetectors to form a trigger decision. The L3 farm runs a simplified version of the complete reconstruction software to reconstruct all physics objects (such as muons, electrons, and jets). Only after the event has been accepted by L3 is the event written to permanent storage. The rate of events passed by L3 is approximately 50 Hz.

[3]There are exceptions to this statement. The L1 muon system communicates with the L1 Central Track Trigger system. This provides a measurement of the momentum of the muon which can be implemented in a trigger condition.

# CHAPTER 4

# MUON RECONSTRUCTION

The reconstruction of muons in the DØ detector is performed in several stages. First, the individual hits in the various detectors are reconstructed from the electronics signals. The hits in a specific layer (A and B/C) are then combined to form a muon segment. The muon segments inside and outside the toroidal magnet are then combined to form muon tracks. Finally, an attempt is made to match tracks in the muon system to tracks reconstructed in the central tracking system.

## A. Muon Hits

When a phototube in a muon scintillator fires (presumably from the passage of a muon or other charged particle), the time that the signal was received is attached to the hit. However, the muon system has been designed so that a beam-produced, speed-of-light muon should arrive at a time of zero. This is accomplished by subtracting a "T0" at the front-end. These T0's are determined from data and are periodically updated [25]. A reconstructed muon scintillator hit contains the location of the scintillation counter and the time the hit was recorded (minus the T0). The timing information in the scintillators allows for the rejection of cosmic-ray muons, as the timing for an in-going muon will be

different than that for an out-going muon.

Tracking in the muon system is accomplished with drift tubes. In the central muon system, the anode wires for two adjacent cells in the proportional drift tubes (PDTs) are attached. A 20 ns delay is implemented between the two wires. The signal from the anode wire is then read out on both wires, resulting in two times. These two times can then be used to calculate both the time for the signal to propagate along the wire (the axial time) and the time for the ions to drift to the anode wire (the drift time). Since the drift speed in the chamber gas and the speed of the signal along the wire are known, the position of the hit along the wire and the distance of the charged particle from the wire can both be calculated.

The mini-drift tubes (MDTs) in the forward muon system are only read out on one end of the wire. Hence, there is no information about the position of the hit along the anode wire. The MDT hits are combined with a scintillator hit in the same layer and octant to get a rough measure of the position of the hit along the wire.

## B. Muon Segments

A linked-list algorithm is used to reconstruct muon segments [26]. Segments are straight-line tracks that are reconstructed using either only A-layer wire hits or only B/C-layer wire hits. Since there is no magnetic field in between the B- and C-layers of the muon system, the muon track should form a straight line in the B- and C-layers and hence all hits in both layers are used to create a single segment. The first step of this algorithm is to take all possible combinations of pairs of wire hits and construct a segment for each pair of hits that are near each other.

An attempt is then made to combine some of these two-hit segments in order to create a segment with more hits. A $\chi^2$ is calculated for each reconstructed segment as a measure of the goodness of the fit. Each of the reconstructed muon segments has an associated 3-dimensional position in the detector and a set of angles that determine its direction.

## C. Muon Tracks

Muon tracks use the reconstructed muon segments to form the track of a muon through all layers of the muon system. The algorithm first takes pairs of segments, one A-layer segment and one B/C-layer segment. The two segments are required to be consistent in both position and direction by comparing the positions of the extrapolated segments at the midpoint between the two segments.

The toroid magnet is located between the A-layer and the B/C-layers. By measuring the bend of track between the A- and B/C-layers, the momentum of the muon can be calculated. However, the momentum resolution of the muon system is much poorer than the momentum resolution of the central tracking system [27]. The momentum resolution ($\Delta p/p$) for the central tracking system is approximately 11% for a muon with a momentum of 50 GeV/c [28]. The momentum resolution for a 50 GeV/c muon using only the muon system is approximately 60% [28]. Hence, the momentum measured in the muon system is only used when the the muon track has not been matched to a reconstructed track in the central tracking system.

## D. Central Track Matching

Since the momentum resolution of the central tracker is much better than the momentum resolution of the muon system, an attempt is made to match muon tracks to tracks reconstructed in the central tracking system. This matching is performed for both "complete" muon tracks (containing both an A-layer and a B/C-layer segment), and for A-layer and B/C-layer segments that do not have a matching segment in the other layer. This improves the muon reconstruction efficiency, particularly for low momentum muons that do not penetrate the toroid.

The first step of this matching is to extrapolate the muon track back to the central tracking system and predict in what region a matching central track should be found. A $\chi^2$ variable is constructed for each of the central tracks in the selected region based on the difference on spatial position of the A-layer muon segment and the central track extrapolated to the A-layer. The matching central track is selected as the central track giving the lowest $\chi^2$.

## E. Time-of-Flight Corrections

The time resolution of the central muon scintillation counters can be improved by performing a time-of-flight correction. There are two parts to this correction. One involves correcting for the actual path length traveled to the scintillator and the second is a correction for the time it takes the light to propagate within the scintillator. The size of these corrections is determined from data. These corrections were applied to the segment times starting in software release p14. They result in a modest improvement in time resolution [29].

Each scintillator channel in the detector has a constant (the "T0") subtracted

in the hardware from the actual value read out. The purpose of the T0 is to move the peak of the muon timing distribution to zero. That is, all real, beam-produced muons should register (within the detector resolution) with a time of zero. However, as shown in Figure 4.1, this T0 is for "ideal" muons that arrive at the center of the counter.[1] In general, a muon will not arrive at the center of the counter. This has two effects. First, the path length of the muon from the vertex to the scintillator will be different than in the ideal case. Since all muons are traveling at the speed of light, this will cause non-ideal muons to have slightly different times than ideal muons. Furthermore, it takes some amount of time for the light to propagate from where the particle struck the scintillator until it reaches the phototube. This should be proportional to the deviation noted in Figure 4.1. Two corrections are made, one for each of these effects, in an attempt to improve the timing resolution of the muon scintillation counters.

Raw data from several different runs was processed using a custom version of the `muo_examine` program. Only "tight" muons are used in the calculations.[2] The relevant information for tight muons is written into an ntuple, which is then analyzed to find the corrections.

Corrections are only performed for the central muon system. Due to the small size of the pixel scintillation counters in the forward muon system, any correction would have a negligible effect on the time resolution. The central scintillation counters are much bigger (particularly the B- and C-layer counters). Hence, the

[1] Actually, this is not quite correct. Since the T0s are calculated by looking at data from real muon events, it will be the average position of the muons striking the counter. Since the muon system has a box geometry, this will not generally correspond to the actual center of the counter. This is further complicated by the actual location of the phototube in the detector.

[2] Tight muons are required to have more than 1 A-layer wire hits, 1 or more A-layer scintillator hits, greater than 2 B/C-layer wire hits, 1 or more B/C-layer scintillator hits, and a converged local fit ($\chi^2 > 0$).

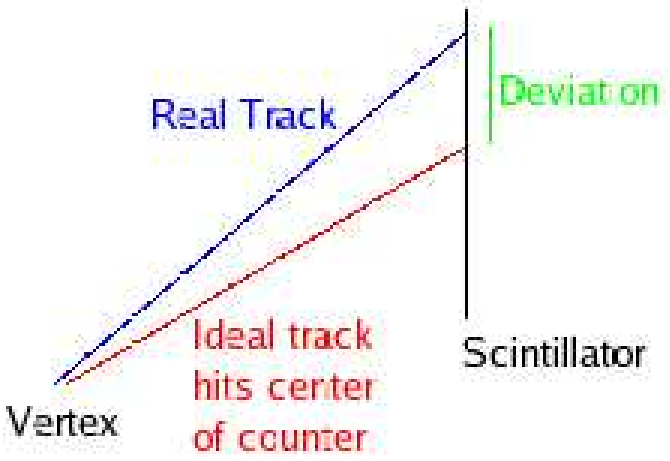


Figure 4.1: Idealized view of a muon scintillator. Ideal muons (red) hit the scintillator (black) in the center. Real muons (blue) do not hit in the center of the scintillator. This means that the total distance traveled from the vertex to the scintillator is different for real muons and ideal muons. There is also some time delay for the light to propagate in the scintillator itself (deviation in green).

corrections should have a noticeable effect on the time resolution of the central muon counters.

The information from the muon system is first processed by the reconstruction software to form hits. The scintillator hits are then used in conjunction with the hits from the muon tracking chambers (PDTs in the central muon system and MDTs in the forward muon system) to form segments. Segments are reconstructed separately in the A-layer and together in the B- and C-layers. Segments are then combined to form muon tracks, and finally reconstructed muons. It was decided that the actual time registered for the hit will be left unchanged. The time-of-flight corrections are applied to the times returned by the A-layer segments and the B/C-layer segments. The actual corrections are performed in the `LocalSegment` class of the `muo_segmentlinkedlist` package. In the p14 release, the corrections are performed in the `LocalSegment::getSegment()` method, while in the p17 release it has been moved to `LocalSegment::TOFCorrectedTime()`.

The first correction applied is to correct for the difference in time for a speed-of-light muon based on the difference in path length between an ideal muon and the actual muon. This correction is performed by first calculating the ideal distance measured from the center of the detector.[3] The real hit position in the scintillator is then calculated by extrapolating the muon segment parameters to the plane of the scintillator. The real distance is taken to be the distance from the center of the detetctor to the real hit position. The difference between the ideal distance and the real distance is then divided by the speed of light to determine the path length correction to the segment time.

[3]Note that this is not measured from the vertex of the event. The distance is calculated from the center of the detector ( (0,0,0) in cartesian coordinates).

The next correction is proportional to the deviation between the actual hit position in the scintillator and the center of the counter. Only the deviation along the long axis of the scintillator was used in the correction. The corresponds to the $z$-direction (along the beam axis) for the A-layer, B-layer, and bottom C-layer counters, but the $\phi$ direction for the remaining C-layer counters. In each case, plots were made of the time versus the deviation. A linear fit was performed to find the correction factors. The details for A-, B-, and C-layer counters are described below.

The long axis of the central A-layer counters (or A/$\phi$ counters) is in the $z$-direction (along the beam axis). Figure 4.2 shows such a plot. The "V" shape of this plot is expected. Muons hitting the center of the counter will register the smallest time, while muons hitting off-center in either direction will register larger times due to the additional time required for the light to propagate to the phototube.

A linear fit is performed separately for negative deviations and for positive deviations. The slope of these two fits was found to be nearly identical. The fit was performed for counters read out by a particular Scintillator Front-End card (SFE), and then the slopes were averaged over all SFE's [30]. The slope used to find the p14 correction is 0.085 ns/cm. This was an initial estimate. A closer analysis of the data revealed that a slope of 0.044 ns/cm was optimal. This improved correction is used in p17.

The long axis of the side B-layer scintillators (octant 4 and 7) are also in the $z$-direction. Figure 4.3 shows a plot of time versus $z$-deviation for counters read out by SFE 0x18. A linear fit was performed and the final correction was calculated by averaging over the slopes calculated from the two side B-layer SFE's (0x18

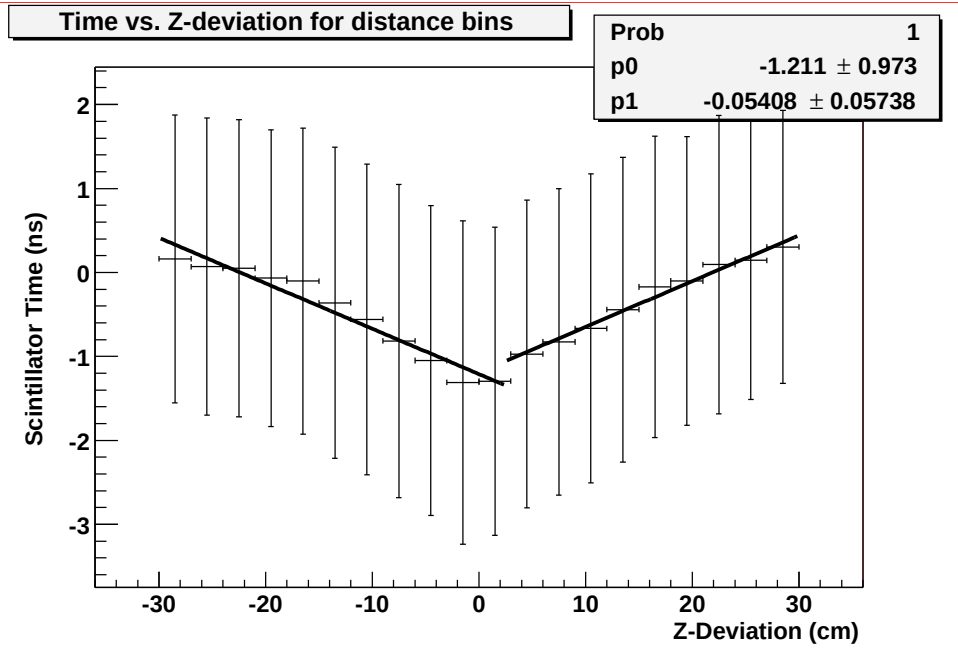


Figure 4.2: A plot of time versus deviation from the center of the counter in the $z$-direction for A-layer scintillators. Plot shows muons in SFE 0x00.

and 0x1E). The slope used to compute the correction in p14 is 0.045 ns/cm. This correction is unchanged for p17.

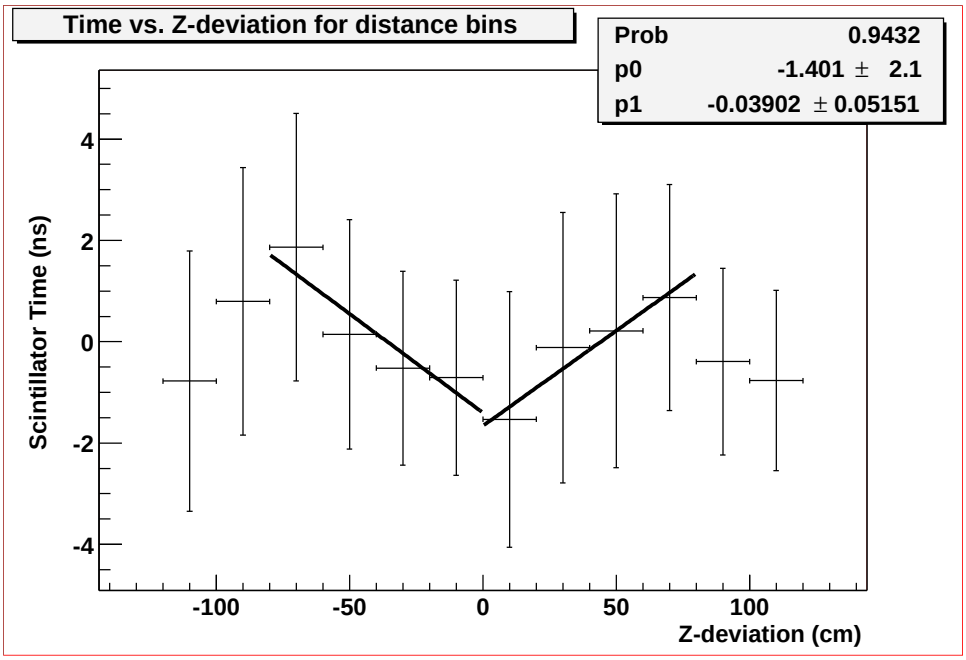


Figure 4.3: A plot of time versus deviation from the center of the counter in the $z$-direction for B-layer scintillators. Plot shows muons in SFE 0x18.

The bottom B-layer scintillators (octants 5 and 6) also have their long axis in the $z$-direction. However, the counters are different than those used in the side B-layer, and so the corrections are calculated separately. Figure 4.4 shows the time versus $z$-deviation for counters in SFE 0x1D. The slopes from all bottom B-layer SFEs were averaged to calculate the correction factor. Both p14 and p17 use a correction of 0.05 ns/cm.

The long axis of the side and top C-layer scintillator counters (octants 0-4, 7) is in the $\phi$ direction. Figure 4.5 shows a plot of time versus $\phi$ deviation for SFE 0x2E. Plots and fits were made separately for each suboctant and then averaged to find the final correction. Both p14 and p17 use a slope of 0.045 ns/cm to

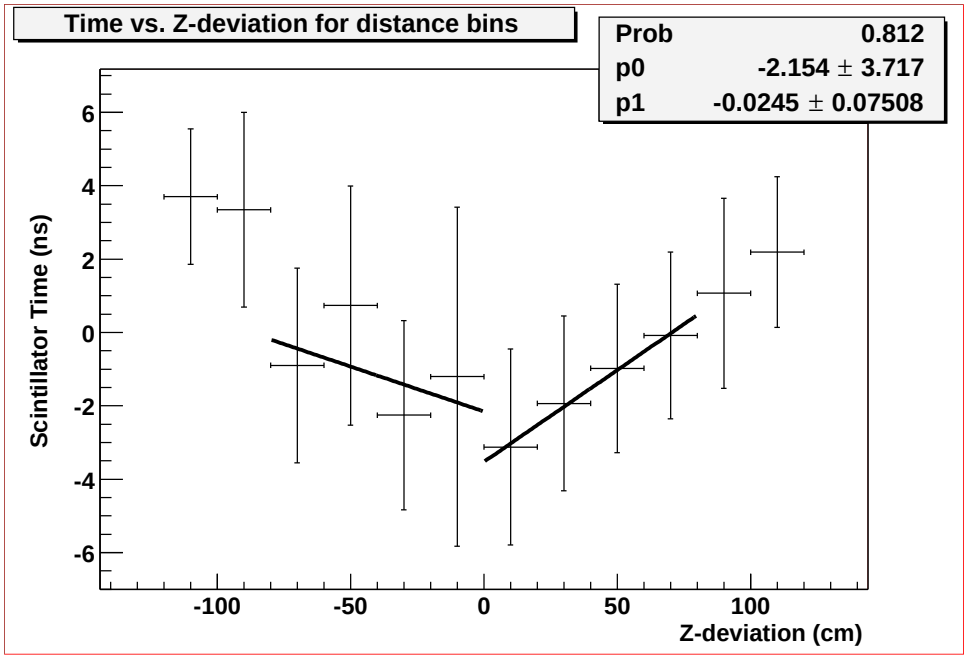


Figure 4.4: A plot of time versus deviation from the center of the counter in the $z$-direction for B-layer scintillators. Plot shows muons in SFE 0x1D.

compute the correction.

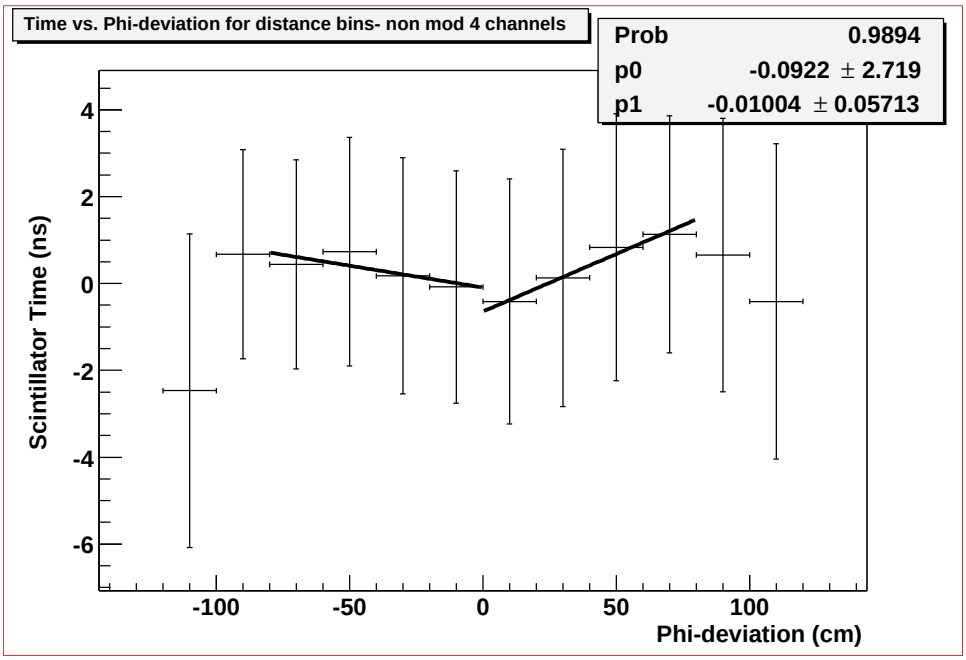


Figure 4.5: A plot of time versus deviation from the center of the counter in the $\phi$-direction for C-layer scintillators. Plot shows muons in SFE 0x2E.

The long axis of the bottom C-layer scintillators (octants 5 and 6) are in the $z$-direction. Figure 4.6 shows a plot of time versus $z$-deviation for counters in SFE 0x2A. After averaging over all SFEs the final slope used to compute the correction is 0.05 ns/cm in both p14 and p17.

After applying both the corrections for the path length difference and for the light propagation time in the counter, the mean of the timing distributions was shifted away from zero. A final offset correction was subtracted to shift the mean back to zero. The value of the offset and the deviation corrections are summarized in Table 4.1.

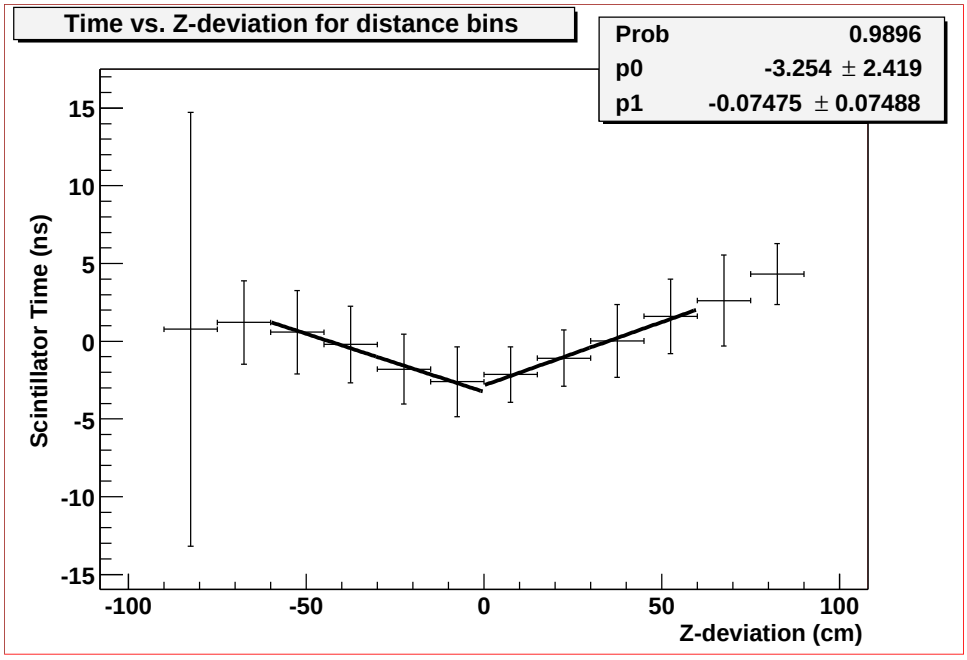


Figure 4.6: A plot of time versus deviation from the center of the counter in the $z$-direction for C-layer scintillators. Plot shows muons in SFE 0x2A.

Table 4.1: Summary of Time-of-Flight Correction Factors

| Counter type | p14 z/phi deviation slope (ns/cm) | p17 z/phi deviation slope (ns/cm) | p14 offset (ns) | p17 offset (ns) |
|---|---|---|---|---|
| A-layer | 0.085 | 0.044 | 2.0 | 1.0 |
| Side B-layer | 0.045 | 0.045 | 1.0 | 1.0 |
| Bottom B-layer | 0.050 | 0.050 | 2.0 | 2.0 |
| Side/top C-layer | 0.045 | 0.045 | 2.5 | 2.5 |
| Bottom C-layer | 0.050 | 0.050 | 2.0 | 2.0 |

Once the corrections were applied, the effect on the scintillator timing resolution was studied. Table 4.2 summarizes the resolution of each scintillator type, as calculated from a Gaussian fit to the timing distribution. Figures 4.7, 4.8, 4.9, 4.10, and 4.11 show the timing distributions both before and after the corrections are applied.

Table 4.2: Summary of scintillator timing resolutions before and after corrections.

| Counter type | Raw (Uncorrected) resolution (ns) | Corrected Resolution (ns) |
|---|---|---|
| A-layer | 2.1 | 2.0 |
| Side B-layer | 2.8 | 3.0 |
| Bottom B-layer | 3.7 | 3.1 |
| Side/top C-layer | 4.5 | 3.8 |
| Bottom C-layer | 3.5 | 2.5 |

The corrections are effective in improving the resolution of the bottom B-layer and all C-layer counters. This is likely due to the fact that these counters are the largest. Hence, the path length differences and light propagation times for these counters are large. The resolution of A-layer and side B-layer counters does not noticeably improve with these corrections, likely due to the smaller size of these counters. It is unlikely that the scintillator timing resolution can be improved to much better than 2 ns. The size of the timing readout bins are approximately 1 ns. The optimal resolution is therefore less than 1 ns. However, it is not possible to calibrate the counters well enough to acheive this resolution.

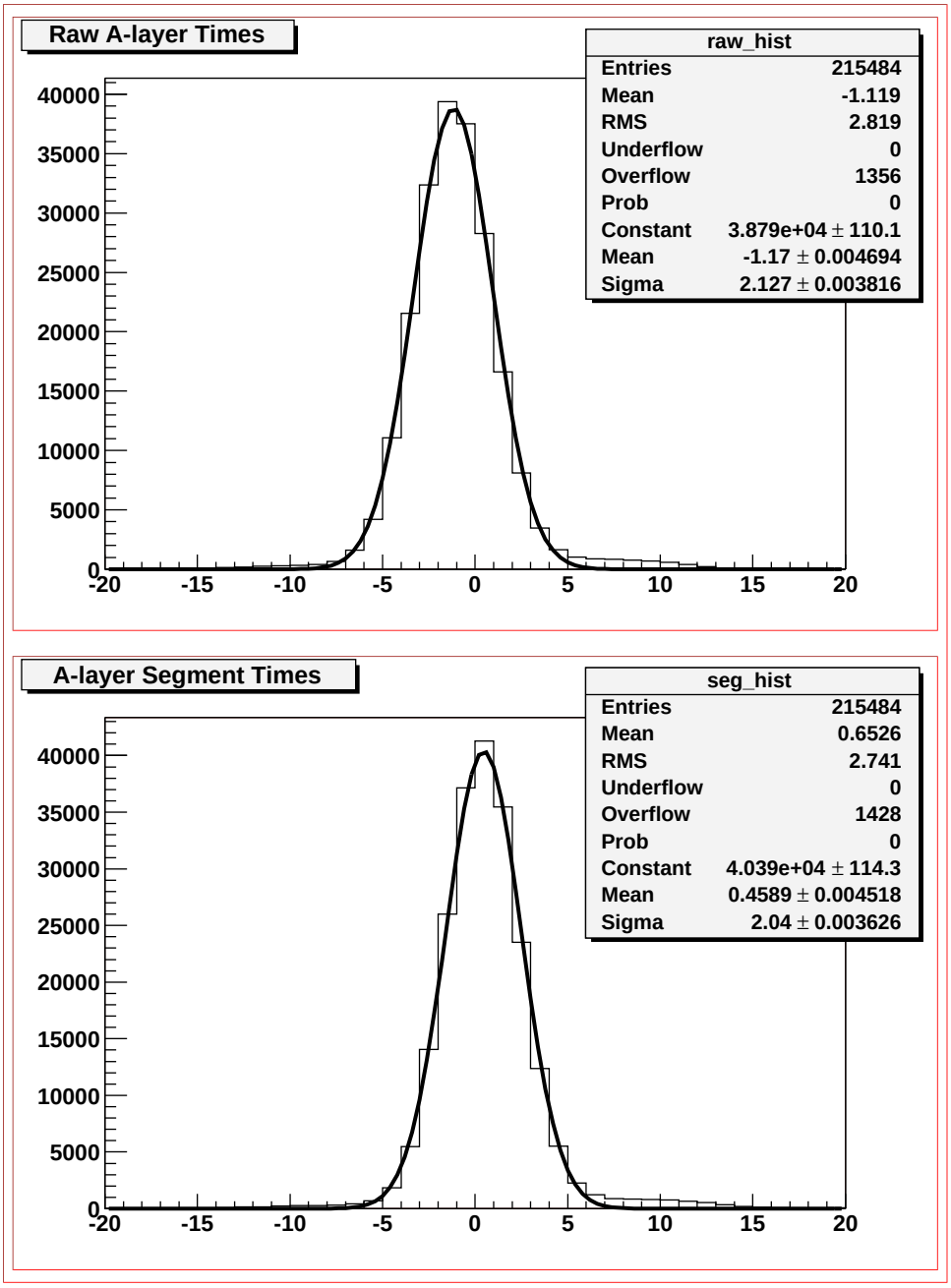


Figure 4.7: Timing distributions (in ns) for raw (uncorrected) and corrected scintillator times for A-layer counters. Both distributions are fit with a Gaussian.

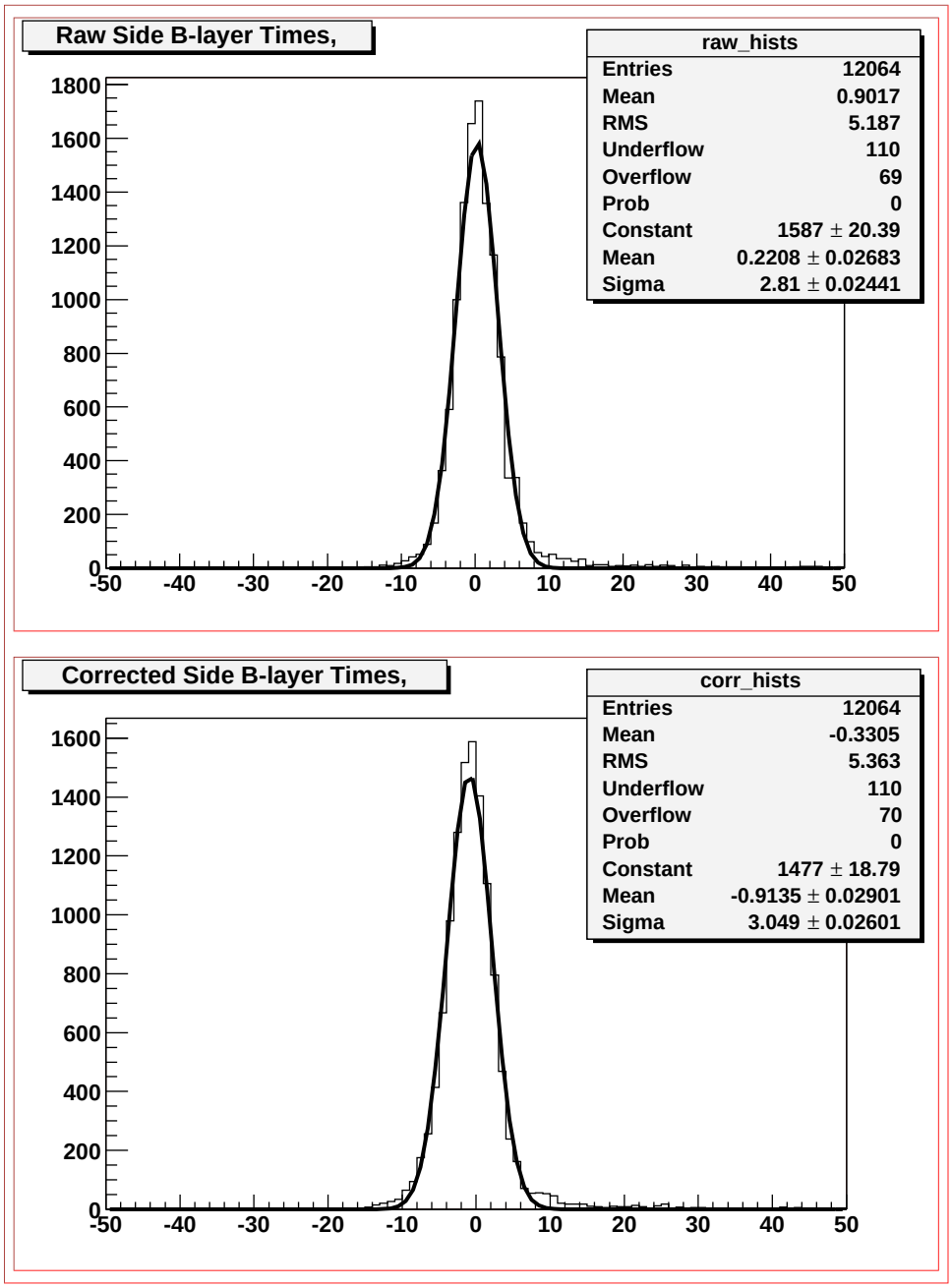


Figure 4.8: Timing distributions (in ns) for raw (uncorrected) and corrected scintillator times for side B-layer counters. Both distributions are fit with a Gaussian.

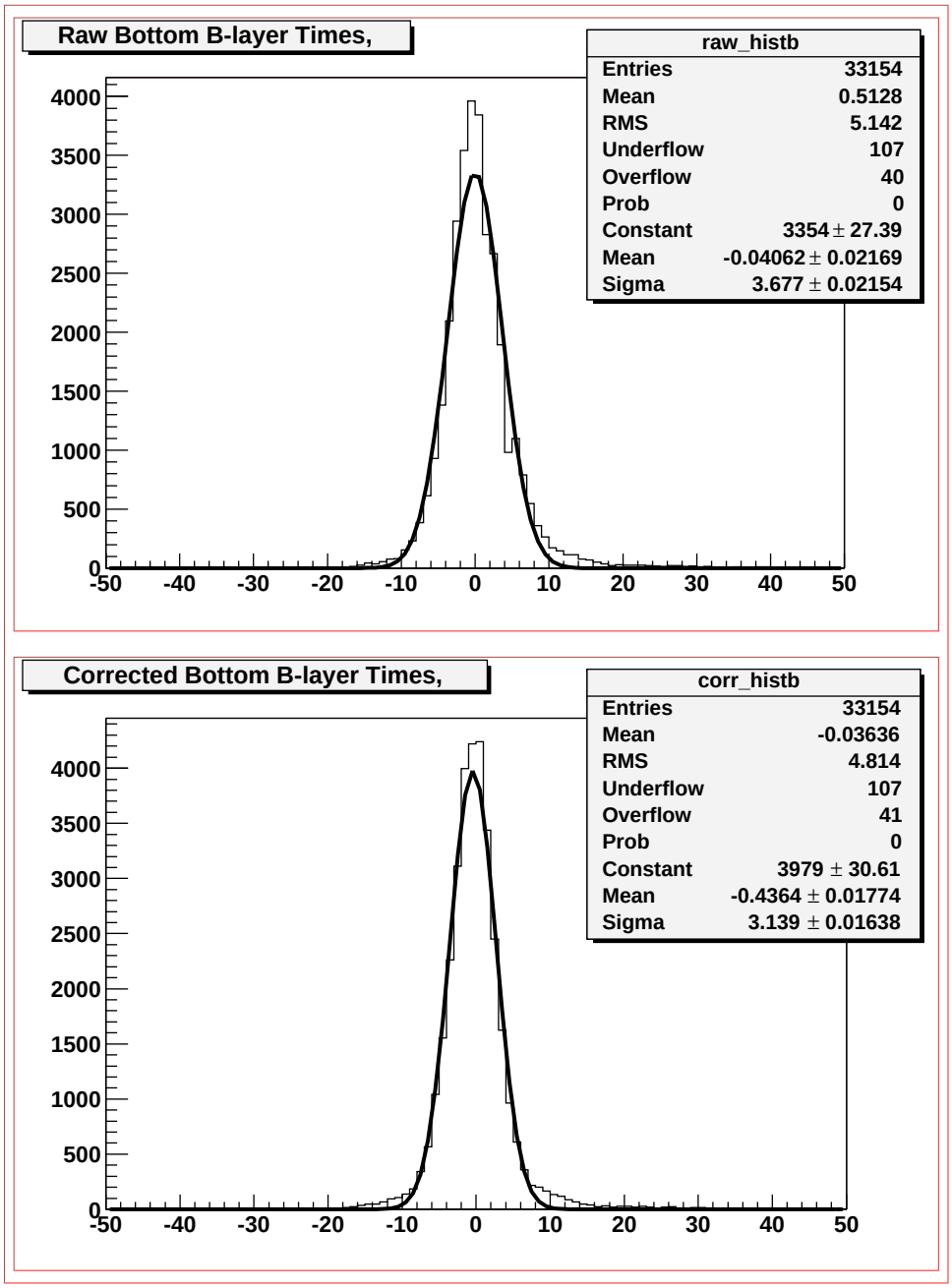


Figure 4.9: Timing distributions (in ns) for raw (uncorrected) and corrected scintillator times for bottom B-layer counters. Both distributions are fit with a Gaussian.

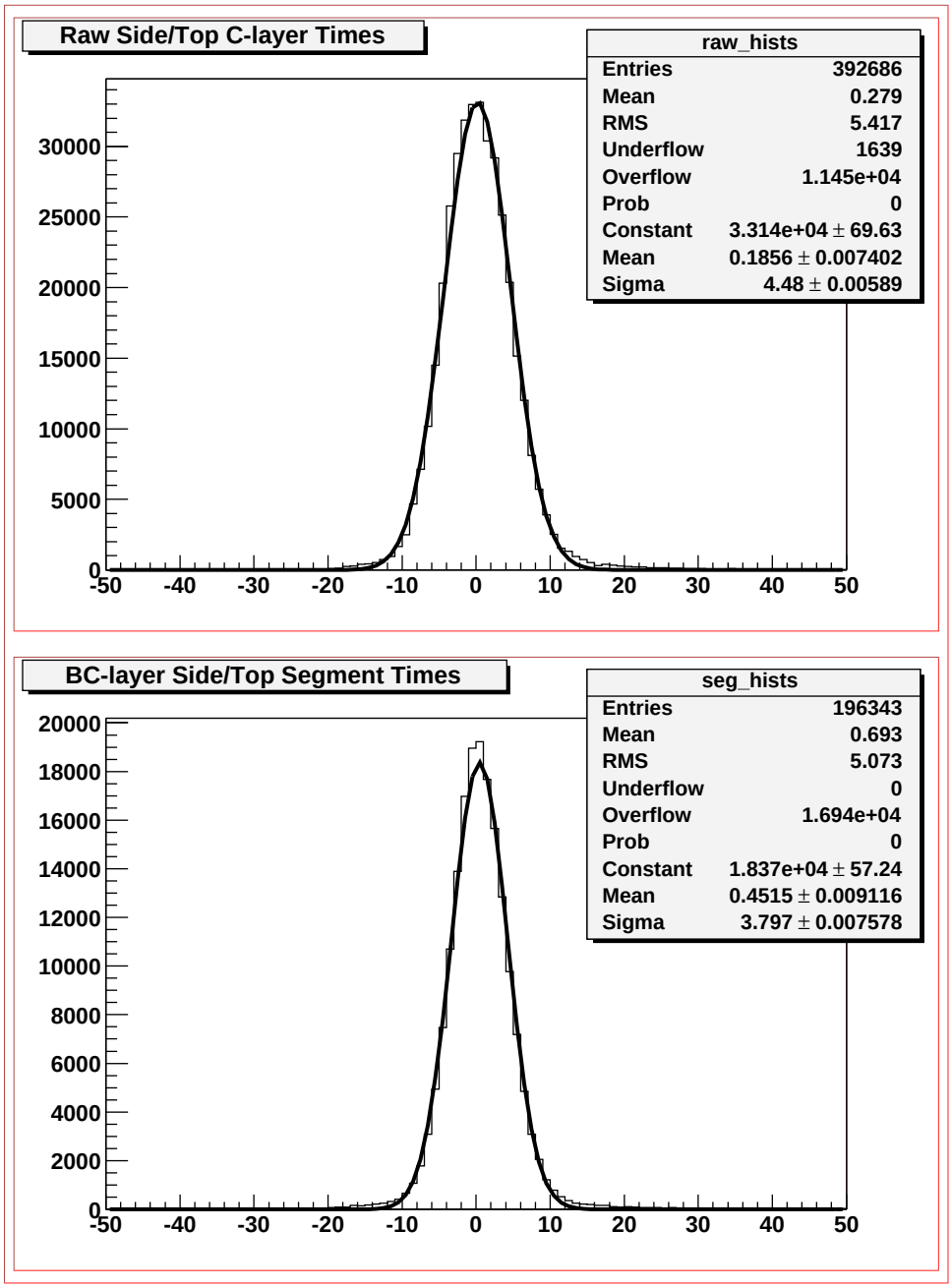


Figure 4.10: Timing distributions (in ns) for raw (uncorrected) and corrected scintillator times for side/top C-layer counters. Both distributions are fit with a Gaussian.

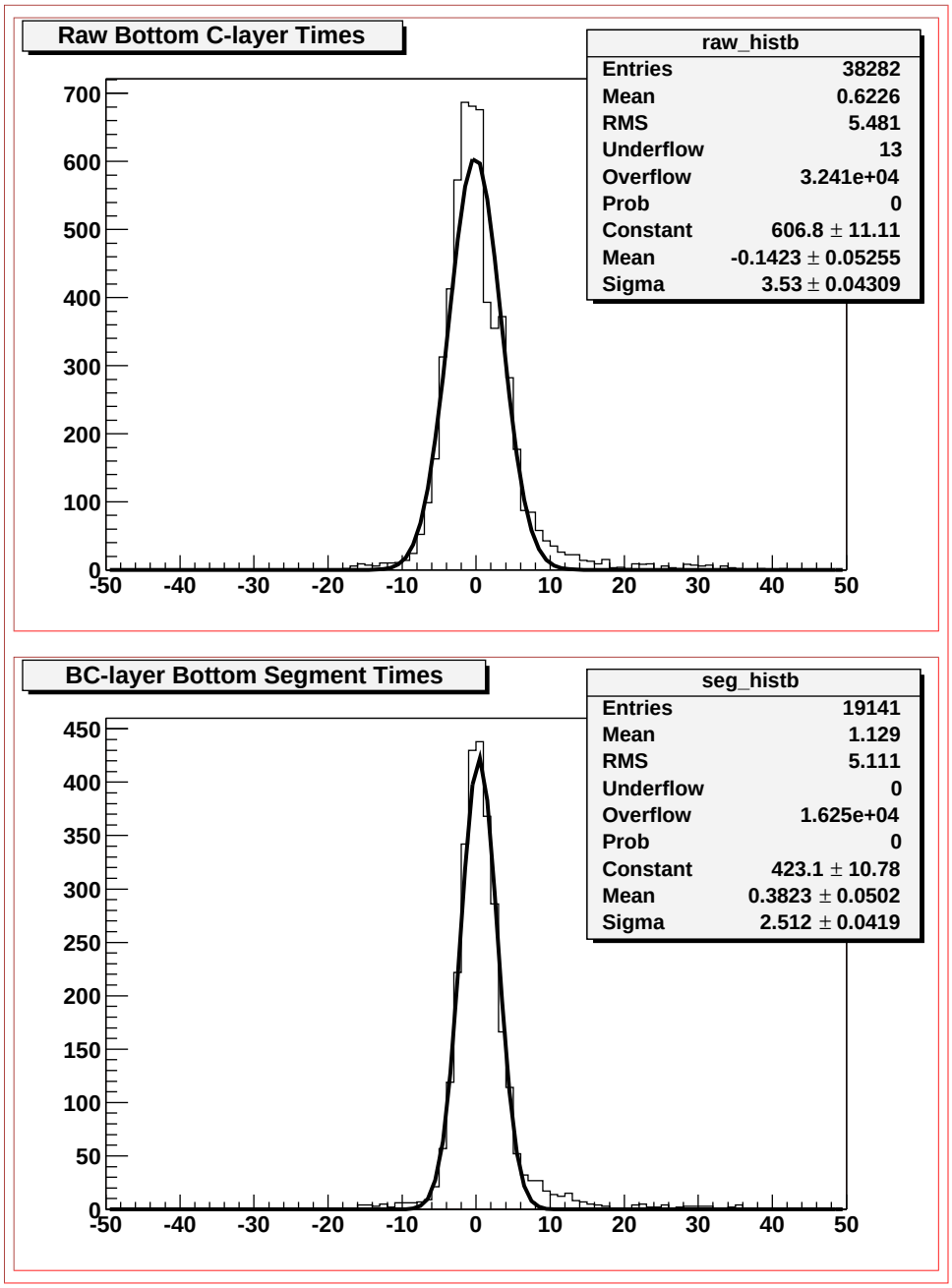


Figure 4.11: Timing distributions (in ns) for raw (uncorrected) and corrected scintillator times for bottom C-layer counters. Both distributions are fit with a Gaussian.

# CHAPTER 5

# THE STAU ANALYSIS

The DØ detector is used to search for charged massive stable particles. These particles have a lifetime long enough to escape the detector before decaying. Since the CMSP will penetrate all layers of the detector, it will appear similar to a muon. However, the massive CMSP will be moving much slower than a beam-produced muon. The timing information from the muon scintillation counters is used to measure the speed and separate candidate CMSPs from muons. This chapter describes a search for stable staus in a GMSB model. These are preliminary results that have not yet been published, but have received approval to be shown outside the DØ collaboration [31].

The GMSB model used in this analysis is a model with a stau NLSP. It is referred to as "Model Line D" from the Snowmass 2001 Direct Investigations of Supersymmetry Subgroup [32]. The parameters of this model are shown in Table 5.1. If the stau decays to the gravitino/goldstino are sufficiently suppressed (through a large value of the $C_{grav}$ parameter), then the stau lives long enough to escape the detector. If the stau NLSP is stable, then all heavier SUSY particles will first decay to a stau before decaying to the gravitino/goldstino LSP. However, the signature of these cascade decays in the detector is quite model-dependent and can be difficult to simulate accurately. In this analysis, only the pair-production of the lightest staus is considered. This means that each signal

event will contain exactly two stable staus. However, this analysis will also have some sensitivity to events containing CMSPs produced in cascade decays. The background estimates are unchanged for such topologies but the (highly model-dependent) signal acceptance will be different than that quoted for this analysis.

Table 5.1: GMSB Model Parameters

| Parameter | Description | Value |
|---|---|---|
| $\Lambda_m$ | Scale of SUSY breaking | 19 to 100 TeV |
| $M_m$ | Messenger mass scale | $2\Lambda_m$ |
| $N_5$ | Number of messenger fields | 3 |
| $\tan\beta$ | Ratio of Higgs VEVs | 15 |
| sgn $\mu$ | Sign of Higgsino mass term | +1 |
| $C_{grav}$ | Factor multiplying effective mass of gravitino | 1 |

# A. Signal Sample

Pythia 6.202 and DØReco version p14.08.00 were used to generate pair produced stable staus [33]. Samples were generated by varying the GMSB $\Lambda$ parameter from 19 TeV to 100 TeV. One-hundred-thousand events were generated for stau mass points of 60, 100, 150, 200, 250, and 300 GeV/c$^2$.

The full GEANT-based DØ detector simulation does not contain any massive stable particles. So, in order to simulate the detector response the Pythia-generated samples were processed with a Parameterized Monte-Carlo Simulation (PMCS) of the detector. This PMCS simulation performs muon momentum and position smearing and includes trigger and muon identification efficiencies. The efficiencies used were identical to the efficiencies computed for the $Z \rightarrow \mu\mu$ cross-section analysis [34].

The PMCS simulation of the detector does not simulate the timing in the muon scintillators. A modified version of PMCS was created that correctly simulated the timing response of the muon scintillators in response to both speed-of-light and slow-moving particles.

The speed of the Monte-Carlo particle and the distance traveled to reach a particular scintillator detector is known, so time taken to reach the scintillation counter can be calculated. However, the timing in the DØ muon system is designed so that a speed-of-light particle will be read out with a time of zero. This is accomplished by subtracting a value (known as the T0) at the front-end. In order to accurately model the read-out times for the scintillators, it is necessary to subtract this T0. Since varying cable lengths preclude the use of the actual T0's used by the front-ends, the T0 for each scintillator is estimated as the time for a speed-of-light particle to reach the center of the counter. Figure 5.1 shows the time of muons in data compared to the simulated time for staus with mass 100 GeV/$c^2$ and 300 GeV/$c^2$. The scintillator times in the detector are read out in units of approximately 1 ns.

The timing resolution of the muon scintillators was determined from a sample that contained all muons identified as tight (according to the muon ID requirements) in the entire data sample [28]. This sample consisted of over 43 million muons. Since there are several different types of scintillation counters used at DØ, the times for these muons were histogrammed separately for the three forward pixel planes (A, B, and C), central A-layer, central side B-layer, central bottom B-layer, central side/top C-layer, and central bottom C-layer. The resolution and offset (since the timing distributions may not be centered exactly at zero) was taken from a gaussian fit to these histograms. The computed resolutions and

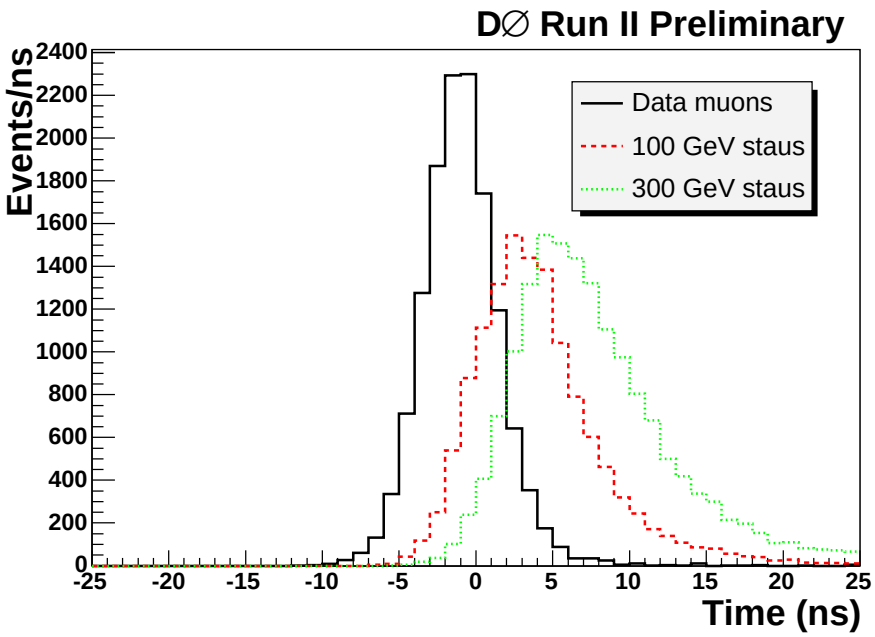


Figure 5.1: A-layer scintillator times for muons from data (black) compared to the simulated time for staus of mass 100 GeV/$c^2$ (red) and 300 GeV/$c^2$ (green). No cuts have been applied to the stau sample. Histograms are normalized to approximately the same number of events.

offsets are shown in Table 5.2.

Table 5.2: Measured Scintillation Counter Resolutions and Offsets

| Scintillation Counter | Resolution (ns) | Offset (ns) |
|---|---|---|
| Forward A-layer | 2.19 | -0.04 |
| Forward B-layer | 2.28 | -0.06 |
| Forward C-layer | 2.38 | 0.02 |
| Central A-layer | 2.30 | -0.06 |
| Central side B-layer | 2.37 | -0.41 |
| Central bottom B-layer | 3.41 | -0.22 |
| Central side/top C-layer | 3.41 | -0.11 |
| Central bottom C-layer | 3.32 | 0.23 |

As a check of the scintillator timing simulated in PMCS, a sample of muons from Z-boson decays in data was compared to a sample of muons from Z-boson decays simulated with Pythia and PMCS. There is good agreement in the timing distributions for the two samples. Figure 5.2 shows the timing distribution for muons in data and PMCS for the forward muon scintillation counters.

Since the coverage of the muon scintillators is not 100% and the efficiency of the scintillation counters is not perfect, it was necessary to implement an efficiency map. A total of eighteen such maps were generated: three each for the three planes of the north and south pixel planes and four (top, bottom, east, and west) for each of the three layers of the central system. These maps were calculated from a sample consisting of all tight (according to muon ID definitions) muons with central track matches in the entire data sample. Each scintillator plane was divided into 10 cm by 10 cm bins. The central track matched to the muon was then extrapolated to the plane. It was then determined if that muon had a scintillator hit in that plane. The efficiency of each bin was determined as the number of muons with scintillator hits in that bin divided by the total

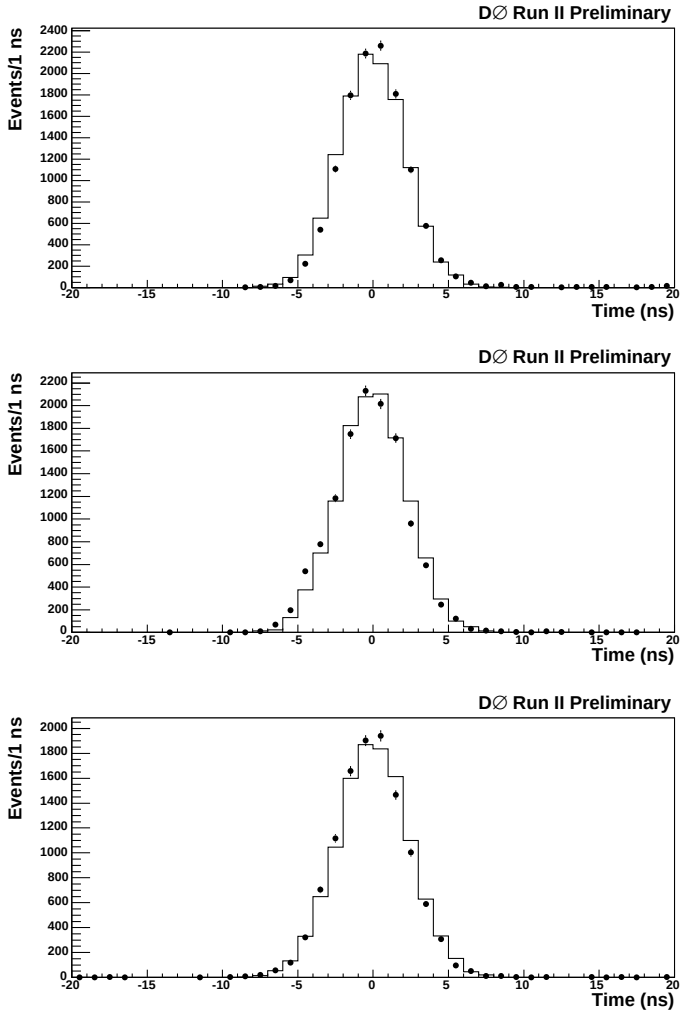


Figure 5.2: Timing in the forward muon scintillation counters for muons in data (points) and muons simulated with PMCS (line). The top plot is for a forward A-layer counters, the middle plot is for the forward B-layer counters, and the bottom plot is for the forward C-layer counters. The histograms are normalized to the same number of events.

number of muons in that bin. Figure 5.3 shows the distribution of muons in data with scintillator hits in the north C-layer scintillator plane. Figure 5.4 shows the distribution of staus in PMCS that have scintillator hits in the north C-layer scintillator plane.

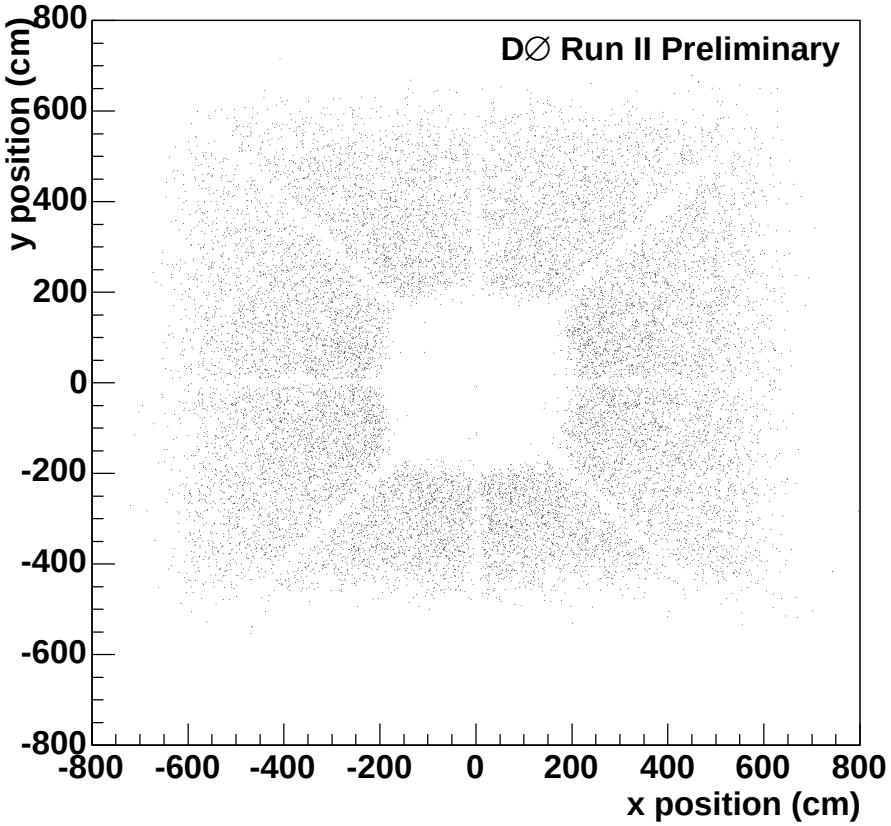


Figure 5.3: Distribution of muons in data with scintillator hits in the north C-layer pixel plane.

Since the CMSPs may be moving at a speed substantially smaller than the speed of light, another concern is whether or not the particles can cause a trigger. This analysis uses triggers based on hits in the muon scintillation counters. There is a trigger gate (which varies for different regions and layers) during which the

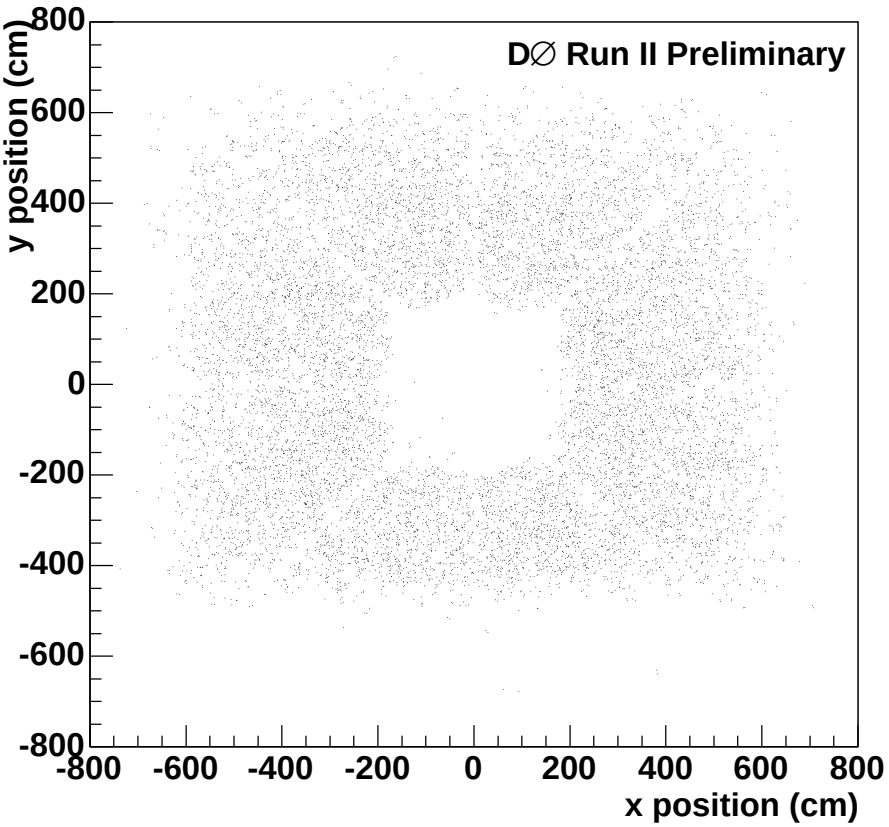


Figure 5.4: Distribution of staus in PMCS with scintillator hits in the north C-layer pixel plane.

signal from the scintillation counter must arrive. Table 5.3 shows the trigger gates for the different areas of the muon system. The trigger gates are adjusted so that beam-produced, speed-of-light muons will arrive in the center of the trigger gate. If the CMSP is moving too slowly, it will arrive at the scintillation counter outside of the trigger gate. Figure 5.5 shows the fraction of staus that will arrive inside the trigger gate for the different layers of the muon system. Although the trigger efficiency drops as the stau mass increases, muon triggers will be fairly efficient for staus in the mass range studied in the analysis.

Table 5.3: Muon System Trigger Gates

| Section | Trigger Gate (ns) |
|---|---|
| Central A-layer | 24 |
| Central side B-layer | 84 |
| Central bottom B-layer | 50 |
| Central side C-layer | 46 |
| Central bottom C-layer | 60 |
| All forward layers | 30 |

# B. Data Sample

The data sample used for the analysis is the common sample groups 2MU pass2 skim [35]. This skim requires two loose muons to be present in the event. This sample covers the data-taking period from April 2002 to August 2004, up to and including version 13 of the trigger list. All data has been reconstructed with version p14 reconstruction software.

To ensure a clean data sample, bad runs have been removed. Runs are required to have been rated as "REASONABLE" in the muon portion of the run

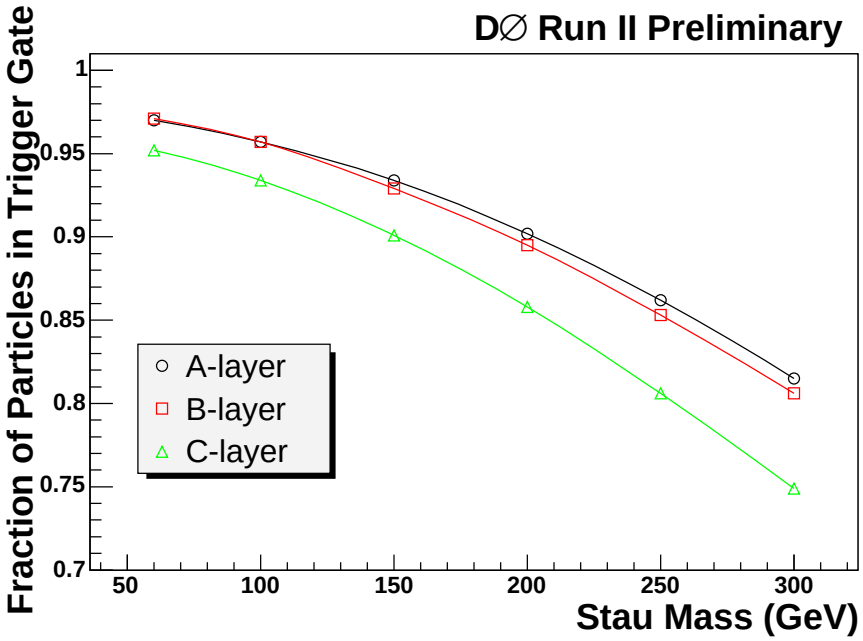


Figure 5.5: Fraction of all staus arriving within the trigger gate versus mass for the three layers of muon scintillation counters.

quality database. Furthermore, since central tracks will be required during the preselection phase, runs are required to not be marked as "BAD" in the SMT and CFT portion of the run quality database. No requirements are made on the calorimeter data quality. Additionally, runs in the range 172359 to 173101 and 174207 to 174217 were removed due to a problem with the dimuon trigger. Bad and duplicate LBNs are also removed.

Dimuon triggers are required in this analysis. These triggers require two scintillator triggers to be satisfied at L1. Both of these L1 scintillator triggers must have scintillator hits in more than one layer. Changes in the trigger list during the data taking period result in a few different L2 and L3 conditions applied to this L1 dimuon requirement. The `runrange_luminosity` program is used to calculate the luminosity for each of the trigger lists used during the

data-taking period. Table 5.4 shows a summary of the different trigger lists, the corresponding trigger, and the integrated luminosity after bad runs have been removed. The total integrated luminosity on the data sample is $390 \pm 25$ pb$^{-1}$.

Table 5.4: Integrated Luminosity by Trigger List

| Trigger List | Trigger Name | Integrated Luminosity ($pb^{-1}$) |
|---|---|---|
| v10 and prior | 2MU_A_L2M0 | 58.47 |
| v11 | 2MU_A_L2M0_TRK10 | 63.45 |
| v12 | 2MU_A_L2M0_TRK5 | 220.03 |
| v13 | DMU1_TK5 | 48.29 |
| total | | 390.24 |

The experimental clock of DØ (used to synchronize the experiment to the accelerator's time structure) has been shown to have a drift of a few nanoseconds on a seasonal basis [36]. The mean of the muon timing distribution versus the run number for forward A-layer scintillation counters is shown in Figure 5.6. In order not to bias the speed calculation based on these scintillator times, the mean of the timing distribution for each run is applied as a correction factor to the data. This run-by-run correction factor results in a slight improvement in the time resolution of the muon scintillators, as shown in Table 5.5. This factor also corrects for runs early in Run II when T0s for some of the muon system had not yet been properly calculated.

## C. Preselection

In order to reduce the data sample to a manageable level, a series of preselection cuts were applied. These cuts were chosen to select a sample of events of good

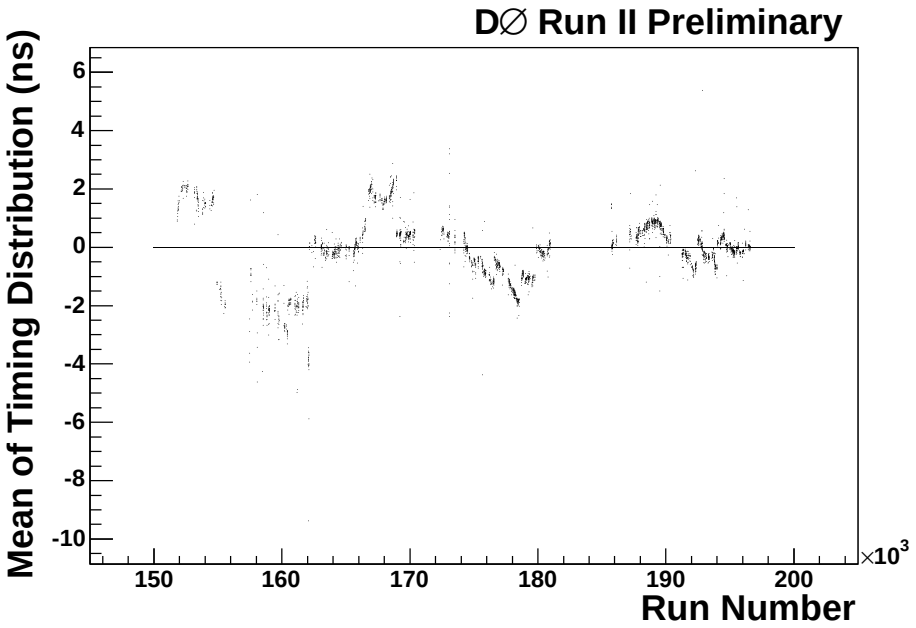


Figure 5.6: The mean of the muon timing distribution versus the run number for forward A-layer muon scintillators. Ideally the mean should be at zero.

Table 5.5: Scintillator time resolutions before and after run-by-run corrections.

| Scintillation Counter | Resolution before correction (ns) | Resolution after correction (ns) |
|---|---|---|
| Forward A-layer | 2.30 | 2.19 |
| Forward B-layer | 2.40 | 2.28 |
| Forward C-layer | 2.48 | 2.38 |
| Central A-layer | 2.55 | 2.30 |
| Central side B-layer | 2.78 | 2.37 |
| Central bottom B-layer | 3.44 | 3.41 |
| Central side/top C-layer | 3.52 | 3.41 |
| Central bottom C-layer | 3.75 | 3.32 |

quality and possessing the possibility of separating signal from background, while still being very efficient for signal events.

Since the search is for the pair production of CMSPs, each event will contain exactly two CMSPs. Each event is required to pass a dimuon trigger. Furthermore, each event is required to have two muons that pass the medium quality requirements, as defined by the muon ID group. However, medium muons in certain regions of the detector may have scintillator hits in only one layer. In order to improve background rejection both muons are additionally required to have scintillator hits in at least two layers. Both muons are also required to be matched to a central track. Since the spatial resolution of the central tracker is much smaller than the spatial resolution of the muon spectrometer, the central track requirement allows for a more precise determination of the distance traveled by the particle in the detector.

The transverse momentum of a stau CMSP is also much larger than that of most muons produced in the detector. So, each muon was required to have a transverse momentum larger than 15 GeV/c. This cut is at least 99% percent efficienct for all stau mass points. Furthermore, CMSP particles with transverse momentum below this value will be moving too slowly to be detected.

Since the search is for pair-produced CMSPs, there should not be any large transverse momentum jets or tracks near the CMSPs. Furthermore, particles from jets may leak out of the calorimeter, resulting in hits in the muon system that can mimic an out-of-time muon. Also, muons produced in the decays of B-hadrons may also mimic the signal. Therefore, at least one of the muons in the event is required to be isolated. The exact isolation cuts are identical to those used in the $Z \rightarrow \mu\mu$ cross-section analysis. Two of the following four requirements

must be met in the event:

1. Sum of the track $p_T$ in a $R = 0.5$ cone around the first muon must be less than 3.5 GeV.

2. Sum of the track $p_T$ in a $R = 0.5$ cone around the second muon must be less than 3.5 GeV.

3. Sum of the calorimeter energy in a hollow cone between $R = 0.1$ and $R = 0.4$ around the first muon must be less than 2.5 GeV.

4. Sum of the calorimeter energy in a hollow cone between $R = 0.1$ and $R = 0.4$ around the second muon must be less than 2.5 GeV.

This cut was found to be over 99% efficient for $Z \rightarrow \mu\mu$ events. The same efficiency is assumed for signal events in this analysis.

Since the signal events should be back-to-back in $\phi$, the two muons in the event are required to have a $\Delta\phi$ larger than 1.0 radians.

As cosmic ray muons can pass through the detector at any time, not just during an accelerator bunch crossing, they could be wrongly identified as a slow-moving particle. So, additional preselection cuts remove cosmic ray muons from the sample. An event is rejected if any of the following conditions are true:

1. Absolute value of the sum of the pseudorapidity of the two muons is less than 0.15.

2. The distance-of-closest-approach to the beamline of either muon is larger than 0.15 cm.

3. The absolute value of the difference in A-layer times of the two muons is larger than 10 ns.

4. The C-layer time minus the A-layer time for either muons is less than -10 ns.

These cuts are very effective at removing muons from cosmic rays. The efficiency of these cosmic cuts on signal events varies from about 90% for low mass staus to about 70% for the highest mass staus.

The timing information from the muon system is used to calculate the speed of each muon in the event. The speed is first calculated in each layer in which the muon has a scintillator hit. The layer speeds are simply the total distance traveled by the muon to reach the counter divided by the time for the muon to reach the counter. (Speed is quoted in units of $c$ throughout this document.) The central track matched to the muon is extrapolated to the plane containing the scintillator hit. The distance is then taken between the scintillator hit position and the production position (assumed to be $x = y = 0$ and the $z$-coordinate is taken to be the $z$ position at the distance of closest approach to the beamline). Due to the timing in the muon system, a T0 must be added back to the scintillator time obtained from the readout. This T0 is estimated as the time for a speed-of-light particle to travel from the center of the detector to the center of the counter.

The uncertainty on the speed calculation in each layer is obtained from the measured time resolution of the muon scintillation counter (see Table 5.2). The speed uncertainty for each layer is calculated from the following relation:

$$\sigma_v = v\frac{\sigma_t}{t} \tag{5.1}$$

Table 5.6 shows the mean value of the uncertainty on the speed for each of the

different type of counters in the muon system.

Table 5.6: Mean value of the speed uncertainty for counters in the muon system

| Scintillation Counter | Mean Value of Speed Uncertainty (units of $c$) |
|---|---|
| Forward A-layer | 0.147 |
| Forward B-layer | 0.094 |
| Forward C-layer | 0.082 |
| Central A-layer | 0.220 |
| Central side B-layer | 0.108 |
| Central bottom B-layer | 0.203 |
| Central side/top C-layer | 0.156 |
| Central bottom C-layer | 0.107 |

Once the layer speed has been calculated for each layer containing scintillator hits from the muons, the average speed and its uncertainty are calculated for the muon. Figure 5.7 shows the calculated speed for real muons in data and for 100 GeV/c$^2$ and 300 GeV/c$^2$ staus. Figure 5.8 shows the two-dimensional distribution of the speed of each muon for muon pairs in data and for 100 GeV/c$^2$ staus.

The final preselection cut is to ensure that the times registered in the different layers of the muon system are consistent with each other. The speed is calculated using the time in each layer of the muon system for which a particle has a hit. These speeds are then combined to find the average speed of the particle. A $\chi^2$ quantity is constructed based on the average speed, the layer speeds, and the uncertainty on the speed. This quantity is defined as follows:

$$\chi^2 = \Sigma_{layer} \frac{(v_{avg} - v_{layer})^2}{\sigma^2} \tag{5.2}$$

The $\chi^2$ divided by the number of degrees of freedom for each particle in the event is required to be less than four. This cut will remove particles whose times in the

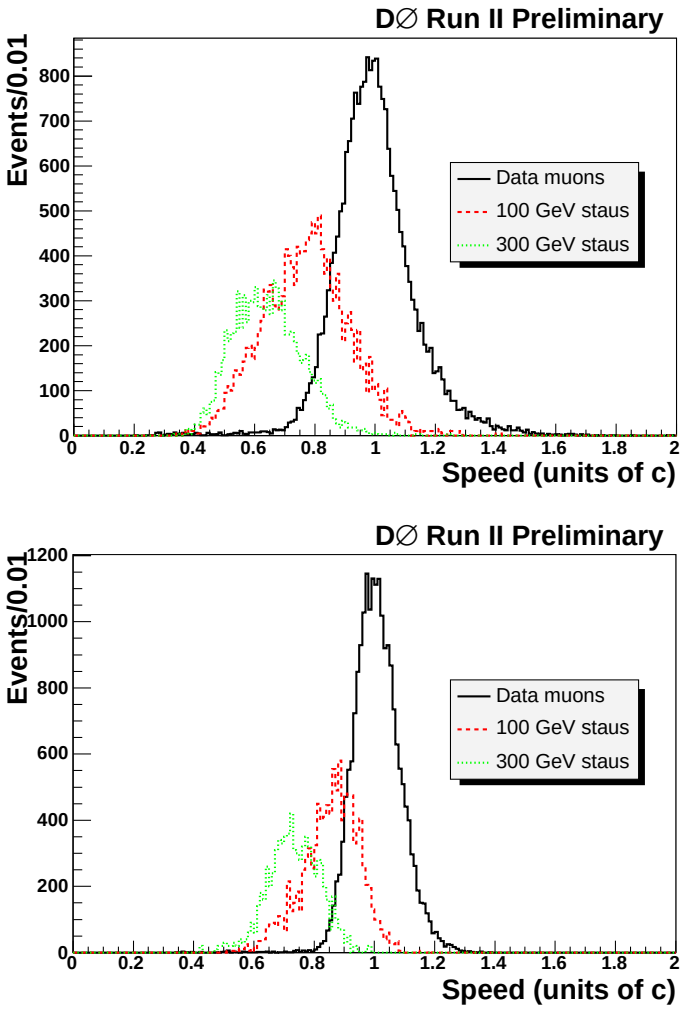


Figure 5.7: Calculated speed for real muons in data (black), 100 GeV/$c^2$ simulated staus (red), and 300 GeV/$c^2$ simulated staus (green). The top plot is for particles in the central muon region and the bottom plot is for particles in the forward muon region. All particles pass preselection cuts. Histograms are normalized to approximately the same number of events.

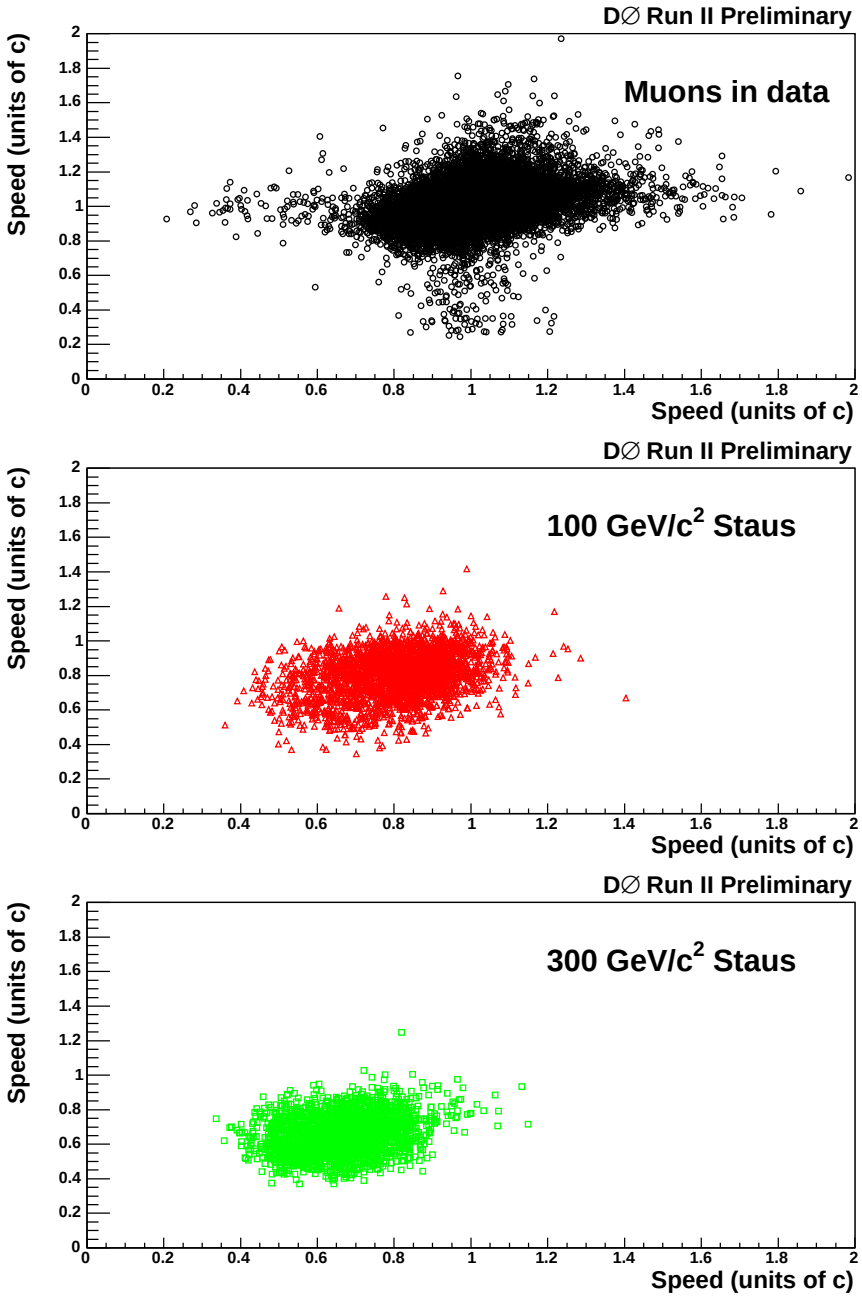


Figure 5.8: The two-dimensional distribution of the speed of each muon for muon pairs in data (top, black circles), 100 GeV/c$^2$ staus (middle, red triangles), and 300 GeV/c$^2$ staus (bottom, green squares). All particles pass preselection cuts. Histograms are normalized to approximately the same number of events.

muon system fall in the non-gaussian tail of the timing distribution, as well as particles that are not beam-produced muons (such as any remaining cosmic-ray muons or calorimeter punch-through particles). The efficiency for signal events to pass the $\chi^2$ requirement was estimated using muons in the Z peak (invariant mass 80 to 100 GeV/$c^2$). Table 5.7 shows the cumulative efficiency for the various preselection cuts.

Table 5.7: Cumulative trigger and preselection efficiencies for stau signal events. The "trigger" column shows the fraction of signal events passing the trigger requirements (including arriving within the trigger gate). The "medium" column requires both of the particles in the event to be identified as medium. The "scint hits" column requires both particles in the event to contain hits in at least two layers of the muon scintillators. The "track" column requires both of the muons to be matched to a central track. The "$p_T$" column requires both muons to have a transverse momentum larger than 15 GeV/c. The "$\Delta\phi$" column requires the difference in $\phi$-coordinate of the two particles be larger than 1.0 rad. The "cosmic" column required both particles in the event to pass the cosmic vetos. The "$\chi^2$" column shows the efficiency for both particles to pass the $\chi^2 > 4$ requirement.

| Stau Mass (GeV) | Trigger | Medium | Scint Hits | Track | $p_T$ | $\Delta\phi$ | Cosmic | $\chi^2$ |
|---|---|---|---|---|---|---|---|---|
| 60 | 0.67 | 0.58 | 0.29 | 0.25 | 0.25 | 0.25 | 0.23 | 0.18 |
| 100 | 0.68 | 0.62 | 0.29 | 0.27 | 0.27 | 0.27 | 0.24 | 0.19 |
| 150 | 0.68 | 0.62 | 0.29 | 0.26 | 0.26 | 0.26 | 0.23 | 0.18 |
| 200 | 0.65 | 0.60 | 0.27 | 0.25 | 0.25 | 0.25 | 0.21 | 0.17 |
| 250 | 0.61 | 0.57 | 0.26 | 0.24 | 0.24 | 0.24 | 0.20 | 0.16 |
| 300 | 0.57 | 0.53 | 0.24 | 0.22 | 0.22 | 0.22 | 0.18 | 0.14 |

# D. Analysis Cuts

The speed calculated from the scintillator timing information in the muon system is used to separate slow-moving CMSPs from speed-of-light muons. Even though a particle may have a measured speed that is substantially less than the speed of light, it is still possible that this speed is compatible with the speed of light within the uncertainty. So, rather than use the speed directly, we define the *speed significance* as in Equation 5.3.

$$speed\ significance = \frac{1 - speed}{\sigma_{speed}} \tag{5.3}$$

The speed significance is a measure of the number of standard deviations away from the speed of light. Since CMSPs will be moving slower than the speed of light, they are expected to have a speed significance that is larger than zero. Particles moving at the speed of light are expected to have a speed significance of zero (within the detector resolution). Figure 5.9 shows the speed significance for real muons in data, 100 GeV/c$^2$, and 300 GeV/c$^2$ staus. The speed significance of muons in data has a slight asymmetry, with a longer tail at positive speed significance. This is because the readout gates for the scintillator times are also asymmetric, accepting times up to approximately 60 ns before the beam-produced muon signal, where only approximately 20 ns before the beam-produced muon signal are accepted. Figure 5.10 shows the two-dimensional speed significance distributions for both of the particles in dimuon data events and for 100 GeV/c$^2$ staus.

In the actual analysis, the speed significance of the two particles is multiplied together to get the *significance product*. This variable gives quite good separa-

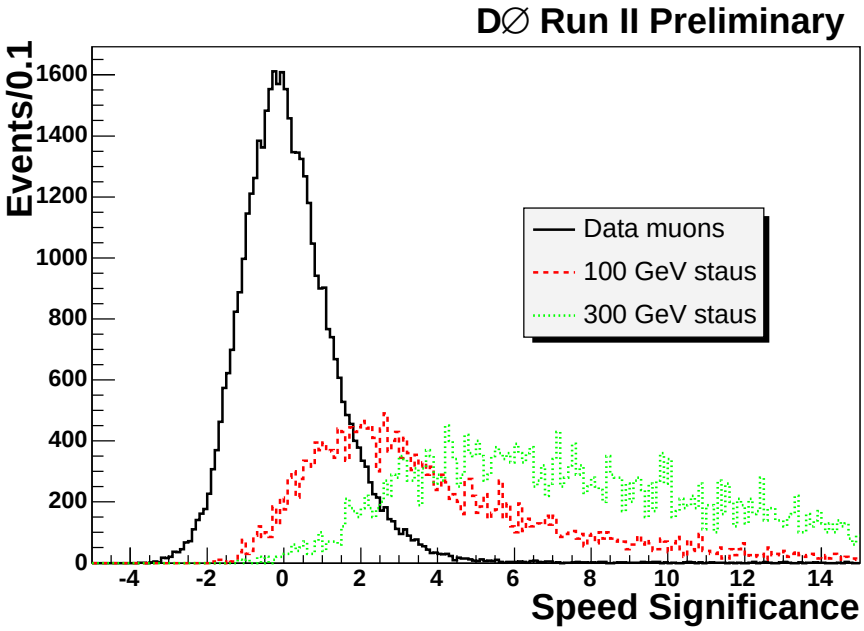


Figure 5.9: Speed significance for muons in data (black), 100 GeV/$c^2$ staus (red), and 300 GeV/$c^2$ staus (green). All particles pass preselection cuts. Histograms are normalized to approximately the same number of events.

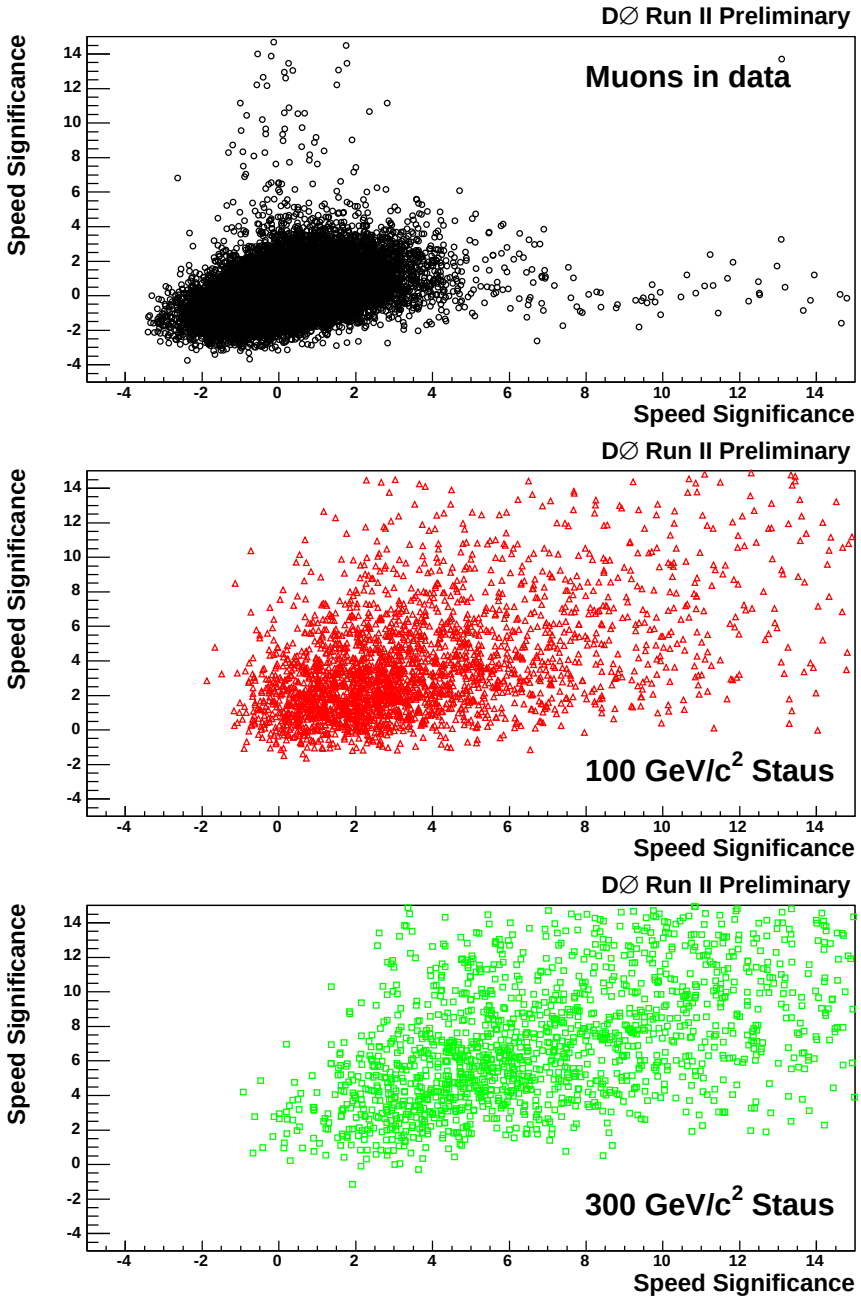


Figure 5.10: The two-dimensional distribution of the speed significance of each muon for dimuons in data (top, black circles), 100 GeV/c$^2$ staus (middle, red triangles), and 300 GeV/c$^2$ staus (bottom, green squares). All particles pass preselection cuts. Histograms are normalized to approximately the same number of events.

tion between signal and background. Figure 5.11 shows the significance product distribution for muon pairs in data and 100 GeV/$c^2$ staus.

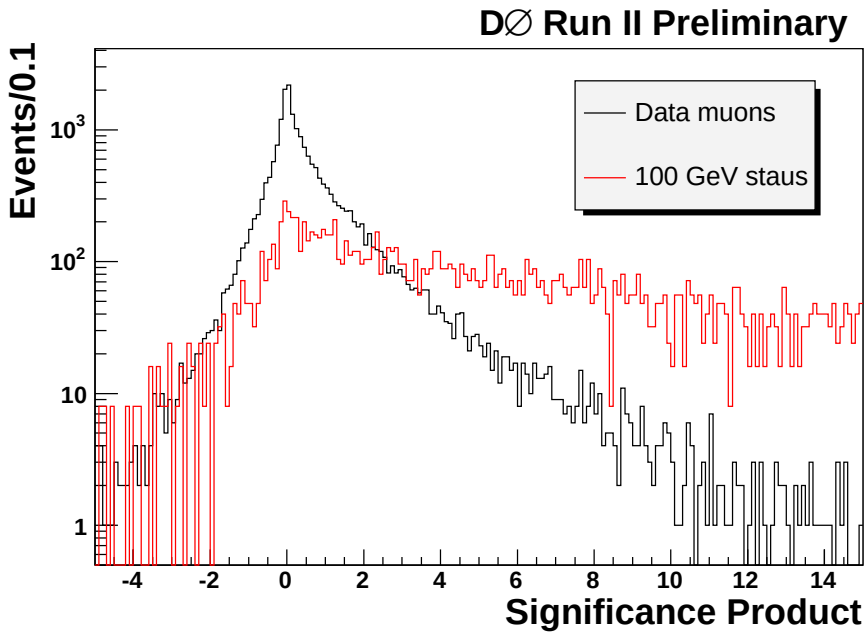


Figure 5.11: Significance product distribution for muon pairs in data (black) and 100 GeV/$c^2$ staus (red). All particles pass preselection requirements. Histograms are normalized to approximately the same number of events.

The first analysis cut requires the speed significance of both particles in the event to be larger than zero. This eliminates events that have the speed significance of both particles negative, which results in a significance product that is positive.

Another variable that is used to discriminate between signal and background events is the invariant mass of the two particles in the event. Background events are real muons, which are mostly from the decay of Z-bosons in the transverse momentum range of interest. However, signal events occur at a much larger invariant mass, as seen in Figure 5.12. To calculate the invariant mass of signal

events, the particles are assumed to have the mass of a muon and the three-momentum is taken from the central tracker measurement.

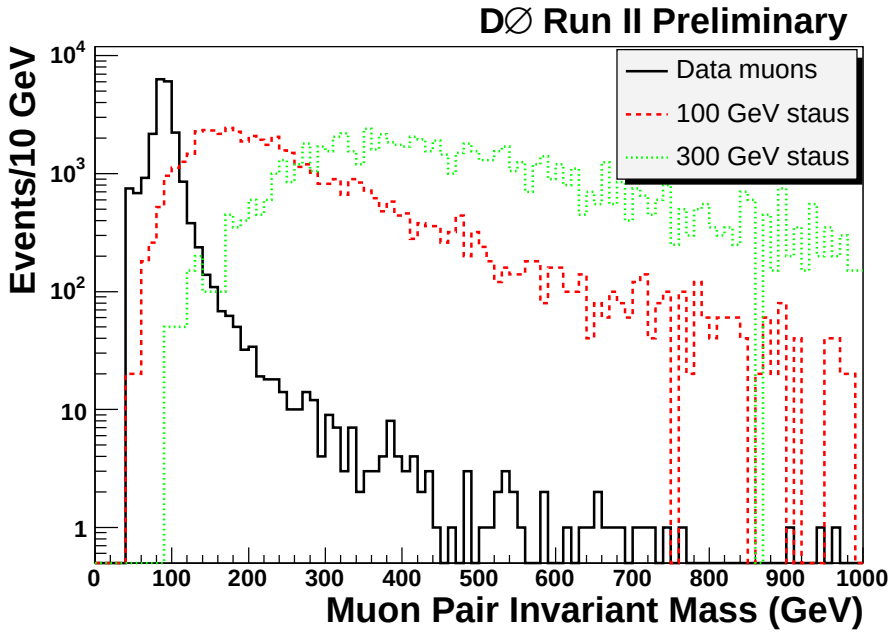


Figure 5.12: Invariant mass of muon pair for muons in real (black), 100 GeV/$c^2$ staus (red), and 300 GeV/$c^2$ staus (green). The muon mass is assumed when calculating the invariant mass of the stau pair. All particles pass preselection cuts. Histograms are normalized to approximately the same number of events.

In order to maximally utilize the available information in the event, a two-dimensional cut is made in the invariant mass versus significance product plane. The two-dimensional distribution for real muons in data and 60 GeV/$c^2$ staus is shown in Figure 5.13. First, an invariant mass cut is chosen that will be 90% efficient for signal events.[1] Next, a hyperbolic cut is implemented of the form

[1]For the 60 GeV/$c^2$ stau mass point, the 90% efficient stau invariant mass cut was below the Z-peak. So, the invariant mass cut for the 60 GeV/$c^2$ mass point was chosen to be at 110 GeV/$c^2$ to eliminate the Z-peak.

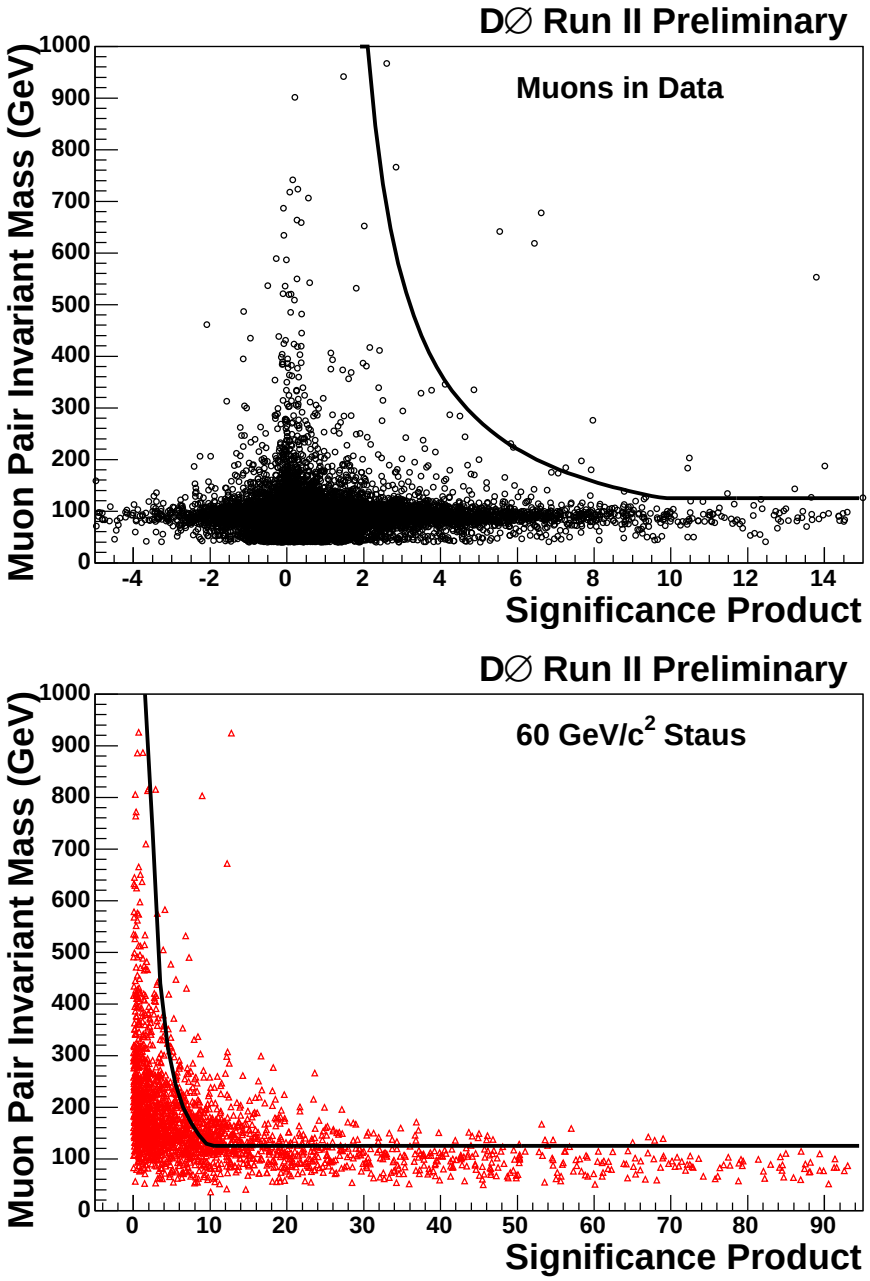


Figure 5.13: Invariant mass versus significance product for muon pairs in data (top, black circles) and 60 GeV/c$^2$ staus (bottom, red triangles). All particles pass preslection cuts. Histograms are normalized to approximately the same number of events. The optimized two-dimensional cut is shown as a black line. All events above the line are passed.

shown in Equation 5.4.

$$invmass\ cut = \frac{par0}{significance\ product - par1} \tag{5.4}$$

Where $par0$ and $par1$ are variables to be optimized. Based on the cross section for stau pair production, very few events are expected to be produced. Therefore, the parameters are optimized by minimizing the expected 95% confidence level cross section limit. Table 5.8 shows the optimized cut parameters for each stau mass point.

Table 5.8: Optimized Cut Parameters

| Stau Mass (GeV/c$^2$) | Invariant Mass Cut (GeV/c$^2$) | $par0$ | $par1$ |
|---|---|---|---|
| 60 | 110 | 1100 | 1 |
| 100 | 125 | 2000 | 6 |
| 150 | 165 | 2000 | 5 |
| 200 | 205 | 1800 | 5 |
| 250 | 245 | 2000 | 5 |
| 300 | 275 | 2000 | 4 |

It should be noted that since the invariant mass and significance of the signal events are correlated, the actual cuts used in this analysis are likely not ideal. A future version of the analysis could either use a more complicated multidimensional contour, or use an advanced analysis method (such as a neural network) to achieve better separation between signal and background.

# E. Background Estimation

There are no Standard Model processes that would appear as a massive, ionizing, slowly moving particle in the detector. The only background is real muons that for some reason have anomalously large times. So, the background estimates are derived from data events. The analysis cuts applied are the significance cut and the two-dimensional cut. For background events, no significant correlations exist between these quantities, since speed is measured in the muon system and the invariant mass is measured using the central tracker. The background efficiency for each cut is calculated separately, then the separate efficiencies are multiplied together to get the total efficiency for background events to pass all cuts.

The first cut applied was to require positive significance for both muons in the event. Events in the data sample are selected if they have a dimuon invariant mass between 80 and 100 GeV/$c^2$. There is expected to be less than one signal event in this region, while there are over ten thousand events in the data. The number of events in the Z peak (80 to 100 GeV/$c^2$) that have speed significance of both muons larger than zero is divided by the total number of events in the Z peak to give an estimate of the cut efficiency on background events.

Two distributions are used to predict the background remaining after the two-dimensional invariant mass versus significance product cut: the significance product distribution from events in the Z peak (Figure 5.14) and the invariant mass distribution for events in the signal sample that have the speed significance of both muons less than zero (Figure 5.15). These two distributions are then normalized and used to construct the two dimensional probability density function (PDF) for background events. The area of this two-dimensional PDF above

the cut curve is then integrated to obtain the efficiency of background events to pass the two-dimensional cut. Table 5.9 shows the efficiencies for the background events to pass the significance and two-dimensional cut.

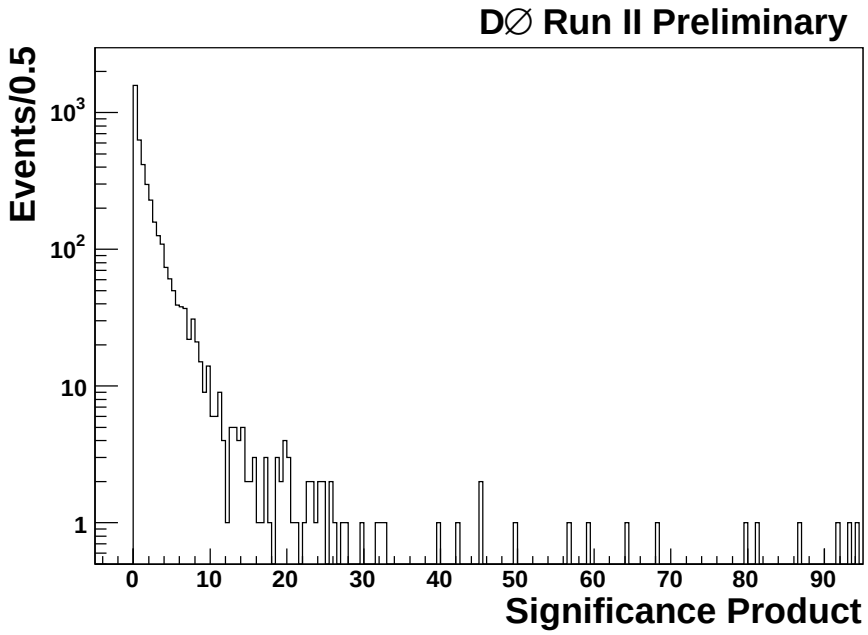


Figure 5.14: Significance product distribution used to estimate background. It contains the significance product of all events in the Z peak (80 - 100 GeV/$c^2$).

Table 5.9: Background event cut efficiency

| Mass Point (GeV/$c^2$) | Significance Efficiency | Two-dimensional Efficiency | Total Efficiency |
|---|---|---|---|
| 60 | 0.33 | 0.0022 | $7.3 \times 10^{-4}$ |
| 100 | 0.33 | 0.00011 | $3.6 \times 10^{-5}$ |
| 150 | 0.33 | 0.00011 | $3.6 \times 10^{-5}$ |
| 200 | 0.33 | 0.000096 | $3.2 \times 10^{-5}$ |
| 250 | 0.33 | 0.000075 | $2.5 \times 10^{-5}$ |
| 300 | 0.33 | 0.000097 | $3.2 \times 10^{-5}$ |

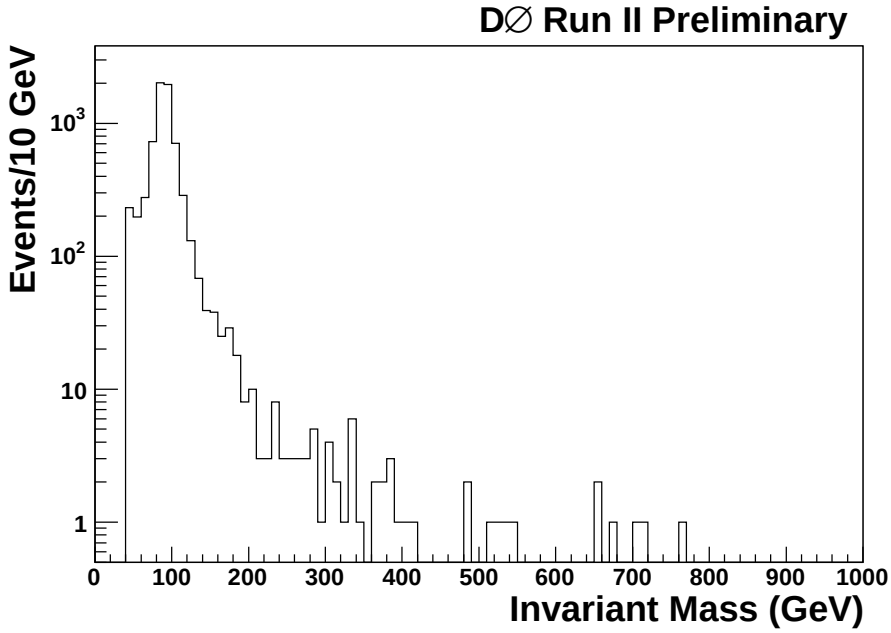


Figure 5.15: Invariant mass distribution used to estimate background. It contains the invariant mass of signal events where the speed significance of both muons is less than zero.

# F. Systematic Uncertainties

The PMCS simulation may not perfectly describe the response of the detector to CMSPs. For example, the tranverse momentum smearing, trigger efficiencies, and muon identification efficiencies may not be accurate. The $Z \rightarrow \mu\mu$ cross section analysis (for which the PMCS values were tuned) quotes a systematic uncertainty of 2% on the PMCS acceptance. Since the preselection cuts used in this analysis are nearly identical, we have also assumed a 2% systematic uncertainty arising from the PMCS calculation.

Muons in the Z peak (80 to 100 GeV/c$^2$) were used to estimate the efficiency of signal events to pass the $\chi^2$ requirement. The width of the Z peak used was varied to estimate the possible systematic uncertainty in this estimate. The efficiency estimate was found to vary by less than 1%.

It is also possible that the scintillation counter timing simulation is not completely accurate. The widths and means of the timing distributions used to smear the times computed in PMCS were calculated from all tight muons in the data sample. These times and means were compared to those obtained from a sample of muons from Z boson decays. The comparison is shown in Table 5.10. To estimate the systematic uncertainty introduced by an imperfect knowledge of the widths and means of the timing distributions, a new PMCS sample of ten-thousand 100 GeV/c$^2$ stau events was processed. The difference in the signal acceptance of the original PMCS sample and the PMCS sample processed with the Z muon widths and means was taken as an estimate of the systematic uncertainty on the PMCS timing simulation. The systematic uncertainties on the signal acceptances are shown in Table 5.11.

Table 5.10: Comparison of timing distribution widths and means between all tight muons and muons from Z boson decays.

| Scintillation Counter | Tight Muon Resolution (ns) | Tight Muon Offset (ns) | Z Muon Resolution (ns) | Z Muon Offset (ns) |
|---|---|---|---|---|
| Forward A-layer | 2.19 | -0.04 | 2.12 | 0.05 |
| Forward B-layer | 2.28 | -0.06 | 2.36 | -0.25 |
| Forward C-layer | 2.38 | 0.02 | 2.35 | -0.11 |
| Central A-layer | 2.30 | -0.06 | 2.13 | -0.06 |
| Central side B-layer | 2.37 | -0.41 | 2.35 | 0.04 |
| Central bottom B-layer | 3.41 | -0.22 | 3.06 | 1.05 |
| Central side/top C-layer | 3.41 | -0.11 | 3.19 | -0.26 |
| Central bottom C-layer | 3.32 | 0.23 | 1.81 | 0.25 |

Table 5.11: Summary of systematic uncertainties on the signal acceptance.

| Source | Fractional Uncertainty |
|---|---|
| PMCS efficiencies | 0.02 |
| $\chi^2$ efficiency | 0.008 |
| PMCS timing | 0.019 |
| Total systematic uncertainty on acceptance | 0.027 |

For the background estimate, two distributions were used to estimate the background remaining after the two-dimensional invariant mass versus significance product cut: the significance product distribution from muons in the Z peak (80 - 100 GeV/$c^2$) and the invariant mass distribution from events where muons have a speed significance less than zero. The width of the Z peak used to select the significance product distribution was varied. Separately, the value of the significance requirements on the two muons used in the invariant mass distribution was also varied. The largest effect on the background efficiency from these variations was found to be 3.5%. Table 5.12 summarizes the sources of systematic uncertainty on the background estimate.

Table 5.12: Summary of systematic uncertainties on the background estimate.

| Source | Fractional Uncertainty |
|---|---|
| Significance $< 0$ cut | 0.007 |
| Invariant mass vs. significance product cut | 0.035 |
| Total systematic uncertainty on background estimate | 0.036 |

# G. Results

The events remaining after the various cuts are shown in Table 5.13 for all stau mass points. Table 5.14 shows the final number of events remaining in the data after all cuts, the signal acceptance, and the predicted number of background events for all six stau mass points.

Table 5.13: Events remaining and signal acceptance after cuts.

| Cut | Data Events | Predicted background | Signal Acceptance |
|---|---|---|---|
| **60 GeV/c$^2$ Staus** | | | |
| Preselection | 18,985 | | 0.18 |
| Significance $> 0$ | 6410 | $6279 \pm 127$(stat) $\pm$ 44(sys) | 0.16 |
| Two-dimensional cut | 13 | $13.6 \pm 0.7 \pm 0.5$ | 0.04 |
| **100 GeV/c$^2$ Staus** | | | |
| Preselection | 18,985 | | 0.19 |
| Significance $> 0$ | 6410 | $6279 \pm 127$(stat) $\pm$ 44(sys) | 0.17 |
| Two-dimensional cut | 0 | $0.66 \pm 0.06 \pm 0.02$ | 0.06 |
| **150 GeV/c$^2$ Staus** | | | |
| Preselection | 18,985 | | 0.18 |
| Significance $> 0$ | 6410 | $6279 \pm 127$(stat) $\pm$ 44(sys) | 0.17 |
| Two-dimensional cut | 0 | $0.69 \pm 0.05 \pm 0.02$ | 0.10 |
| **200 GeV/c$^2$ Staus** | | | |
| Preselection | 18,985 | | 0.17 |
| Significance $> 0$ | 6410 | $6279 \pm 127$(stat) $\pm$ 44(sys) | 0.17 |
| Two-dimensional cut | 0 | $0.60 \pm 0.04 \pm 0.02$ | 0.12 |
| **250 GeV/c$^2$ Staus** | | | |
| Preselection | 18,985 | | 0.16 |
| Significance $> 0$ | 6410 | $6279 \pm 127$(stat) $\pm$ 44(sys) | 0.16 |
| Two-dimensional cut | 0 | $0.47 \pm 0.03 \pm 0.02$ | 0.12 |
| **300 GeV/c$^2$ Staus** | | | |
| Preselection | 18,985 | | 0.14 |
| Significance $> 0$ | 6410 | $6279 \pm 127$(stat) $\pm$ 44(sys) | 0.14 |
| Two-dimensional cut | 0 | $0.61 \pm 0.05 \pm 0.02$ | 0.12 |

Table 5.14: Analysis results for all six stau mass points.

| Stau Mass (GeV/$c^2$) | Data Events | Background Prediction | Signal Acceptance |
|---|---|---|---|
| 60 | 13 | 13.6 ± 0.7 (stat) ± 0.5 (syst) | 0.0381 ± 0.0007 (stat) ± 0.0010 (syst) |
| 100 | 0 | 0.66 ± 0.06 ± 0.02 | 0.0559 ± 0.0009 ± 0.0015 |
| 150 | 0 | 0.69 ± 0.05 ± 0.02 | 0.0968 ± 0.0014 ± 0.0026 |
| 200 | 0 | 0.60 ± 0.04 ± 0.02 | 0.1180 ± 0.0016 ± 0.0032 |
| 250 | 0 | 0.47 ± 0.03 ± 0.02 | 0.1222 ± 0.0017 ± 0.0033 |
| 300 | 0 | 0.61 ± 0.05 ± 0.02 | 0.1226 ± 0.0017 ± 0.0033 |

Since the number of observed events is consistent with the expected background, a 95% confidence level limit on the production cross section is set using the $CL_s$ method for each stau mass point [37]. These can be compared to the next-to-leading order cross section calculated with SoftSusy and Prospino 2 [38, 39]. The calculated limits and the NLO cross section for each mass point are shown in Table 5.15 and graphically in Figure 5.16. Although these preliminary limits are not yet stringent enough to set a limit on the stau mass, they are the best limits to date from the Tevatron.

Table 5.15: Limits and NLO cross section for pair-produced staus.

| Stau Mass (GeV/c$^2$) | 95% CL limit (pb) | NLO cross section (pb) |
|---|---|---|
| 60 | 0.620 | 0.072 |
| 100 | 0.139 | 0.012 |
| 150 | 0.081 | 0.0022 |
| 200 | 0.066 | 0.00049 |
| 250 | 0.064 | 0.00012 |
| 300 | 0.064 | 0.000032 |

Table 5.16 shows some information about the events that pass all cuts for the 60 GeV/c$^2$ mass point. No events pass all cuts for the other mass points. Several of the events that pass all cuts probably have the momentum of one of the muons mismeasured.

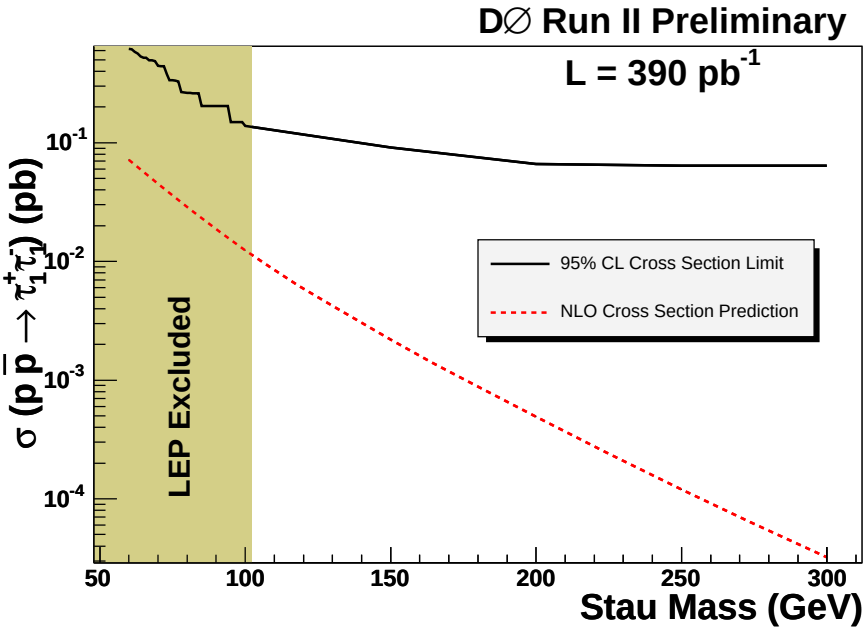


Figure 5.16: 95% CL cross-section limit (solid line) and NLO production cross section (dashed line) versus stau mass for pair-produced staus.

Table 5.16: Events passing all cuts for the 60 GeV mass point.

| Run Number | Invariant Mass (GeV) | Muon 1 $p_T$ GeV | Muon 2 $p_T$ (GeV) | Muon 1 Significance | Muon 2 Significance |
|---|---|---|---|---|---|
| 164450 | 276 | 288 | 64 | 2.3 | 3.4 |
| 179194 | 182 | 214 | 39 | 3.0 | 3.6 |
| 175642 | 618 | 1796 | 51 | 2.4 | 2.7 |
| 187864 | 145 | 27 | 83 | 5.6 | 2.4 |
| 188933 | 112 | 52 | 59 | 6.9 | 3.9 |
| 189562 | 133 | 38 | 117 | 3.3 | 3.4 |
| 190082 | 199 | 148 | 52 | 3.9 | 1.9 |
| 190368 | 3870 | 37 | 99864 | 1.2 | 2.1 |
| 191884 | 134 | 36 | 120 | 3.6 | 5.4 |
| 192364 | 647 | 19 | 1106 | 2.2 | 2.5 |
| 192581 | 962 | 56 | 4088 | 1.7 | 1.5 |
| 192823 | 122 | 51 | 66 | 4.8 | 2.6 |
| 193708 | 236 | 33 | 415 | 22 | 2.6 |

# CHAPTER 6

# THE CHARGINO ANALYSIS

The preceding chapter described a search for stable staus in a GMSB model using the scintillator timing to measure the speed of particles passing through the muon system of the DØ detector. This chapter describes an extension of that analysis. The strategy and cuts involved are identical, but the result is interpreted in terms of a stable chargino SUSY scenario. These are preliminary results that have not yet been published, but have received approval to be shown outside the DØ collaboration [31].

## A. Signal Sample

Two different model points are used. The relevant SUSY parameters are the higgsino mass parameter, $\mu$, the ratio of Higgs vacuum expectation values, $\tan\beta$, and the gaugino mass parameters, $M_1$ and $M_2$. The two different models studied are a higgsino-like chargino and a gaugino-like chargino. The higgsino-like chargino case has small $|\mu|$ and large $M_1$ and $M_2$. The lightest chargino and the lightest neutralino are both higgsino-like and have a mass approximately equal to $|\mu|$. In the gaugino-like chargino case, $|\mu|$ is large and the lightest neutralino and the lightest chargino are gaugino-like and have a mass approximately equal to $M_2$ (assuming $M_1 > M_2$).

Pythia and PMCS were used to generate 100,000 events for each of six mass points (60, 100, 150, 200, 250, and 300 GeV/c$^2$, chosen to be identical to those used in the stau analysis) for each of the two models. Pair-production of the lightest chargino was used. The parameters used for each of the chargino models are shown in Table 6.1. The value of $\tan\beta$ was fixed at 15 for all models and mass points. For the gaugino-like chargino model the value of $M_1$ was chosen to be three times $M_2$, motivated by AMSB models.

Table 6.1: SUSY parameters used in chargino analysis

| Model | $\mu$ (GeV/c$^2$) | $M_1$ (GeV/c$^2$) | $M_2$ (GeV/c$^2$) | $M_3$ (GeV/c$^2$) | $\tan\beta$ | Squark Mass (GeV) |
|---|---|---|---|---|---|---|
| higgsino-like chargino | varied from 60 to 300 | 100,000 | 100,000 | 500 | 15 | 800 |
| gaugino-like chargino | 10,000 | $3M_2$ | varied from 60 to 300 | 500 | 15 | 800 |

## B. Data Sample

The data sample used for the chargino analysis is identical to the data sample used in the stau analysis.

## C. Preselection and Analysis Cuts

The kinematic properties of the chargino models are similar to those of staus of the same mass, as seen in a comparison of stau and charginos in the momentum distribution and speed distribution, shown in Figures 6.1 and 6.2. The charginos have a softer transverse momentum distribution than staus, but they are also more likely to be produced more forward than staus, so the speed distributions for charginos and staus are quite similar. Therefore, the cuts used in the chargino analysis are identical to those used for the stau analysis. The preselection efficiencies for charginos are shown in Table 6.2 (for higgsino-like charginos) and 6.3 (for gaugino-like charginos). The columns are identical to those in Table 5.7. PMCS is used to calculate the acceptance for each of the chargino models and its associated statistical uncertainty. The signal acceptance for the two chargino models is shown in Table 6.4. Figure 6.3 shows a comparison of signal acceptances for staus and the two chargino models used in this analysis. The drop in chargino acceptance for large masses is due to the slightly softer momentum spectrum of charginos compared to staus. This causes the charginos to move slightly slower and reduces the number of particles arriving within the trigger gate. The two-dimensional analysis cuts become more efficient for particles moving more slowly.

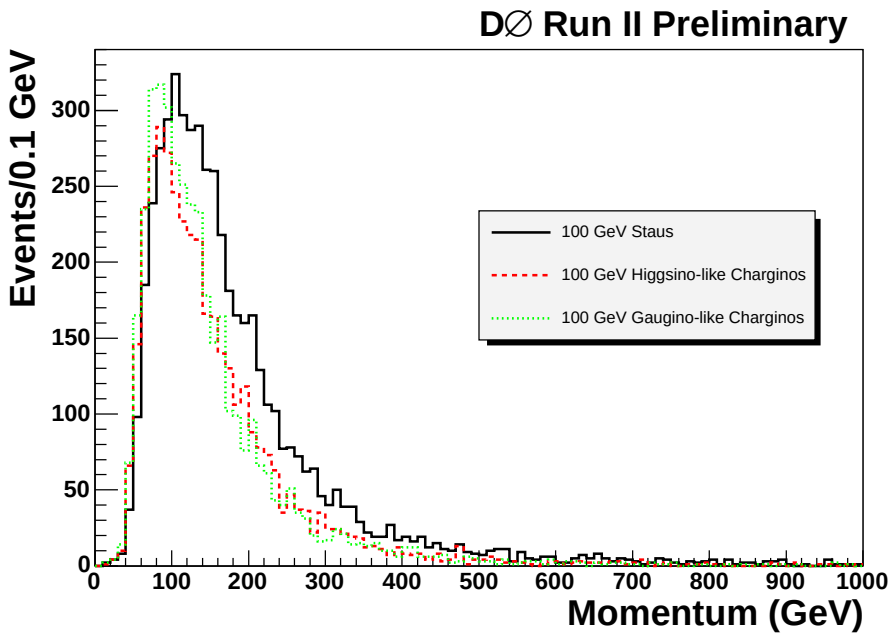


Figure 6.1: Momentum distribution for staus (black), higgsino-like charginos (red), and gaugino-like charginos (green). Both the staus and charginos have a mass of 100 GeV/$c^2$. All particles pass preselection cuts. Histograms are normalized to approximately the same number of events.

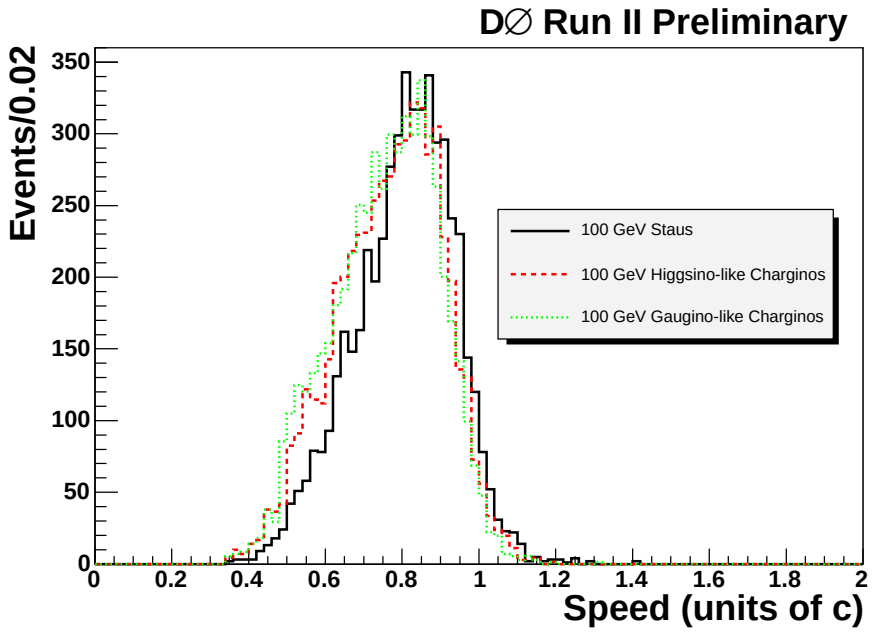


Figure 6.2: Speed distribution for staus (black), higgsino-like charginos (red), and gaugino-like charginos (green). Both the staus and charginos have a mass of 100 GeV/$c^2$. All particles pass preselection cuts. Histograms are normalized to the same number of events.

Table 6.2: Cumulative trigger and preselection efficiencies for higgsino-like chargino signal events.

| Chargino Mass (GeV/c$^2$) | Trigger | Medium | Scint Hits | Track | $p_T$ | $\Delta\phi$ | Cosmic | $\chi^2$ |
|---|---|---|---|---|---|---|---|---|
| 60 | 0.49 | 0.39 | 0.21 | 0.18 | 0.18 | 0.18 | 0.16 | 0.12 |
| 100 | 0.54 | 0.46 | 0.24 | 0.20 | 0.20 | 0.20 | 0.18 | 0.14 |
| 150 | 0.52 | 0.46 | 0.24 | 0.21 | 0.21 | 0.21 | 0.17 | 0.13 |
| 200 | 0.49 | 0.44 | 0.22 | 0.20 | 0.20 | 0.20 | 0.16 | 0.13 |
| 250 | 0.44 | 0.40 | 0.20 | 0.18 | 0.18 | 0.18 | 0.14 | 0.11 |
| 300 | 0.38 | 0.35 | 0.17 | 0.16 | 0.16 | 0.16 | 0.12 | 0.09 |

Table 6.3: Cumulative trigger and preselection efficiencies for gaugino-like chargino signal events.

| Chargino Mass (GeV/c$^2$) | Trigger | Medium | Scint Hits | Track | $p_T$ | $\Delta\phi$ | Cosmic | $\chi^2$ |
|---|---|---|---|---|---|---|---|---|
| 60 | 0.49 | 0.39 | 0.21 | 0.18 | 0.18 | 0.18 | 0.16 | 0.12 |
| 100 | 0.54 | 0.46 | 0.24 | 0.20 | 0.20 | 0.20 | 0.18 | 0.14 |
| 150 | 0.52 | 0.46 | 0.24 | 0.21 | 0.21 | 0.21 | 0.17 | 0.13 |
| 200 | 0.49 | 0.44 | 0.22 | 0.20 | 0.20 | 0.20 | 0.16 | 0.12 |
| 250 | 0.44 | 0.40 | 0.20 | 0.18 | 0.18 | 0.18 | 0.14 | 0.10 |
| 300 | 0.38 | 0.35 | 0.17 | 0.16 | 0.16 | 0.16 | 0.12 | 0.09 |

Table 6.4: Signal acceptance for the two chargino models.

| Mass (GeV/$c^2$) | Higgsino-like Signal Acceptance | Gaugino-like Signal Acceptance |
|---|---|---|
| 60 | 0.0249 ± 0.0006 (stat) ± 0.0007 (syst) | 0.0227 ± 0.0005 (stat) ± 0.0006 (syst) |
| 100 | 0.0519 ± 0.0009 ± 0.0014 | 0.0536 ± 0.0009 ± 0.0015 |
| 150 | 0.0815 ± 0.0012 ± 0.0022 | 0.0805 ± 0.0012 ± 0.0022 |
| 200 | 0.0921 ± 0.0013 ± 0.0025 | 0.0880 ± 0.0013 ± 0.0024 |
| 250 | 0.0872 ± 0.0013 ± 0.0024 | 0.0814 ± 0.0012 ± 0.0022 |
| 300 | 0.0783 ± 0.0012 ± 0.0021 | 0.0733 ± 0.0011 ± 0.0020 |

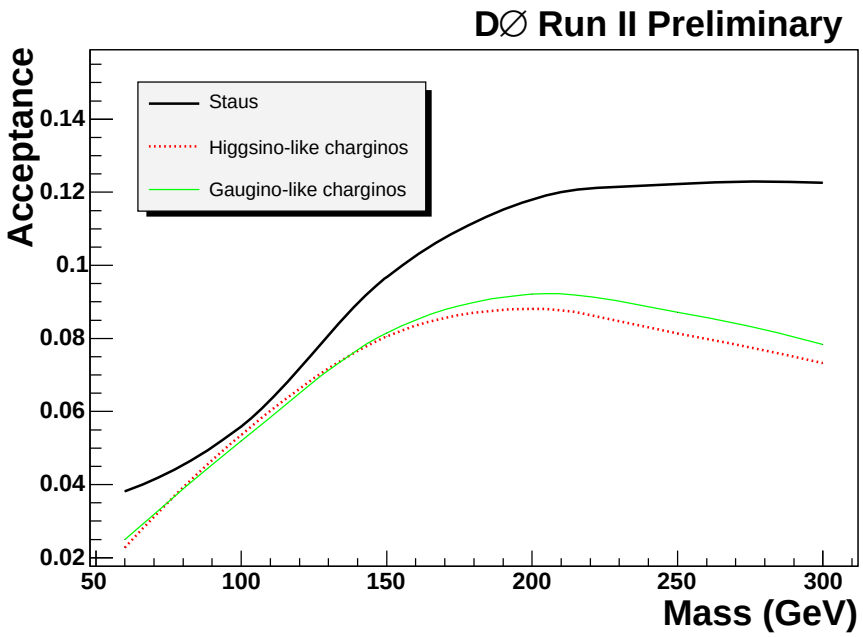


Figure 6.3: Signal acceptance after all cuts for staus (black), higgsino-like charginos (red), and gaugino-like charginos (green).

## D. Background Estimation

Since the cuts used for the chargino mass points were identical to those used for the stau mass points, the estimation of background events is identical to the estimation presented for the stau analysis.

## E. Systematic Uncertainties

The systematic uncertainties in the chargino analysis are identical to those estimated for the stau analysis.

# F. Results

Tables 6.5 and 6.7 show the events remaining and the signal acceptance at each stage of the analysis cuts for higgsino-like and gaugino-like charginos, respectively. Tables 6.6 and 6.8 show the number of data events, predicted number of background events, and the signal acceptance after all analysis cuts for higgsino-like and gaugino-like charginos, respectively.

Table 6.5: Events remaining and signal acceptance after cuts for higgsino-like charginos.

| Cut | Data Events | Predicted background | Signal Acceptance |
|---|---|---|---|
| **60 GeV/c$^2$ Charginos** | | | |
| Preselection | 18,985 | | 0.15 |
| Significance $> 0$ | 6410 | $6279 \pm 127$(stat) $\pm$ 44(sys) | 0.14 |
| Two-dimensional cut | 13 | $13.6 \pm 0.7 \pm 0.5$ | 0.02 |
| **100 GeV/c$^2$ Charginos** | | | |
| Preselection | 18,985 | | 0.17 |
| Significance $> 0$ | 6410 | $6279 \pm 127$(stat) $\pm$ 44(sys) | 0.16 |
| Two-dimensional cut | 0 | $0.66 \pm 0.06 \pm 0.02$ | 0.05 |
| **150 GeV/c$^2$ Charginos** | | | |
| Preselection | 18,985 | | 0.16 |
| Significance $> 0$ | 6410 | $6279 \pm 127$(stat) $\pm$ 44(sys) | 0.16 |
| Two-dimensional cut | 0 | $0.69 \pm 0.05 \pm 0.02$ | 0.08 |
| **200 GeV/c$^2$ Charginos** | | | |
| Preselection | 18,985 | | 0.15 |
| Significance $> 0$ | 6410 | $6279 \pm 127$(stat) $\pm$ 44(sys) | 0.15 |
| Two-dimensional cut | 0 | $0.60 \pm 0.04 \pm 0.02$ | 0.09 |
| **250 GeV/c$^2$ Charginos** | | | |
| Preselection | 18,985 | | 0.13 |
| Significance $> 0$ | 6410 | $6279 \pm 127$(stat) $\pm$ 44(sys) | 0.13 |
| Two-dimensional cut | 0 | $0.47 \pm 0.03 \pm 0.02$ | 0.09 |
| **300 GeV/c$^2$ Charginos** | | | |
| Preselection | 18,985 | | 0.11 |
| Significance $> 0$ | 6410 | $6279 \pm 127$(stat) $\pm$ 44(sys) | 0.11 |
| Two-dimensional cut | 0 | $0.61 \pm 0.05 \pm 0.02$ | 0.08 |

Table 6.6: Analysis results for all six higgsino-like chargino mass points.

| Chargino Mass (GeV/$c^2$) | Data Events | Background Prediction | Signal Acceptance |
|---|---|---|---|
| 60 | 13 | 13.6 ± 0.7 (stat) ± 0.5 (syst) | 0.0249 ± 0.0006 (stat) ± 0.0007 (syst) |
| 100 | 0 | 0.66 ± 0.06 ± 0.02 | 0.0519 ± 0.0009 ± 0.0014 |
| 150 | 0 | 0.69 ± 0.05 ± 0.02 | 0.0815 ± 0.0012 ± 0.0022 |
| 200 | 0 | 0.60 ± 0.04 ± 0.02 | 0.0921 ± 0.0013 ± 0.0025 |
| 250 | 0 | 0.47 ± 0.03 ± 0.02 | 0.0872 ± 0.0013 ± 0.0024 |
| 300 | 0 | 0.61 ± 0.05 ± 0.02 | 0.0783 ± 0.0012 ± 0.0021 |

Table 6.7: Events remaining and signal acceptance after cuts for gaugino-like charginos.

| Cut | Data Events | Predicted background | Signal Acceptance |
|---|---|---|---|
| **60 GeV/c$^2$ Charginos** | | | |
| Preselection | 18,985 | | 0.14 |
| Significance $> 0$ | 6410 | 6279 $\pm$ 127(stat) $\pm$ 44(sys) | 0.13 |
| Two-dimensional cut | 13 | 13.6 $\pm$ 0.7 $\pm$ 0.5 | 0.02 |
| **100 GeV/c$^2$ Charginos** | | | |
| Preselection | 18,985 | | 0.17 |
| Significance $> 0$ | 6410 | 6279 $\pm$ 127(stat) $\pm$ 44(sys) | 0.16 |
| Two-dimensional cut | 0 | 0.66 $\pm$ 0.06 $\pm$ 0.02 | 0.05 |
| **150 GeV/c$^2$ Charginos** | | | |
| Preselection | 18,985 | | 0.16 |
| Significance $> 0$ | 6410 | 6279 $\pm$ 127(stat) $\pm$ 44(sys) | 0.16 |
| Two-dimensional cut | 0 | 0.69 $\pm$ 0.05 $\pm$ 0.02 | 0.08 |
| **200 GeV/c$^2$ Charginos** | | | |
| Preselection | 18,985 | | 0.14 |
| Significance $> 0$ | 6410 | 6279 $\pm$ 127(stat) $\pm$ 44(sys) | 0.14 |
| Two-dimensional cut | 0 | 0.60 $\pm$ 0.04 $\pm$ 0.02 | 0.09 |
| **250 GeV/c$^2$ Charginos** | | | |
| Preselection | 18,985 | | 0.13 |
| Significance $> 0$ | 6410 | 6279 $\pm$ 127(stat) $\pm$ 44(sys) | 0.13 |
| Two-dimensional cut | 0 | 0.47 $\pm$ 0.03 $\pm$ 0.02 | 0.08 |
| **300 GeV/c$^2$ Charginos** | | | |
| Preselection | 18,985 | | 0.10 |
| Significance $> 0$ | 6410 | 6279 $\pm$ 127(stat) $\pm$ 44(sys) | 0.10 |
| Two-dimensional cut | 0 | 0.61 $\pm$ 0.05 $\pm$ 0.02 | 0.07 |

Table 6.8: Analysis results for all six gaugino-like chargino mass points.

| Chargino Mass (GeV/c$^2$) | Data Events | Background Prediction | Signal Acceptance |
|---|---|---|---|
| 60 | 13 | 13.6 ± 0.7 (stat) ± 0.5 (syst) | 0.0227 ± 0.0005 (stat) ± 0.0006 (syst) |
| 100 | 0 | 0.66 ± 0.06 ± 0.02 | 0.0536 ± 0.0009 ± 0.0015 |
| 150 | 0 | 0.69 ± 0.05 ± 0.02 | 0.0805 ± 0.0012 ± 0.0022 |
| 200 | 0 | 0.60 ± 0.04 ± 0.02 | 0.0880 ± 0.0013 ± 0.0024 |
| 250 | 0 | 0.47 ± 0.03 ± 0.02 | 0.0814 ± 0.0012 ± 0.0022 |
| 300 | 0 | 0.61 ± 0.05 ± 0.02 | 0.0733 ± 0.0011 ± 0.0020 |

Since no excess of events over the predicted background is observed, a 95% confidence level cross-section limit on the pair production cross section was set for both chargino models. This is compared to the predicted next-to-leading order cross section [40]. The limits obtained and the NLO cross section is shown for both of the chargino models in Table 6.9. This is shown graphically in Figure 6.4 for the higgsino-like chargino case and in Figure 6.5 for the gaugino-like chargino case. A mass limit for stable charginos is set by observing the point of intersection between the cross section limit and the NLO cross section prediction. This results in a mass limit of 140 GeV/$c^2$ for the higgsino-like chargino model and a mass limit of 174 GeV/$c^2$ for the gaugino-like chargino model. These are currently the best experimental limits to date for stable charginos.

Table 6.9: Limits and NLO cross section for pair-produced charginos.

| Chargino Mass (GeV) | Higgsino-like 95% CL limit (pb) | Higgsino-like NLO cross section (pb) | Gaugino-like 95% CL limit (pb) | Gaugino-like NLO cross section (pb) |
|---|---|---|---|---|
| 60 | 0.947 | 3.11 | 1.039 | 13.39 |
| 100 | 0.150 | 0.413 | 0.145 | 1.322 |
| 150 | 0.096 | 0.0796 | 0.097 | 0.211 |
| 200 | 0.085 | 0.0202 | 0.089 | 0.0452 |
| 250 | 0.089 | 0.0057 | 0.096 | 0.0106 |
| 300 | 0.100 | 0.0017 | 0.106 | 0.0026 |

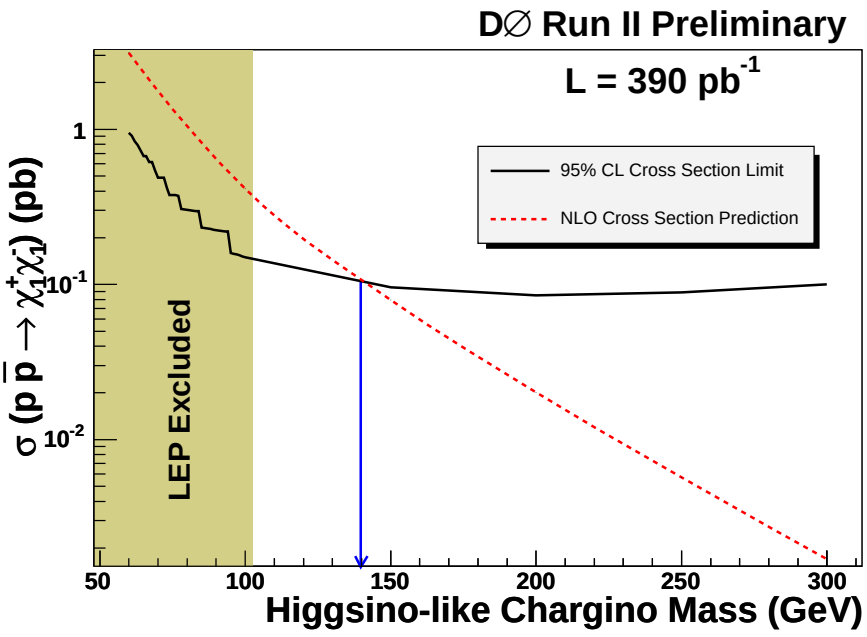


Figure 6.4: 95% CL cross section for higgsino-like charginos (black) and the NLO cross section prediction (red). Stable charginos with a mass less than 140 GeV/$c^2$ are excluded.

## G. Effect of a Finite Lifetime

The stau analysis and both models in the chargino analysis assumed that the CMSPs were absolutely stable. If the CMSP was to decay inside the detector it would reduce the acceptance and hence the sensitivity of this analysis. The effect of a finite lifetime CMSP was estimated by assuming the lifetime, then demanding that both of the CMSPs not decay until passing the detector's C-layer muon scintillation counters. Figure 6.6 shows the acceptance versus lifetime for 100 GeV/$c^2$ staus, higgsino-like charginos, and gaugino-like charginos.

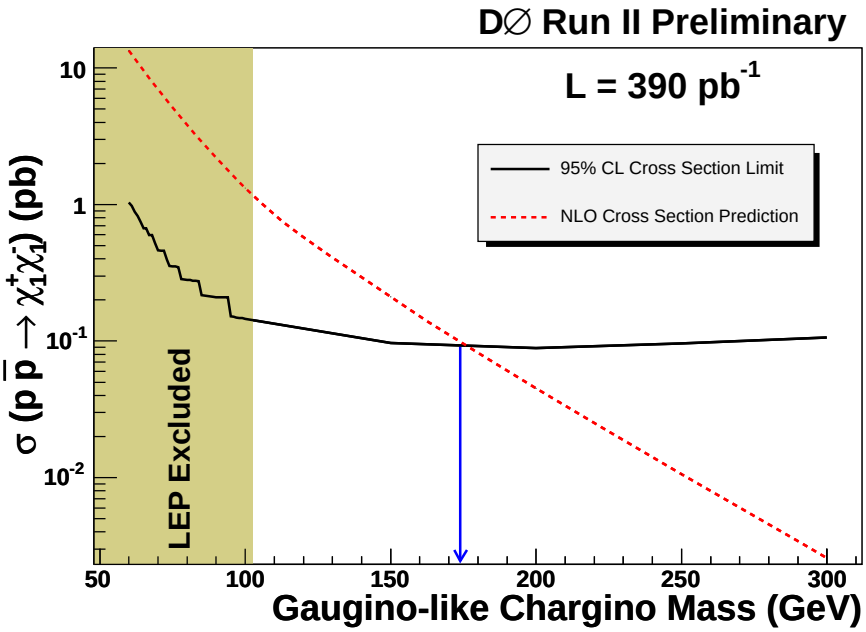


Figure 6.5: 95% CL cross section for gaugino-like charginos (black) and the NLO cross section prediction (red). Stable charginos with a mass less than 174 GeV/$c^2$ are excluded.

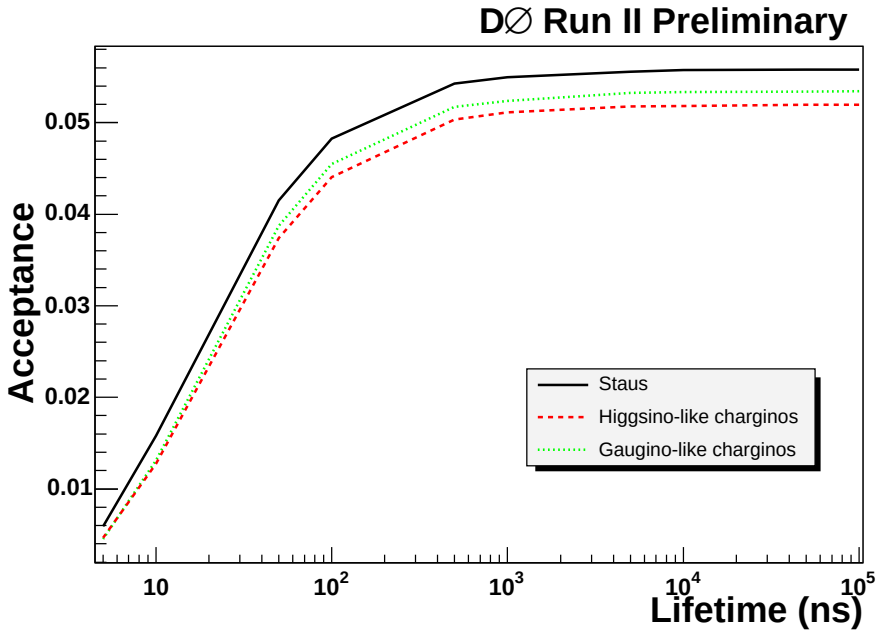


Figure 6.6: Acceptance versus lifetime for staus (black), higgsino-like charginos (red), and gaugino-like charginos (green). All have a mass of 100 GeV/$c^2$.

# CHAPTER 7

# CONCLUSION

A search for charged massive stable particles has been performed at the DØ detector at the Fermilab Tevatron using 390 $pb^{-1}$ of data. The timing information in the muon scintillation counters is used to calculate the speed of the muons in the event. No excess of events is observed over the background prediction, and 95% CL limits on the production cross for pair-produced stable stau leptons are set. These limits vary from 0.06 pb to 0.62 pb, depending on the stau mass, and are the most stringent limits to date from the Tevatron. Mass limits are also set for the pair-production of stable charginos. A higgsino-like chargino must be heavier than 140 $GeV/c^2$ and a gaugino-like chargino must be heavier than 174 $GeV/c^2$, both at the 95% confidence level. These are currently the best limits to date on stable charginos.

This analysis could be easily extended to search for CMSP signals in other models, such as heavy fourth generation leptons or a stable doubly-charged Higgs boson. Furthermore, other supersymmetric models could be explored. One could also explore inclusive CMSP production in supersymmetric models by utilizing cascade decays to CMSPs rather than only pair production. Although including cascade decays will result in a more complicated and model dependent signature, there will be a larger production cross section. In principle, as long as the particular CMSP signal events can be generated with a Monte Carlo program, it can

be interfaced into the PMCS detector simulation to obtain the signal efficiency.

In addition to a simple extension of the existing analysis to new model points, it is also possible to make some additional improvements to the next iteration of the analysis. In the existing version of the analysis, the speed significance product and the invariant mass of the event were used to separate candidate signal events from the muon background. It would be useful to be able to identify a CMSP on a particle-by-particle basis rather than an event-by-event basis.[1] The momentum and speed of a CMSP traversing the detector are related. Figure 7.1 shows the momentum versus speed for muons, 100 GeV/$c^2$, and 300 GeV/$c^2$ staus. Figure 7.2 shows the momentum versus speed significance for muons, 100 GeV/$c^2$, and 300 GeV/$c^2$ staus. There appears to be significant separation between signal and background.

Another possible improvement would be the use of energy loss in the detector to separate signal CMSPs from background muons. The energy loss could be measured in either the central tracker or the calorimeter (or both). However, much work needs to be done to verify the usefulness of such an approach. The energy loss of muons in the DØ detector has not been well studied, so it is not clear how much additional rejection would be obtained by using energy loss.

Another clear improvement for a future version of this analysis is a change in the choice of trigger requirement. It has been shown that a dimuon trigger begins to become a limiting factor in the efficiency for the largest CMSP masses. One alternative is to use single-muon triggers. If only one CMSP is required to satisfy the muon trigger (and hence arrive within the trigger gate), events will be accepted where the second CMSP is moving too slowly to arrive within the trigger

[1] This would be absolutely necessary in a search for single CMSPs.

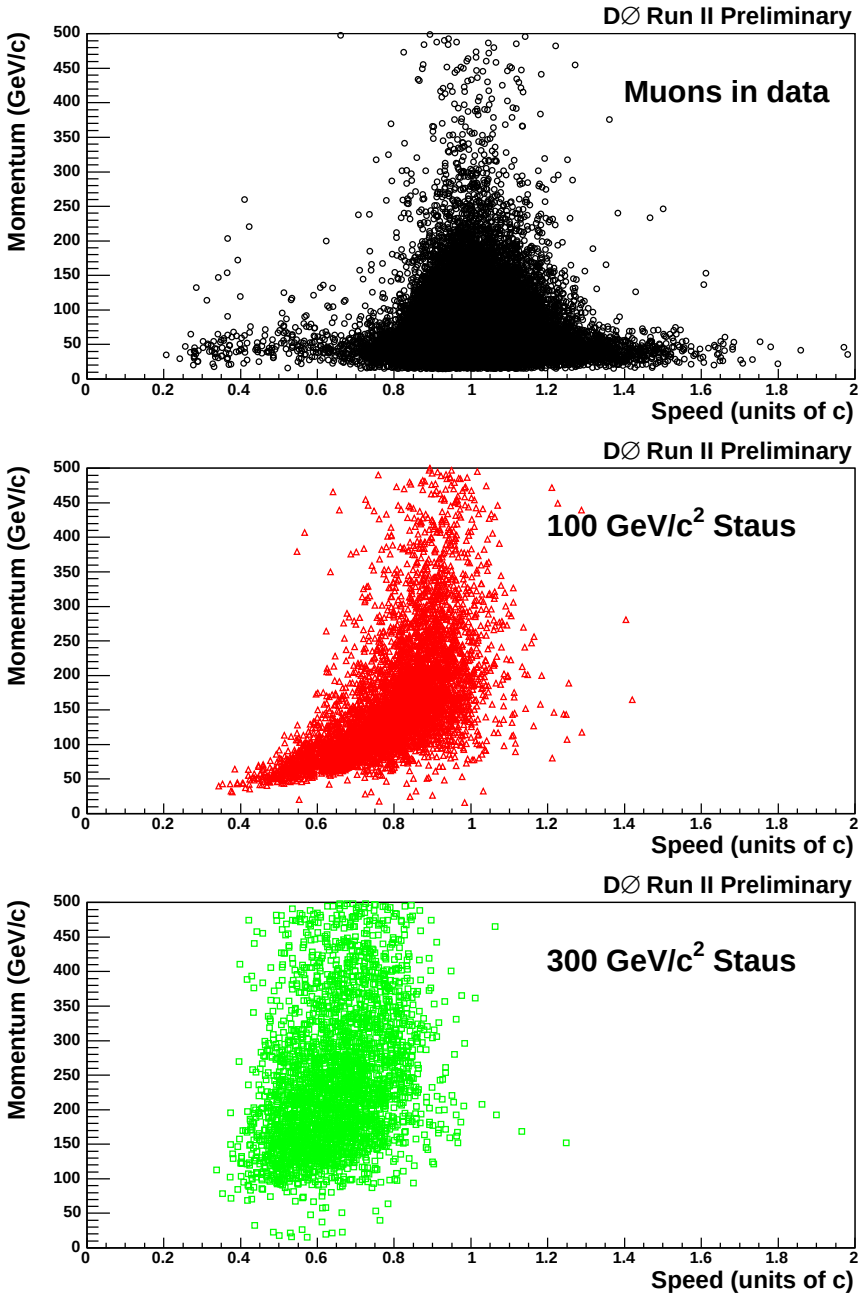


Figure 7.1: Momentum versus speed (in units of the speed of light) for muons from data (top, black circles), 100 GeV/$c^2$ staus (middle, red triangles), and 300 GeV/$c^2$ staus (bottom, green squares). Particles pass all preselection cuts. Histograms are normalized to approximately the same number of events.

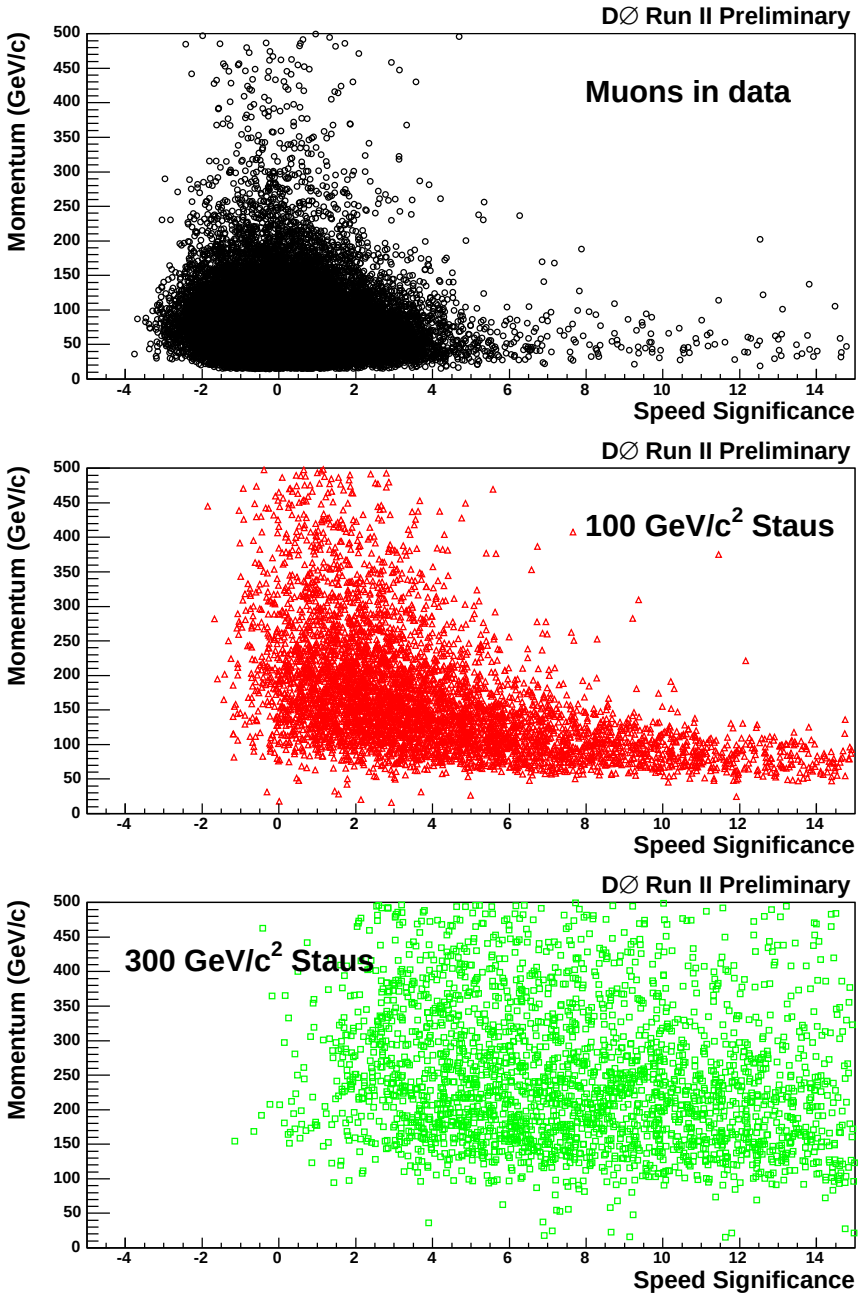


Figure 7.2: Momentum versus speed significance for muons from data (top, black circles), 100 GeV/$c^2$ staus (middle, red triangles), and 300 GeV/$c^2$ staus (bottom, green squares). Particles pass all preselection cuts. Histograms are normalized to approximately the same number of events.

gate. However, using a single-muon trigger does introduce other complications.[2] It may also be possible to create a trigger using tracks in the central tracking system.

It would also probably be useful to employ an advanced analysis method in a future version of the analysis. Since there are many variables that are measured in the detector that exhibit complicated correlations (such as scintillator times, speeds, and momenta), a neural network or similar tool will probably be able to achieve a good separation between signal and background.

In closing, this analysis has yielded cross section limits on the pair production of stable staus (which are the best limits to date from the Tevatron) and mass limits on stable charginos (which are the best in the world to date). However, there are many improvements that should significantly increase the sensitivity of future versions of the analysis, resulting in either much improved limits, or (hopefully) a discovery of CMSPs at DØ.

[2]Current (non-prescaled) single-muon triggers have a smaller coverage in psuedorapidity than the existing dimuon triggers. Furthermore, usable single-muon triggers have a transverse momentum requirement, but this would probably not be an issue for the CMSP channel. However, single-muon triggers also have a drift-tube wire hit requirements at Level 1. It is not clear if this would be efficient for CMSPs.

## REFERENCES


[1] H.P. Nilles, Phys. Rep. **110**, 1 (1984).

[2] M. Dine and A.E. Nelson, Phys. Rev. D **48**, 1277 (1993);
G.F. Giudice and R. Rattazzi, Phys. Rept. **322**, 419 (1999);
R. Culbertson, et.al., FERMILAB-PUB-00/251-T (unpublished).

[3] L. Randall and R. Sundrum, Nucl. Phys. B **557**, 79 (1999);
G.F. Giudice, M.A. Luty, M. Hurayama, and R. Rattazzi, JHEP **9812**, 027 (1998).

[4] M. Perl, et.al., Int. J. Mod. Phys. A **16**, 2137 (2001).

[5] J. Feng and T. Moroi, Phys. Rev. D **58**, 035001 (1998).

[6] J. Feng, S. Fu, and F. Takayama, Phys. Rev. D **70**, 063514 (2004);
**70**, 075019 (2004).

[7] C. Chen, M. Drees, and J. Gunion, Phys. Rev. D **55**, 330 (1997);
**60**, 039901 (1999).

[8] J. Gunion and S. Mrenna, Phys. Rev. D **62**, 015002 (2000).

[9] T. Ghergetta, G.F. Giudice, and J.D. Wells, Nucl. Phys. B **559**, 27 (1999).

[10] G. Anderson, H. Baer, C.H. Chen, and X. Tata, Phys. Rev D **61**, 095005 (2000).

[11] N. Arkani-Hamed, S. Dimopolous, G.F. Giudice, and A. Romanino, Nucl. Phys B **709**, 3 (2005).

[12] Covi, et.al., JHEP **0406**, 003 (2004).

[13] S. Eidelman, et.al., Phys. Lett B **592**, 1 (2004).

[14] P.F. Smith, et.al., Nucl. Phys B **206**, 333 (1982);
T.K. Hemmick, et.al., Phys. Rev. D **41**, 2074 (1990);
P. Verkerk, et. al., Phys. Rev. Lett **68**, 1116 (1992);

[15] D. Acosta, et.al., Phys. Rev. Lett. **90**, 131801 (2003).

[16] A. Heister, et. al., Eur. Phys. J. C **25**, 339 (2002);
J. Abdallah, et.al., Eur. Phys. J. C **27**, 153 (2003);
P. Achard, et.al., Phys. Lett. B **517**, 75 (2001);
G. Abbiendi, et. al., Phys. Lett. B **572**, 8 (2003).

[17] LEP2 SUSY Working Group,
http://lepsusy.web.cern.ch/lepsusy/www/stable_summer02/stable_208.html .

[18] A. Heister, et. al., Phys. Lett. B **533**, 223 (2002);
P. Abreu, et. al., Phys. Lett. B **444**, 491, 1998;
P. Abreu, et. al., Eur. Phys. J. C **11**, 1 (1999);
M. Acciarri, et. al., Phys. Lett. B **471**, 308 (1999);
G. Abbiendi, et. al., Phys. Lett. B **572**, 8 (2003).

[19] S. Abachi, et. al., Nucl. Instrum. Methods A **338**, 185 (1994).

[20] S. Abachi, et.al., Phys. Rev. Lett. **74**, 2632 (1995);
F. Abe, et.al., Phys. Rev. Lett. **74**, 2626 (1995).

[21] V. Abazov, et. al., in preparation for submission to Nucl. Instrum. Methods.

[22] V. Abazov, et. al., Fermilab-PUB-05-034-E, submitted to Nucl. Instrum. Methods.

[23] B. Baldin, et.al., "Technical Design of the Central Muon System", DØ note 3365 (unpublished).

[24] V. Abramov, et.al., "Technical Design Report for the DØ forward trigger scintillation counters", DØ note 3237 (unpublished);
G. Alexeev, et.al., "Technical Design Report for the DØ Forward Muon Tracking Detector based on Mini-drift Tubes", DØ note 3366 (unpublished).

[25] C. Bailey, S. Doulas, D. Wood, "Channel-by-channel t0 Calibration of the Central Muon Scintillators", DØ note 4291 (unpublished);
R. Harrington, "Channel-by-channel t0 Calibration of the Central Muon BC-layer Scintillation Counters", DØ note 4435 (unpublished).

[26] O. Peters, "Muon Segement Reconstruction - Linked List Algorithm", DØ note 3901 (unpublished).

[27] J. Butler, "Local Muon Momentum Resolution", DØnote 4002 (unpublished).

[28] C. Clement, et.al., "MuonID Certification for p14" DØ note 4350 (unpublished).

[29] S. Doulas, M. Eads, A. Ito, and D. Hedin, "Central Muon Scintillator Time of Flight Corrections", DØ note 4201 (unpublished).

[30] H.T. Diehl, et.al., "Central Muon Upgrade Scintillator Front-End Crate Addresses", DØnote 3642 (unpublished).

[31] M. Eads and D. Hedin, "A Search for Charged Massive Stable Particles at DØ", DØ note 4746 (unpublished).

[32] S.P. Martin, S. Moretti, J. Qian, G.W. Wilson, FERMILAB-CONF-01-371-T (unpublished);
B.C. Allanach, et.al., Eur. Phys J. C **25**, 113 (2002).

[33] T. Sjosstrand, et.al., Computer Physics Comun. **135**, 238 (2001).

[34] E. Nurse and P. Telford, "Measurement of the Cross section for Inclusive $Z$ Production in Di-muon Final States at $\sqrt{s} = 1.96$ TeV", DØ note 4573 (unpublished).

[35] The DØ Common Sample Group Skimming Page,
http://www-d0.fnal.gov/Run2Physics/cs/skimming/skimming.html .

[36] D. Denisov, A. Shchukin, "Study of the correlation between D0 Clock System timing drift and Forward Muon Scintillation Counters T0's", DØ note 4143 (unpublished);
D. Denisov, A. Shchukin, "Long-term stability of muon timing peak in the forward muon scintillation counters", DØ note 4458 (unpublished).

[37] T. Junk, Nucl. Instrum. Methods A **434**, 435 (1999).

[38] B.C. Allanach, hep-ph/0104145 (unpublished).

[39] W. Beenakker, M. Klasen, M. Kramer, T. Plehn, M. Spira and P. M. Zerwas, Phys. Rev. Lett. **83**, 3780 (1999)

[40] M. Klasen, G. Sajot, private communication.